

# Error Quantification and Mitigation for Numerical Compact Binary Waveforms

Thesis by  
Sarah Mary Habib

In Partial Fulfillment of the Requirements for the  
Degree of  
Doctor of Philosophy

The logo for the California Institute of Technology (Caltech), featuring the word "Caltech" in a bold, orange, sans-serif font.

CALIFORNIA INSTITUTE OF TECHNOLOGY  
Pasadena, California

2025  
Defended May 2nd, 2025

© 2025

Sarah Mary Habib  
ORCID: 0000-0002-4725-4978

All rights reserved

## ACKNOWLEDGEMENTS

Like any thesis, this one is a symbol of not only individual scientific efforts but also the strength of a community. Research is an inherently cooperative effort, and I have been extremely fortunate to work with some of the most passionate and supportive people in my field.

I would like to give a very deep thanks to my advisors within SXS, Mark Scheel and Saul Teukolsky, who have taught me what being a researcher means. From them I have learned that uncertainty and the unexpected are to be embraced as part of the spirit of science. Together they've imparted to me the crucial lesson to, as they would say, "add one nine at a time". Both Saul and Mark have also granted me an incredible amount of kindness, empathy, and patience. On one occasion, I expressed insecurities about my progress with Saul, and it was a great comfort to hear his response of having experienced similar feelings in the past. There were honestly many times when I doubted that I would be able to graduate, and ultimately I was able to because Saul and Mark believed in my abilities.

I would also like to give a special thanks to Elias Most, to whom I am especially indebted. Elias has been one of my biggest advocates in the department, and I could not have made it to this point without his mentorship and support. Elias has always been eager to share his feedback on my latest findings and spread an enthusiasm for science. Beyond that, he uplifted my work, pushed me out of my comfort zone, offered inexhaustible encouragement, and helped me find confidence in my abilities. Elias, I truly cannot put into words how much you have done for me. Thank you so much for everything.

The cohort of grad students, postdocs, and faculty within our collaboration was a source of endless support and camaraderie. Thanks to Keefe Mitman, Mike Pajkos, and Nils Vu, both for their interminable willingness to answer my questions and also for their presence as positive forces in our group. I would also like to thank Nils Deppe, who, on top of sharing technical and scientific knowledge, helped me mature both professionally and as a person transitioning within stages of life. An additional thanks to the countless other research collaborators who shared their expertise with me and make the numerical relativity community a privilege to be a part of.

Thanks to my defense committee members, Katerina Chatziioannou, Yanbei Chen, and Alan Weinstein. In particular I would also like to thank Alan not only for his

insightful comments on my thesis but also for the invaluable perspective he gave me shortly after I passed candidacy.

Thanks to JoAnn Boyd, who keeps all of TAPIR propped up on her shoulders.

Thanks to the many people at Caltech (and slightly beyond) without whom I would not have seen the other side of some extremely difficult times. Some supported me as research colleagues, all as friends who gave me countless valuable memories and brought much needed light into dark days. A very heartfelt thanks to Sasha Alabugin, Ivy Bennett-Ford, Yoonsoo Kim, Talya Klinger, Isaac Legred, Hannah Manetsch, Quinn Morgan, Kyle Nelli, Joe Ruan, Nicholas Rui, Kiran Shila, Rhiannon Udall, and others too numerous to list here, who made Caltech and Pasadena special for me.

Thanks to the music staff at Caltech, and especially Scott Babcock, Barb Caitlin, and Glenn Price, for being the backbone of a community I and many others have taken respite in. I would also like to thank Stephen Pfeiffer for granting me a means of artistic expression. Stephen, you're an incredible teacher, musician, and person.

Thanks to my friends Conan Huang and Marshall Shriner. Our friendship has trivialized a country-wide gap.

Finally, thanks to my siblings, Andy and Sophie, and my parents, Fakher and Zina, for their unconditional love and support.

## ABSTRACT

Gravitational wave analysis requires waveform models to compare with observed signals from compact binaries. These models are based on and validated by numerical relativity waveforms—waveforms output from codes developed to numerically evolve the Einstein field equations. The efficacy of numerical waveforms for analysis is limited by error from both numerical and astrophysical sources. This thesis makes two contributions to the quantification and mitigation of this error.

Chapter 2 describes a new algorithm for eccentricity reduction, the process of determining initial conditions for quasicircular binary orbits. This iterative procedure requires a measurement of eccentricity based on an early-inspiral trajectory. We find that the use of nonlinear fitting techniques such as variable projection leads to vastly improved consistency in eccentricity measurements.

Finally, Chapter 3 presents an in-depth quantification of error in numerical binary neutron star waveforms from three vastly different numerical relativity codes. We find that overall these codes produce consistent binary neutron star evolutions, but that further accuracy improvements will be required for analysis of next-generation gravitational wave detector signals.

## PUBLISHED CONTENT AND CONTRIBUTIONS

- [1] Sarah Habib, Mark Scheel, and Saul Teukolsky. “Eccentricity Reduction for Quasicircular Binary Evolutions”. In: *Physical Review D* (Oct. 2024). doi: [10.1103/PhysRevD.111.084059](https://doi.org/10.1103/PhysRevD.111.084059). arXiv: [2410.05531](https://arxiv.org/abs/2410.05531) [gr-qc].  
S.M.H. wrote the majority of the paper, implemented the described procedure, and performed the analysis. This paper has been adapted to Chapter 2.
  
- [2] Sarah Habib et al. “Error quantification and comparison of binary neutron star gravitational waveforms from numerical relativity codes”. In preparation.  
S.M.H. led writing of the paper and performed the analysis. This paper has been adapted to Chapter 3.

## CONTENTS

Acknowledgements . . . . .	iii
Abstract . . . . .	v
Published Content and Contributions . . . . .	vi
Contents . . . . .	vi
List of Figures . . . . .	ix
List of Tables . . . . .	xi
Chapter I: Introduction . . . . .	1
Chapter II: Eccentricity Reduction for Quasicircular Binary Black Holes . . . . .	14
2.1 Introduction . . . . .	15
2.2 Methods . . . . .	19
2.2.1 Current eccentricity reduction method . . . . .	19
2.2.2 Improved algorithm for eccentricity fitting . . . . .	22
2.2.2.1 Frequency domain pre-processing . . . . .	24
2.2.2.2 Initial guesses for fit parameters . . . . .	25
2.2.2.3 Variable projection . . . . .	28
2.2.2.4 New fitting formula for $\dot{\Omega}(t)$ . . . . .	29
2.3 Robustness test . . . . .	30
2.4 Conclusion . . . . .	32
2.5 Acknowledgments . . . . .	36
Chapter III: Error Quantification and Comparison of Binary Neutron Star Gravitational Waveforms from Numerical Relativity Codes . . . . .	45
3.1 Introduction . . . . .	46
3.2 Methods . . . . .	48
3.2.1 Evolution codes . . . . .	49
3.2.1.1 FIL . . . . .	49
3.2.1.2 SpEC . . . . .	50
3.2.1.3 SpECTRE . . . . .	52
3.2.2 Waveform extraction . . . . .	54
3.2.2.1 Nakano extrapolation . . . . .	56
3.2.2.2 Finite radius extrapolation . . . . .	57
3.2.2.3 Cauchy-Characteristic Evolution . . . . .	57
3.3 Results . . . . .	58
3.3.1 Waveform properties . . . . .	58
3.3.2 Error analysis . . . . .	60
3.3.2.1 Phase error convergence . . . . .	61
3.3.2.2 Waveform extraction error . . . . .	64
3.3.2.3 Phase error comparison . . . . .	66
3.3.3 Implications . . . . .	68
3.4 Conclusion . . . . .	71

3.5 Acknowledgments . . . . . 74

## LIST OF FIGURES

<i>Number</i>	<i>Page</i>
2.1 Eccentricity reduction flowchart . . . . .	18
2.2 Example binary black hole trajectories from the public SXS catalog .	23
2.3 Binary black hole trajectory data in time and frequency domains with and without high-frequency filtering . . . . .	26
2.4 Local minima in the residual function of Eq. (2.10) as related to the number of orbits used for fitting . . . . .	30
2.5 Nonlinear fits to a binary black hole trajectory using different initial guesses for the $\omega$ parameter . . . . .	31
2.6 Best fit values for Eq. (2.10) on an analytically generated trajectory with respect to fit window bounds . . . . .	33
2.7 Best fit values for Eq. (2.10) on numerical binary black hole trajectory SXS:BBH:0235 with respect to fit window bounds . . . . .	37
2.8 Histogram of standard deviation in measured eccentricity $e$ with respect to a changing fit window for binary black hole trajectories in the public SXS catalog . . . . .	38
3.1 Schematic spacetime diagram of simulation domains involved in CCE	59
3.2 Strain mode $l = 2, m = 2$ for binary neutron star waveforms from each assessed numerical relativity code using the highest resolutions available . . . . .	61
3.3 Strain mode $l = 2, m = 2$ for binary neutron star waveforms from each assessed numerical relativity code at all run resolutions . . . . .	62
3.4 Difference in phase between runs of varying resolutions within each code, both unscaled and with an additional scaling factor based on the expected convergence order . . . . .	65
3.5 Phase difference between SpEC binary neutron star waveforms using different waveform extraction methods (finite radius extraction ver- sus Cauchy-Characteristic evolution), compared to phase difference between finite radius extraction waveforms of different resolution . .	67
3.6 Phase difference between all analyzed numerical binary neutron star waveforms and the waveform Richardson-extrapolated from the two highest-resolution FIL waveforms . . . . .	69

- 3.7 Extrapolated mismatches between BNS waveforms and waveform  
Richardson extrapolation versus distinguishability threshold mismatches 72
- 3.8 Compute cost in core hours as a function of grid separation  $\Delta x$  . . . . 73

## LIST OF TABLES

<i>Number</i>		<i>Page</i>
3.1	Specifications for every numerical binary neutron star waveform produced . . . . .	55
3.2	Summary of projected grid resolutions and compute costs required to reach target mismatch thresholds . . . . .	71

*Chapter 1*

## INTRODUCTION

General relativity (GR), the modern theory of gravitation, describes gravity as a geometric property of spacetime, a four-dimensional manifold that is curved by the presence of energy. This concept is succinctly encapsulated by the Einstein Field Equations (EFEs), a set of nonlinear partial differential equations. GR has been wildly successful in predicting observed effects not explained by Newtonian gravity. In particular, GR predicts the existence of black holes, regions in spacetime formed by extremely compact mass and causally separated by an “event horizon”, and gravitational waves (GWs), waves that propagate in spacetime itself (analogous to electromagnetic radiation and its propagation in electromagnetic fields).

Extraordinary scientific effort has been put towards the detection and analysis of GWs (e.g. Refs. [15, 60, 10, 1, 4, 7, 77]). Although theoretically any accelerating and spherically asymmetric object emits gravitational radiation, the characteristic strain scale for GWs passing through Earth is so miniscule—ranging from about  $10^{-23}$  to  $10^{-18}$  even for loud signals—that only extremely energetic systems have so far proven feasible as subjects for observation. In fact, the only such system from which direct observations have been successfully made is compact binary coalescence (CBC), a pair of orbiting compact objects (e.g. black holes or neutron stars) that *inspiral* towards each other as a result of gravitational waves removing orbital energy (a process termed *radiation-reaction*) until they become close enough to *merge*, producing a *ringdown* signal in the aftermath as the newly formed object stabilizes. The relative masses of the merging objects (with equal-mass ratio binaries following vastly different evolutions from extreme-mass ratio binaries) and the presence of spins influences the resulting GW signal, so properties of the binary can be inferred from the signal morphology.

The first gravitational wave detection came indirectly from the discovery of the Hulse–Taylor pulsar [51], a neutron star–pulsar binary with an orbital decay rate in precise agreement with the rate of energy loss due to GW emission [85]. The first direct GW observation was achieved decades later by the Laser Interferometry Gravitational-wave Observatory (LIGO) Scientific Collaboration [6]. The detected signal, named GW150914, was emitted by a binary black hole (BBH) and was

the first of many similar compact binary detections to follow, including neutron star-black hole (NSBH) [9] and binary neutron star (BNS) events [5]. The primary mechanism of the LIGO GW detectors (specifically, the Virgo and Kamioka Gravitational Wave Detector (KAGRA) collaborations) is laser interferometry bolstered by highly sophisticated isolation from noise. Currently, GW interferometers are sensitive enough to detect compact binaries several orbits before merger [8], but are limited to stellar mass binary sources<sup>1</sup>.

Extensive matched-filter searches are used to identify likely GW signals in detection data [64, 65, 7]; signals are then further characterized through comparison to waveform templates and parameter estimation to constrain possible source properties (e.g. masses and spins) [8, 2]. However, it is not known ahead of time what parameters a signal will have, so each of these steps requires accurate waveform models.

A vast amount of research is dedicated to the purpose of developing gravitational waveform models. There is no single closed-form solution describing the full evolution of a CBC, so different modeling formalisms have been developed according to the span of gravitational regimes a CBC passes through. Post-Newtonian (PN) expansion [21], expressing the spacetime metric in terms of perturbations from Newtonian gravity in orders of  $v^2/c^2$ , provides an analytical description of waveforms in the weak-field regime with low  $v^2/c^2$ , e.g. from binaries with large orbital separation. PN modeling is surprisingly effective in the inspiral regime, even past the point where intuition suggests it should break down [17, 86]. Nonetheless, PN can be extended with effective-one-body resummation [26] and the self-force formalism [70], which are applied in practice to extreme mass ratio systems.

However, analytical modeling is not sufficient to describe the physics of compact binaries during the merger phase—for this purpose, the EFEs must be solved numerically, and the field of *numerical relativity* (NR) has developed to address this daunting task. On a high level, the goal of NR is to numerically solve the system of equations given by the EFEs, particularly for compact binary systems with GW emissions in the frequency band relevant for GW observatories<sup>2</sup>. In practice, this process requires successful interplay between several elements of mathematical and

<sup>1</sup>The space-based Laser Interferometer Space Antenna (LISA) is expected to be sensitive to super-massive binary black hole sources [12].

<sup>2</sup>Luckily, the EFEs in vacuum are mass scale-invariant, so the EFE description of BBHs is dependent on the mass ratio and not total mass.

computational machinery, since the EFEs specify a set of ten coupled nonlinear partial differential equations.

The first complete numerical simulation of a BBH coalescence was achieved in 2005 by Frans Pretorius [71], and since then many NR code suites have been written to consolidate the required technical tools for compact binary simulation, with or without matter, into a single simulation framework, such as the Spectral Einstein Code (SpEC) [81], the Einstein Toolkit (ETK) [58], the Bi-functional Adaptive Mesh (BAM) code [24, 25], IllinoisGRMHD [39], the Templated-Hydrodynamics Code (THC) [74], Maya [54], GR-Athena++ [33], GRChombo [31, 14], HAD [13], and SpECTRE [56]. These codes widely vary in setup, algorithmic schemes, and formalisms. For numerical integration, the EFEs must first be expressed in an appropriate form—that is, as an initial value problem that can be evolved forward in time. Multiple formalisms of the EFEs have been devised for implementation in NR codes, such as the generalized harmonic [72, 57], Baumgarte-Shapiro-Shibata-Nakamura [82, 19], and Z4c [22] formulations. Codes also take different approaches in how to deal with the physical singularities in black holes—using either “moving puncture” methods [18, 29] or by excising singularities from the evolution domain [48] as in SpEC. Furthermore, while many codes use finite differencing, SpEC uses spectral discretization for gravitational evolution [68], and SpECTRE implements a hybrid approach [56, 35, 34].

An end goal of NR is the production of large numerical waveform banks for use in observation experiments both directly in GW signal analysis and for reference in other modeling techniques such as effective-one-body [26], phenomenological [52, 55], or surrogate [83, 84] modeling. Such banks, or *catalogs*, need to span the wide parameter space of possible detection sources; for BBHs this space is at least 7-dimensional (for mass ratio and each 3-dimensional spin). As with NR codes, several BBH catalogs have been constructed by the NR community, including the NINJA [16, 11], MAYA [40], NCSA [50], GR-Athena++ [76], and BAM [47] catalogs. The Simulating eXtreme Spacetimes (SXS) collaboration has produced the largest catalog of BBH simulations to date using SpEC [23], totaling to  $\sim 3000$  publically available numerical waveforms, but still more are needed to thoroughly cover the BBH parameter space. The addition of matter to the evolution system makes BNSs and NSBHs even more expensive to simulate than BBHs, but there is no less need for a comprehensive BNS/NSBH waveform catalog. Attempts have been made at BNS catalogs, such as the CoRe database [38, 46]. However, because

of the added expense and difficulty of matter evolution, no comparably sized catalog to the SXS BBH database exists for BNS/NSBH waveforms.

A number of complications arise in numerical codes regardless of implementation choices, not least of which is the problem of how to correctly choose initial conditions, termed *initial data*. Initial data—the metric information from which evolution starts—needs to be constructed given a set of desired orbital parameters, e.g. masses, spins, initial positions, and initial velocities [88]. The choice of parameters reflects the astrophysical conditions of the simulated binary—in particular, orbital eccentricity carries implications for the binary formation channel. Binaries lose eccentricity during inspiral because of the radiation-reaction process [67, 66], so isolated binaries with long inspirals have low eccentricity by the time they merge and reach detection bands; conversely, dynamical binary formation channels can sometimes result in high eccentricity mergers [62, 80, 42, 89].

Because most GW detections are consistent with quasicircular orbits [79, 87, 45, 78, 63, 43, 53, 75], quasicircular binary simulation is of high interest to the NR community. However, eccentricity is difficult to control in a numerical binary simulation. Constructed initial data introduces spurious *junk radiation* in numerical binary evolution [32]. This junk radiation dissipates during the first few orbital cycles of evolution, affecting the extracted waveform as well as the orbital parameters recovered after evolution [59, 90, 49]. Additionally, eccentricity is not a well-defined parameter in GR, so measurement of eccentricity in a numerical orbit is imperfect due to the presence of nonzero radial velocity, and generally depends on definitions contrived from Newtonian mechanics and phenomenology in either the binary kinematics or the waveform (see e.g. Refs. [20, 27]). Most NR codes simulate quasicircular binaries by iteratively evolving initial data, measuring the apparent eccentricity in early evolution, and correcting the initial data for a new evolution in a process called *eccentricity reduction* [69, 28]. Accurate and robust eccentricity measurement in spite of the inherent difficulties is crucial for the tuning of numerical binary parameters.

Nonvacuum systems (e.g. BNSs and NSBHs as opposed to BBHs) pose an even greater challenge for simulation, as the EFEs are then coupled to the equations of hydrodynamics. Independent of additional gravitational coupling, numerically evolving hydrodynamical systems is already a rich field for which a body of algorithmic techniques have been developed. Computational hydrodynamics presents problems in discretizing the fluid equations so that physicality is preserved, and ac-

curately resolving phenomena within a large range of scales. In the context of NR, the challenge is then to incorporate hydrodynamical evolution while maintaining the integrity of the gravitational solution. Since the gravitational waveform is affected by the tidal deformation of merging neutron stars, BNS signals can constrain neutron star properties and the dense matter equation of state [30, 41, 3]. Tidal deformability signatures cannot be modeled analytically as they primarily occur near the merger regime where PN approximation breaks down and so are fitted for from numerical waveforms [37, 36], exacerbating the need for numerical binary neutron star waveforms in GW analysis. The current lack of an extensive BNS waveform catalog will need to be addressed for future GW analysis to be possible.

As in all computational simulation, one of the major challenges of NR is to effectively balance accuracy and efficiency. Current numerical waveforms need high enough accuracy to not systematically bias statistical waveform analysis, but currently do not meet this standard for next-generation detectors (e.g. Cosmic Explorer [77] and the Einstein Telescope [60]) and will require a 10× accuracy improvement to keep up [73, 44, 61]. The technical overhead involved even for a single BBH simulation (including ~20 orbits of inspiral with complete merger and ringdown evolution) can result in runtimes on the scale of weeks or months, so simply running simulations with higher resolutions is not a feasible long-term solution. Error is both numerical and astrophysical in nature, and the NR community cannot resolve the deficiencies of current codes without first quantifying these errors and gaining a thorough understanding of what sources are dominant.

This thesis addresses the need for error quantification and mitigation in binary waveform simulations in two contributions. First, described in Chapter 2, is a new algorithm for eccentricity reduction that shows improved consistency compared to previous methods. Chapter 3 presents a BNS waveform error analysis of state-of-the-art NR codes SpEC, FIL, and SpECTRE, and provides an assessment of how current accuracy standards fare in relation to the requirements set by future detector experiments.

## References

- [1] J. Aasi et al. “Advanced LIGO”. In: *Class. Quant. Grav.* 32 (2015), p. 074001. DOI: [10.1088/0264-9381/32/7/074001](https://doi.org/10.1088/0264-9381/32/7/074001). arXiv: [1411.4547](https://arxiv.org/abs/1411.4547) [gr-qc].

- [2] A. G. Abac et al. “Observation of Gravitational Waves from the Coalescence of a 2.5–4.5 M Compact Object and a Neutron Star”. In: *Astrophys. J. Lett.* 970.2 (2024), p. L34. doi: [10.3847/2041-8213/ad5beb](https://doi.org/10.3847/2041-8213/ad5beb). arXiv: [2404.04248](https://arxiv.org/abs/2404.04248) [[astro-ph.HE](#)].
- [3] B. P. Abbott et al. “GW170817: Measurements of neutron star radii and equation of state”. In: *Phys. Rev. Lett.* 121.16 (2018), p. 161101. doi: [10.1103/PhysRevLett.121.161101](https://doi.org/10.1103/PhysRevLett.121.161101). arXiv: [1805.11581](https://arxiv.org/abs/1805.11581) [[gr-qc](#)].
- [4] B. P. Abbott et al. “GWTC-1: A Gravitational-Wave Transient Catalog of Compact Binary Mergers Observed by LIGO and Virgo during the First and Second Observing Runs”. In: *Phys. Rev. X* 9.3 (2019), p. 031040. doi: [10.1103/PhysRevX.9.031040](https://doi.org/10.1103/PhysRevX.9.031040). arXiv: [1811.12907](https://arxiv.org/abs/1811.12907) [[astro-ph.HE](#)].
- [5] B. P. Abbott et al. “Multi-messenger Observations of a Binary Neutron Star Merger”. In: *Astrophys. J. Lett.* 848.2 (2017), p. L12. doi: [10.3847/2041-8213/aa91c9](https://doi.org/10.3847/2041-8213/aa91c9). arXiv: [1710.05833](https://arxiv.org/abs/1710.05833) [[astro-ph.HE](#)].
- [6] B. P. Abbott et al. “Observation of Gravitational Waves from a Binary Black Hole Merger”. In: *Phys. Rev. Lett.* 116.6 (2016), p. 061102. doi: [10.1103/PhysRevLett.116.061102](https://doi.org/10.1103/PhysRevLett.116.061102). arXiv: [1602.03837](https://arxiv.org/abs/1602.03837) [[gr-qc](#)].
- [7] Benjamin P Abbott et al. “A guide to LIGO–Virgo detector noise and extraction of transient gravitational-wave signals”. In: *Class. Quant. Grav.* 37.5 (2020), p. 055002. doi: [10.1088/1361-6382/ab685e](https://doi.org/10.1088/1361-6382/ab685e). arXiv: [1908.11170](https://arxiv.org/abs/1908.11170) [[gr-qc](#)].
- [8] R. Abbott et al. “GWTC-3: Compact Binary Coalescences Observed by LIGO and Virgo during the Second Part of the Third Observing Run”. In: *Phys. Rev. X* 13.4 (2023), p. 041039. doi: [10.1103/PhysRevX.13.041039](https://doi.org/10.1103/PhysRevX.13.041039). arXiv: [2111.03606](https://arxiv.org/abs/2111.03606) [[gr-qc](#)].
- [9] R. Abbott et al. “Observation of Gravitational Waves from Two Neutron Star–Black Hole Coalescences”. In: *Astrophys. J. Lett.* 915.1 (2021), p. L5. doi: [10.3847/2041-8213/ac082e](https://doi.org/10.3847/2041-8213/ac082e). arXiv: [2106.15163](https://arxiv.org/abs/2106.15163) [[astro-ph.HE](#)].
- [10] T. Accadia et al. “Virgo: a laser interferometer to detect gravitational waves”. In: *JINST* 7 (2012), P03012. doi: [10.1088/1748-0221/7/03/P03012](https://doi.org/10.1088/1748-0221/7/03/P03012).
- [11] P. Ajith et al. “The NINJA-2 catalog of hybrid post-Newtonian/numerical-relativity waveforms for non-precessing black-hole binaries”. In: *Class. Quant. Grav.* 29 (2012). Ed. by Mark Hannam et al. [Erratum: *Class. Quant. Grav.* 30, 199401 (2013)], p. 124001. doi: [10.1088/0264-9381/29/12/124001](https://doi.org/10.1088/0264-9381/29/12/124001). arXiv: [1201.5319](https://arxiv.org/abs/1201.5319) [[gr-qc](#)].
- [12] Pau Amaro-Seoane et al. “Laser Interferometer Space Antenna”. In: (Feb. 2017). arXiv: [1702.00786](https://arxiv.org/abs/1702.00786) [[astro-ph.IM](#)].
- [13] Matthew Anderson et al. “Relativistic MHD with Adaptive Mesh Refinement”. In: *Class. Quant. Grav.* 23 (2006), pp. 6503–6524. doi: [10.1088/0264-9381/23/22/025](https://doi.org/10.1088/0264-9381/23/22/025). arXiv: [gr-qc/0605102](https://arxiv.org/abs/gr-qc/0605102).

- [14] Tomas Andrade et al. “GRChombo: An adaptable numerical relativity code for fundamental physics”. In: *J. Open Source Softw.* 6.68 (2021), p. 3703. doi: [10.21105/joss.03703](https://doi.org/10.21105/joss.03703). arXiv: [2201.03458](https://arxiv.org/abs/2201.03458) [gr-qc].
- [15] Yoichi Aso et al. “Interferometer design of the KAGRA gravitational wave detector”. In: *Phys. Rev. D* 88.4 (2013), p. 043007. doi: [10.1103/PhysRevD.88.043007](https://doi.org/10.1103/PhysRevD.88.043007). arXiv: [1306.6747](https://arxiv.org/abs/1306.6747) [gr-qc].
- [16] Benjamin Aylott et al. “Status of NINJA: The Numerical INJection Analysis project”. In: *Class. Quant. Grav.* 26 (2009). Ed. by Patrick Sutton and Deirdre Shoemaker, p. 114008. doi: [10.1088/0264-9381/26/11/114008](https://doi.org/10.1088/0264-9381/26/11/114008). arXiv: [0905.4227](https://arxiv.org/abs/0905.4227) [gr-qc].
- [17] John G. Baker et al. “Consistency of post-Newtonian waveforms with numerical relativity”. In: *Phys. Rev. Lett.* 99 (2007), p. 181101. doi: [10.1103/PhysRevLett.99.181101](https://doi.org/10.1103/PhysRevLett.99.181101). arXiv: [gr-qc/0612024](https://arxiv.org/abs/gr-qc/0612024).
- [18] John G. Baker et al. “Gravitational wave extraction from an inspiraling configuration of merging black holes”. In: *Phys. Rev. Lett.* 96 (2006), p. 111102. doi: [10.1103/PhysRevLett.96.111102](https://doi.org/10.1103/PhysRevLett.96.111102). arXiv: [gr-qc/0511103](https://arxiv.org/abs/gr-qc/0511103).
- [19] Thomas W. Baumgarte and Stuart L. Shapiro. “On the numerical integration of Einstein’s field equations”. In: *Phys. Rev. D* 59 (1998), p. 024007. doi: [10.1103/PhysRevD.59.024007](https://doi.org/10.1103/PhysRevD.59.024007). arXiv: [gr-qc/9810065](https://arxiv.org/abs/gr-qc/9810065).
- [20] Luc Blanchet. “Gravitational radiation from post-Newtonian sources and inspiraling compact binaries”. In: *Living Rev. Rel.* 9 (2006), p. 4.
- [21] Luc Blanchet. “Post-Newtonian Theory for Gravitational Waves”. In: *Living Rev. Rel.* 17 (2014), p. 2. doi: [10.12942/lrr-2014-2](https://doi.org/10.12942/lrr-2014-2). arXiv: [1310.1528](https://arxiv.org/abs/1310.1528) [gr-qc].
- [22] C. Bona et al. “General covariant evolution formalism for numerical relativity”. In: *Phys. Rev. D* 67 (2003), p. 104005. doi: [10.1103/PhysRevD.67.104005](https://doi.org/10.1103/PhysRevD.67.104005). arXiv: [gr-qc/0302083](https://arxiv.org/abs/gr-qc/0302083).
- [23] Michael Boyle et al. “The SXS Collaboration catalog of binary black hole simulations”. In: *Class. Quant. Grav.* 36.19 (2019), p. 195006. doi: [10.1088/1361-6382/ab34e2](https://doi.org/10.1088/1361-6382/ab34e2). arXiv: [1904.04831](https://arxiv.org/abs/1904.04831) [gr-qc].
- [24] Bernd Bruegmann, Wolfgang Tichy, and Nina Jansen. “Numerical simulation of orbiting black holes”. In: *Phys. Rev. Lett.* 92 (2004), p. 211101. doi: [10.1103/PhysRevLett.92.211101](https://doi.org/10.1103/PhysRevLett.92.211101). arXiv: [gr-qc/0312112](https://arxiv.org/abs/gr-qc/0312112).
- [25] Bernd Bruegmann et al. “Calibration of Moving Puncture Simulations”. In: *Phys. Rev. D* 77 (2008), p. 024027. doi: [10.1103/PhysRevD.77.024027](https://doi.org/10.1103/PhysRevD.77.024027). arXiv: [gr-qc/0610128](https://arxiv.org/abs/gr-qc/0610128).
- [26] A. Buonanno and T. Damour. “Effective one-body approach to general relativistic two-body dynamics”. In: *Phys. Rev. D* 59 (1999), p. 084006. doi: [10.1103/PhysRevD.59.084006](https://doi.org/10.1103/PhysRevD.59.084006). arXiv: [gr-qc/9811091](https://arxiv.org/abs/gr-qc/9811091).

- [27] Alessandra Buonanno et al. “Reducing orbital eccentricity of precessing black-hole binaries”. In: *Phys. Rev. D* 83 (2011), p. 104034. DOI: [10.1103/PhysRevD.83.104034](https://doi.org/10.1103/PhysRevD.83.104034). arXiv: [1012.1549](https://arxiv.org/abs/1012.1549) [gr-qc].
- [28] Alessandra Buonanno et al. “Reducing orbital eccentricity of precessing black-hole binaries”. In: *Phys. Rev. D* 83 (10 2011), p. 104034. DOI: [10.1103/PhysRevD.83.104034](https://doi.org/10.1103/PhysRevD.83.104034). URL: <https://link.aps.org/doi/10.1103/PhysRevD.83.104034>.
- [29] Manuela Campanelli et al. “Accurate evolutions of orbiting black-hole binaries without excision”. In: *Phys. Rev. Lett.* 96 (2006), p. 111101. DOI: [10.1103/PhysRevLett.96.111101](https://doi.org/10.1103/PhysRevLett.96.111101). arXiv: [gr-qc/0511048](https://arxiv.org/abs/gr-qc/0511048).
- [30] Katerina Chatziioannou. “Uncertainty limits on neutron star radius measurements with gravitational waves”. In: *Phys. Rev. D* 105.8 (2022), p. 084021. DOI: [10.1103/PhysRevD.105.084021](https://doi.org/10.1103/PhysRevD.105.084021). arXiv: [2108.12368](https://arxiv.org/abs/2108.12368) [gr-qc].
- [31] Katy Clough et al. “GRChombo : Numerical Relativity with Adaptive Mesh Refinement”. In: *Class. Quant. Grav.* 32.24 (2015), p. 245011. DOI: [10.1088/0264-9381/32/24/245011](https://doi.org/10.1088/0264-9381/32/24/245011). arXiv: [1503.03436](https://arxiv.org/abs/1503.03436) [gr-qc].
- [32] Gregory B. Cook. “Initial data for numerical relativity”. In: *Living Rev. Rel.* 3 (2000), p. 5. DOI: [10.12942/lrr-2000-5](https://doi.org/10.12942/lrr-2000-5). arXiv: [gr-qc/0007085](https://arxiv.org/abs/gr-qc/0007085).
- [33] Boris Daszuta et al. “GR-Athena++: Puncture Evolutions on Vertex-centered Oct-tree Adaptive Mesh Refinement”. In: *Astrophys. J. Supp.* 257.2 (2021), p. 25. DOI: [10.3847/1538-4365/ac157b](https://doi.org/10.3847/1538-4365/ac157b). arXiv: [2101.08289](https://arxiv.org/abs/2101.08289) [gr-qc].
- [34] Nils Deppe et al. “Binary neutron star mergers using a discontinuous Galerkin-finite difference hybrid method”. In: *Class. Quant. Grav.* 41.24 (2024), p. 245002. DOI: [10.1088/1361-6382/ad88cf](https://doi.org/10.1088/1361-6382/ad88cf). arXiv: [2406.19038](https://arxiv.org/abs/2406.19038) [gr-qc].
- [35] Nils Deppe et al. “A high-order shock capturing discontinuous Galerkin-finite difference hybrid method for GRMHD”. In: *Class. Quant. Grav.* 39.19 (2022), p. 195001. DOI: [10.1088/1361-6382/ac8864](https://doi.org/10.1088/1361-6382/ac8864). arXiv: [2109.11645](https://arxiv.org/abs/2109.11645) [gr-qc].
- [36] Tim Dietrich et al. “Matter imprints in waveform models for neutron star binaries: Tidal and self-spin effects”. In: *Phys. Rev. D* 99.2 (2019), p. 024029. DOI: [10.1103/PhysRevD.99.024029](https://doi.org/10.1103/PhysRevD.99.024029). arXiv: [1804.02235](https://arxiv.org/abs/1804.02235) [gr-qc].
- [37] Tim Dietrich, Sebastiano Bernuzzi, and Wolfgang Tichy. “Closed-form tidal approximants for binary neutron star gravitational waveforms constructed from high-resolution numerical relativity simulations”. In: *Phys. Rev. D* 96.12 (2017), p. 121501. DOI: [10.1103/PhysRevD.96.121501](https://doi.org/10.1103/PhysRevD.96.121501). arXiv: [1706.02969](https://arxiv.org/abs/1706.02969) [gr-qc].
- [38] Tim Dietrich et al. “CoRe database of binary neutron star merger waveforms”. In: *Class. Quant. Grav.* 35.24 (2018), 24LT01. DOI: [10.1088/1361-6382/aaebc0](https://doi.org/10.1088/1361-6382/aaebc0). arXiv: [1806.01625](https://arxiv.org/abs/1806.01625) [gr-qc].

- [39] Zachariah B. Etienne et al. “IllinoisGRMHD: An Open-Source, User-Friendly GRMHD Code for Dynamical Spacetimes”. In: *Class. Quant. Grav.* 32 (2015), p. 175009. doi: [10.1088/0264-9381/32/17/175009](https://doi.org/10.1088/0264-9381/32/17/175009). arXiv: [1501.07276](https://arxiv.org/abs/1501.07276) [[astro-ph.HE](#)].
- [40] Deborah Ferguson et al. “Second MAYA Catalog of Binary Black Hole Numerical Relativity Waveforms”. In: (Sept. 2023). arXiv: [2309.00262](https://arxiv.org/abs/2309.00262) [[gr-qc](#)].
- [41] Daniel Finstad, Laurel V. White, and Duncan A. Brown. “Prospects for a Precise Equation of State Measurement from Advanced LIGO and Cosmic Explorer”. In: *Astrophys. J.* 955.1 (2023), p. 45. doi: [10.3847/1538-4357/acf12f](https://doi.org/10.3847/1538-4357/acf12f). arXiv: [2211.01396](https://arxiv.org/abs/2211.01396) [[astro-ph.HE](#)].
- [42] Giacomo Fragione and Bence Kocsis. “Black hole mergers from an evolving population of globular clusters”. In: *Phys. Rev. Lett.* 121.16 (2018), p. 161103. doi: [10.1103/PhysRevLett.121.161103](https://doi.org/10.1103/PhysRevLett.121.161103). arXiv: [1806.02351](https://arxiv.org/abs/1806.02351) [[astro-ph.GA](#)].
- [43] Rossella Gamba et al. “GW190521 as a dynamical capture of two nonspinning black holes”. In: *Nature Astron.* 7.1 (2023), pp. 11–17. doi: [10.1038/s41550-022-01813-w](https://doi.org/10.1038/s41550-022-01813-w). arXiv: [2106.05575](https://arxiv.org/abs/2106.05575) [[gr-qc](#)].
- [44] Rossella Gamba et al. “Waveform systematics in the gravitational-wave inference of tidal parameters and equation of state from binary neutron star signals”. In: *Phys. Rev. D* 103.12 (2021), p. 124015. doi: [10.1103/PhysRevD.103.124015](https://doi.org/10.1103/PhysRevD.103.124015). arXiv: [2009.08467](https://arxiv.org/abs/2009.08467) [[gr-qc](#)].
- [45] V. Gayathri et al. “Eccentricity estimate for black hole mergers with numerical relativity simulations”. In: *Nature Astron.* 6.3 (2022), pp. 344–349. doi: [10.1038/s41550-021-01568-w](https://doi.org/10.1038/s41550-021-01568-w). arXiv: [2009.05461](https://arxiv.org/abs/2009.05461) [[astro-ph.HE](#)].
- [46] Alejandra Gonzalez et al. “Second release of the CoRe database of binary neutron star merger waveforms”. In: *Class. Quant. Grav.* 40.8 (2023), p. 085011. doi: [10.1088/1361-6382/acc231](https://doi.org/10.1088/1361-6382/acc231). arXiv: [2210.16366](https://arxiv.org/abs/2210.16366) [[gr-qc](#)].
- [47] Eleanor Hamilton et al. “Catalog of precessing black-hole-binary numerical-relativity simulations”. In: *Phys. Rev. D* 109.4 (2024), p. 044032. doi: [10.1103/PhysRevD.109.044032](https://doi.org/10.1103/PhysRevD.109.044032). arXiv: [2303.05419](https://arxiv.org/abs/2303.05419) [[gr-qc](#)].
- [48] Daniel A. Hemberger et al. “Dynamical Excision Boundaries in Spectral Evolutions of Binary Black Hole Spacetimes”. In: *Class. Quant. Grav.* 30 (2013), p. 115001. doi: [10.1088/0264-9381/30/11/115001](https://doi.org/10.1088/0264-9381/30/11/115001). arXiv: [1211.6079](https://arxiv.org/abs/1211.6079) [[gr-qc](#)].
- [49] Kenny Higginbotham et al. “Coping with spurious radiation in binary black hole simulations”. In: *Phys. Rev. D* 100.8 (2019), p. 081501. doi: [10.1103/PhysRevD.100.081501](https://doi.org/10.1103/PhysRevD.100.081501). arXiv: [1907.00027](https://arxiv.org/abs/1907.00027) [[gr-qc](#)].

- [50] E. A. Huerta et al. “Physics of eccentric binary black hole mergers: A numerical relativity perspective”. In: *Phys. Rev. D* 100.6 (2019), p. 064003. doi: [10.1103/PhysRevD.100.064003](https://doi.org/10.1103/PhysRevD.100.064003). arXiv: [1901.07038](https://arxiv.org/abs/1901.07038) [gr-qc].
- [51] R. A. Hulse and J. H. Taylor. “Discovery of a pulsar in a binary system”. In: *Astrophys. J. Lett.* 195 (1975), pp. L51–L53. doi: [10.1086/181708](https://doi.org/10.1086/181708).
- [52] Sascha Husa et al. “Frequency-domain gravitational waves from nonprecessing black-hole binaries. I. New numerical waveforms and anatomy of the signal”. In: *Phys. Rev. D* 93.4 (2016), p. 044006. doi: [10.1103/PhysRevD.93.044006](https://doi.org/10.1103/PhysRevD.93.044006). arXiv: [1508.07250](https://arxiv.org/abs/1508.07250) [gr-qc].
- [53] H. L. Iglesias et al. *Eccentricity estimation for five binary black hole mergers with higher-order gravitational wave modes*. Aug. 2022. arXiv: [2208.01766](https://arxiv.org/abs/2208.01766) [gr-qc].
- [54] Karan Jani et al. “Georgia Tech Catalog of Gravitational Waveforms”. In: *Class. Quant. Grav.* 33.20 (2016), p. 204001. doi: [10.1088/0264-9381/33/20/204001](https://doi.org/10.1088/0264-9381/33/20/204001). arXiv: [1605.03204](https://arxiv.org/abs/1605.03204) [gr-qc].
- [55] Sebastian Khan et al. “Frequency-domain gravitational waves from nonprecessing black-hole binaries. II. A phenomenological model for the advanced detector era”. In: *Phys. Rev. D* 93.4 (2016), p. 044007. doi: [10.1103/PhysRevD.93.044007](https://doi.org/10.1103/PhysRevD.93.044007). arXiv: [1508.07253](https://arxiv.org/abs/1508.07253) [gr-qc].
- [56] Lawrence E. Kidder et al. “SpECTRE: A task-based discontinuous Galerkin code for relativistic astrophysics”. In: *J. Comput. Phys.* 335 (2017), pp. 84–114. doi: [10.1016/j.jcp.2016.12.059](https://doi.org/10.1016/j.jcp.2016.12.059). arXiv: [1609.00098](https://arxiv.org/abs/1609.00098) [astro-ph.HE].
- [57] Lee Lindblom et al. “A New generalized harmonic evolution system”. In: *Class. Quant. Grav.* 23 (2006), S447–S462. doi: [10.1088/0264-9381/23/16/S09](https://doi.org/10.1088/0264-9381/23/16/S09). arXiv: [gr-qc/0512093](https://arxiv.org/abs/gr-qc/0512093).
- [58] Frank Löffler et al. “The Einstein Toolkit: A Community Computational Infrastructure for Relativistic Astrophysics”. In: *Class. Quant. Grav.* 29 (2012), p. 115001. doi: [10.1088/0264-9381/29/11/115001](https://doi.org/10.1088/0264-9381/29/11/115001). arXiv: [1111.3344](https://arxiv.org/abs/1111.3344) [gr-qc].
- [59] Geoffrey Lovelace. “Reducing spurious gravitational radiation in binary-black-hole simulations by using conformally curved initial data”. In: *Class. Quant. Grav.* 26 (2009), p. 114002. doi: [10.1088/0264-9381/26/11/114002](https://doi.org/10.1088/0264-9381/26/11/114002). arXiv: [0812.3132](https://arxiv.org/abs/0812.3132) [gr-qc].
- [60] Michele Maggiore et al. “Science Case for the Einstein Telescope”. In: *JCAP* 03 (2020), p. 050. doi: [10.1088/1475-7516/2020/03/050](https://doi.org/10.1088/1475-7516/2020/03/050). arXiv: [1912.02622](https://arxiv.org/abs/1912.02622) [astro-ph.CO].
- [61] Keefe Mitman et al. “Length dependence of waveform mismatch: a caveat on waveform accuracy”. In: (Feb. 2025). arXiv: [2502.14025](https://arxiv.org/abs/2502.14025) [gr-qc].

- [62] Ryan M. O’Leary et al. “Binary mergers and growth of black holes in dense star clusters”. In: *Astrophys. J.* 637 (2006), pp. 937–951. DOI: [10.1086/498446](https://doi.org/10.1086/498446). arXiv: [astro-ph/0508224](https://arxiv.org/abs/astro-ph/0508224).
- [63] Eamonn O’Shea and Prayush Kumar. “Correlations in gravitational-wave reconstructions from eccentric binaries: A case study with GW151226 and GW170608”. In: *Phys. Rev. D* 108.10 (2023), p. 104018. DOI: [10.1103/PhysRevD.108.104018](https://doi.org/10.1103/PhysRevD.108.104018). arXiv: [2107.07981](https://arxiv.org/abs/2107.07981) [[astro-ph](https://arxiv.org/abs/astro-ph).HE].
- [64] Benjamin J. Owen. “Search templates for gravitational waves from inspiraling binaries: Choice of template spacing”. In: *Phys. Rev. D* 53 (1996), pp. 6749–6761. DOI: [10.1103/PhysRevD.53.6749](https://doi.org/10.1103/PhysRevD.53.6749). arXiv: [gr-qc/9511032](https://arxiv.org/abs/gr-qc/9511032).
- [65] Benjamin J. Owen and B. S. Sathyaprakash. “Matched filtering of gravitational waves from inspiraling compact binaries: Computational cost and template placement”. In: *Phys. Rev. D* 60 (1999), p. 022002. DOI: [10.1103/PhysRevD.60.022002](https://doi.org/10.1103/PhysRevD.60.022002). arXiv: [gr-qc/9808076](https://arxiv.org/abs/gr-qc/9808076).
- [66] P. C. Peters. “Gravitational Radiation and the Motion of Two Point Masses”. In: *Phys. Rev.* 136 (4B 1964), B1224–B1232. DOI: [10.1103/PhysRev.136.B1224](https://doi.org/10.1103/PhysRev.136.B1224). URL: <https://link.aps.org/doi/10.1103/PhysRev.136.B1224>.
- [67] P. C. Peters and J. Mathews. “Gravitational Radiation from Point Masses in a Keplerian Orbit”. In: *Phys. Rev.* 131 (1 1963), pp. 435–440. DOI: [10.1103/PhysRev.131.435](https://doi.org/10.1103/PhysRev.131.435). URL: <https://link.aps.org/doi/10.1103/PhysRev.131.435>.
- [68] Harald P. Pfeiffer et al. “A multidomain spectral method for solving elliptic equations”. In: *Computer Physics Communications* 152.3 (May 2003), pp. 253–273. DOI: [10.1016/S0010-4655\(02\)00847-0](https://doi.org/10.1016/S0010-4655(02)00847-0). arXiv: [gr-qc/0202096](https://arxiv.org/abs/gr-qc/0202096) [[gr-qc](https://arxiv.org/abs/gr-qc)].
- [69] Harald P. Pfeiffer et al. “Reducing orbital eccentricity in binary black hole simulations”. In: *Class. Quant. Grav.* 24 (2007). Ed. by Manuela Campanelli and Luciano Rezzolla, S59–S82. DOI: [10.1088/0264-9381/24/12/S06](https://doi.org/10.1088/0264-9381/24/12/S06). arXiv: [gr-qc/0702106](https://arxiv.org/abs/gr-qc/0702106).
- [70] Eric Poisson, Adam Pound, and Ian Vega. “The Motion of point particles in curved spacetime”. In: *Living Rev. Rel.* 14 (2011), p. 7. DOI: [10.12942/lrr-2011-7](https://doi.org/10.12942/lrr-2011-7). arXiv: [1102.0529](https://arxiv.org/abs/1102.0529) [[gr-qc](https://arxiv.org/abs/gr-qc)].
- [71] Frans Pretorius. “Evolution of binary black hole spacetimes”. In: *Phys. Rev. Lett.* 95 (2005), p. 121101. DOI: [10.1103/PhysRevLett.95.121101](https://doi.org/10.1103/PhysRevLett.95.121101). arXiv: [gr-qc/0507014](https://arxiv.org/abs/gr-qc/0507014).
- [72] Frans Pretorius. “Numerical relativity using a generalized harmonic decomposition”. In: *Class. Quant. Grav.* 22 (2005), pp. 425–452. DOI: [10.1088/0264-9381/22/2/014](https://doi.org/10.1088/0264-9381/22/2/014). arXiv: [gr-qc/0407110](https://arxiv.org/abs/gr-qc/0407110).

- [73] Michael Pürrer and Carl-Johan Haster. “Gravitational waveform accuracy requirements for future ground-based detectors”. In: *Phys. Rev. Res.* 2.2 (2020), p. 023151. DOI: [10.1103/PhysRevResearch.2.023151](https://doi.org/10.1103/PhysRevResearch.2.023151). arXiv: [1912.10055](https://arxiv.org/abs/1912.10055) [gr-qc].
- [74] David Radice and Luciano Rezzolla. “THC: a new high-order finite-difference high-resolution shock-capturing code for special-relativistic hydrodynamics”. In: *Astron. Astrophys.* 547 (2012), A26. DOI: [10.1051/0004-6361/201219735](https://doi.org/10.1051/0004-6361/201219735). arXiv: [1206.6502](https://arxiv.org/abs/1206.6502) [astro-ph.IM].
- [75] Antoni Ramos-Buades, Alessandra Buonanno, and Jonathan Gair. “Bayesian inference of binary black holes with inspiral-merger-ringdown waveforms using two eccentric parameters”. In: *Phys. Rev. D* 108.12 (2023), p. 124063. DOI: [10.1103/PhysRevD.108.124063](https://doi.org/10.1103/PhysRevD.108.124063). arXiv: [2309.15528](https://arxiv.org/abs/2309.15528) [gr-qc].
- [76] Alireza Rashti et al. “Binary Black Hole Waveforms from High-Resolution GR-Athena++ Simulations”. In: (Nov. 2024). arXiv: [2411.11989](https://arxiv.org/abs/2411.11989) [gr-qc].
- [77] David Reitze et al. “Cosmic Explorer: The U.S. Contribution to Gravitational-Wave Astronomy beyond LIGO”. In: *Bull. Am. Astron. Soc.* 51.7 (2019), p. 035. arXiv: [1907.04833](https://arxiv.org/abs/1907.04833) [astro-ph.IM].
- [78] Isobel M. Romero-Shaw, Paul D. Lasky, and Eric Thrane. “Signs of Eccentricity in Two Gravitational-wave Signals May Indicate a Subpopulation of Dynamically Assembled Binary Black Holes”. In: *Astrophys. J. Lett.* 921.2 (2021), p. L31. DOI: [10.3847/2041-8213/ac3138](https://doi.org/10.3847/2041-8213/ac3138). arXiv: [2108.01284](https://arxiv.org/abs/2108.01284) [astro-ph.HE].
- [79] Isobel M. Romero-Shaw et al. “GW190521: orbital eccentricity and signatures of dynamical formation in a binary black hole merger signal”. In: *Astrophys. J. Lett.* 903.1 (2020), p. L5. DOI: [10.3847/2041-8213/abbe26](https://doi.org/10.3847/2041-8213/abbe26). arXiv: [2009.04771](https://arxiv.org/abs/2009.04771) [astro-ph.HE].
- [80] Johan Samsing. “Eccentric Black Hole Mergers Forming in Globular Clusters”. In: *Phys. Rev. D* 97.10 (2018), p. 103014. DOI: [10.1103/PhysRevD.97.103014](https://doi.org/10.1103/PhysRevD.97.103014). arXiv: [1711.07452](https://arxiv.org/abs/1711.07452) [astro-ph.HE].
- [81] Mark A. Scheel et al. “High-accuracy waveforms for binary black hole inspiral, merger, and ringdown”. In: *Phys. Rev. D* 79 (2009), p. 024003. DOI: [10.1103/PhysRevD.79.024003](https://doi.org/10.1103/PhysRevD.79.024003). arXiv: [0810.1767](https://arxiv.org/abs/0810.1767) [gr-qc].
- [82] Masaru Shibata and Takashi Nakamura. “Evolution of three-dimensional gravitational waves: Harmonic slicing case”. In: *Phys. Rev. D* 52 (1995), pp. 5428–5444. DOI: [10.1103/PhysRevD.52.5428](https://doi.org/10.1103/PhysRevD.52.5428).
- [83] Vijay Varma et al. “Surrogate model of hybridized numerical relativity binary black hole waveforms”. In: *Phys. Rev. D* 99.6 (2019), p. 064045. DOI: [10.1103/PhysRevD.99.064045](https://doi.org/10.1103/PhysRevD.99.064045). arXiv: [1812.07865](https://arxiv.org/abs/1812.07865) [gr-qc].

- [84] Vijay Varma et al. “Surrogate models for precessing binary black hole simulations with unequal masses”. In: *Phys. Rev. Research*. 1 (2019), p. 033015. doi: [10.1103/PhysRevResearch.1.033015](https://doi.org/10.1103/PhysRevResearch.1.033015). arXiv: [1905.09300](https://arxiv.org/abs/1905.09300) [gr-qc].
- [85] J. M. Weisberg, J. H. Taylor, and L. A. Fowler. “GRAVITATIONAL WAVES FROM AN ORBITING PULSAR”. In: *Sci. Am.* 245 (1981), pp. 66–74. doi: [10.1038/scientificamerican1081-74](https://doi.org/10.1038/scientificamerican1081-74).
- [86] Clifford M. Will. “On the unreasonable effectiveness of the post-Newtonian approximation in gravitational physics”. In: *Proc. Nat. Acad. Sci.* 108 (2011), p. 5938. doi: [10.1073/pnas.1103127108](https://doi.org/10.1073/pnas.1103127108). arXiv: [1102.5192](https://arxiv.org/abs/1102.5192) [gr-qc].
- [87] Shichao Wu, Zhoujian Cao, and Zong-Hong Zhu. “Measuring the eccentricity of binary black holes in GWTC-1 by using the inspiral-only waveform”. In: *Mon. Not. Roy. Astron. Soc.* 495.1 (2020), pp. 466–478. doi: [10.1093/mnras/staa1176](https://doi.org/10.1093/mnras/staa1176). arXiv: [2002.05528](https://arxiv.org/abs/2002.05528) [astro-ph.IM].
- [88] James W. York Jr. “Conformal ‘thin sandwich’ data for the initial-value problem”. In: *Phys. Rev. Lett.* 82 (1999), pp. 1350–1353. doi: [10.1103/PhysRevLett.82.1350](https://doi.org/10.1103/PhysRevLett.82.1350). arXiv: [gr-qc/9810051](https://arxiv.org/abs/gr-qc/9810051).
- [89] Michael Zevin et al. “Implications of Eccentric Observations on Binary Black Hole Formation Channels”. In: *Astrophys. J. Lett.* 921.2 (2021), p. L43. doi: [10.3847/2041-8213/ac32dc](https://doi.org/10.3847/2041-8213/ac32dc). arXiv: [2106.09042](https://arxiv.org/abs/2106.09042) [astro-ph.HE].
- [90] Fan Zhang and Béla Szilágyi. “A joint approach for reducing eccentricity and spurious gravitational radiation in binary black hole initial data construction”. In: *Phys. Rev. D* 88 (2013), p. 084033. doi: [10.1103/PhysRevD.88.084033](https://doi.org/10.1103/PhysRevD.88.084033). arXiv: [1309.1141](https://arxiv.org/abs/1309.1141) [gr-qc].

*Chapter 2*ECCENTRICITY REDUCTION FOR QUASICIRCULAR  
BINARY BLACK HOLES

- [1] Sarah Habib, Mark Scheel, and Saul Teukolsky. “Eccentricity Reduction for Quasicircular Binary Evolutions”. In: *Physical Review D* (Oct. 2024). DOI: [10.1103/PhysRevD.111.084059](https://doi.org/10.1103/PhysRevD.111.084059). arXiv: [2410.05531](https://arxiv.org/abs/2410.05531) [gr-qc].

Simulation of quasicircular compact binaries is a major goal in numerical relativity, as they are expected to constitute most gravitational wave observations. However, given that orbital eccentricity is not well-defined in general relativity, providing initial data for such binaries is a challenge for numerical simulations. Most numerical relativity codes obtain initial conditions for low-eccentricity binary simulations by iterating over a sequence of short simulations—measuring eccentricity mid-evolution and correcting the initial data parameters accordingly. Eccentricity measurement depends on a numerically challenging nonlinear fit to an estimator model, and the resulting eccentricity estimate is extremely sensitive to small changes in how the fit is performed. We have developed an improved algorithm that produces more consistent measurements of eccentricity relative to the time window chosen for fitting. The primary innovations are the use of the nonlinear optimization algorithm, variable projection, in place of more conventional routines, an initial fit parameter guess taken from the trajectory frequency spectrum, and additional frequency processing of the trajectory data prior to fitting.

## 2.1 Introduction

Quasicircular compact binaries are expected to make up the majority of binaries detected by gravitational wave observatories. This is because gravitational radiation causes binaries to circularize during inspiral, resulting in low eccentricity at merger [35, 34]. Indeed, most studies of gravitational-wave (GW) detection events show that the waveforms are consistent with quasicircular orbits [44, 55, 14, 43, 32, 13, 20, 40]. However, there is evidence that some events may have nonzero eccentricity [17]. This suggests that some binaries might have formed relatively recently by dynamical processes, for example, in dense environments such as globular clusters [31, 45, 12, 59].

Our best understanding of GW events from binary mergers relies on numerical relativity (NR). This can be either from direct simulations, or from surrogate models [51, 3, 56, 22, 57, 21] or analytical waveform models [10, 28, 26] calibrated to NR. These NR simulations are formulated in terms of initial-value problems that involve two steps. The first step is the construction of *initial data* [9] that satisfy the Einstein constraint equations on some surface of constant coordinate time. In this step properties such as the masses and spins of the objects and their initial positions and velocities are freely specifiable. The second step is the *evolution* of the initial data through time, which yields the spacetime metric as a function of time, including

the emitted gravitational radiation.

To understand quasicircular binary inspirals, it is therefore important to construct NR simulations that have nearly zero orbital eccentricity. In Newtonian physics this would be straightforward: Kepler’s laws allow specifying initial positions and velocities of the objects that correspond to zero eccentricity. However, this is not true in general relativity (GR). First of all, in GR there are no truly circular orbits because of radiation reaction. Thus, the goal is to achieve a quasicircular orbit in which the binary orbit decays at a monotonic (as opposed to oscillatory) rate, in the absence of spin. For spinning objects, the goal is still to reduce oscillations in the orbit, but this is more complicated because spin-spin interactions produce oscillations that must be distinguished from those caused by eccentricity [7]. In the post-Newtonian (PN) approximation it is possible to compute expressions for particle positions and velocities (or equivalently, initial orbital separation, orbital frequency, and radial velocity) that give quasicircular orbits [2], and indeed by using high enough order PN these expressions can be used [19, 8] to produce NR simulations with eccentricity of order  $10^{-3}$ . However, for accurate waveforms we want to achieve eccentricities smaller than this.

One potential drawback of using PN expressions directly is that the gauge (coordinate) choices used in PN typically differ from those used in NR [36, 50], so that PN and NR orbits can disagree to an extent that is difficult to predict. Yet another problem stems from initial transients that appear in NR simulations. These transients occur because NR initial data, even in the infinite-resolution limit, does not contain the same gravitational radiation as would a snapshot of a binary that has been inspiralling since the infinite past. Instead, at the beginning of the evolution the solution quickly relaxes to quasiequilibrium, slightly changing the initial parameters and the orbit and emitting high-frequency gravitational waves in the process; these waves are known as “junk radiation”. There have been attempts to reduce the amount of junk radiation in NR simulations [1, 58, 23, 24, 42, 49, 27, 50], but typically one simply discards the first few orbits of the simulation until the junk radiation has decayed away [6].

To handle the above difficulties, we have adopted an iterative method for producing quasicircular NR initial data [38, 7, 39, 41]: an initial guess is chosen for NR initial data parameters, the binary is evolved for a few orbits using NR and the eccentricity is measured from that evolution, and then the initial guess is updated so as to give smaller eccentricity for the next iteration. See Fig. 2.1 for an illustration of the

process.

In this chapter we discuss improvements to the iterative eccentricity-reduction method of Ref. [7] and its implementation in the NR code SpEC [48]. Although we limit the discussion and particular examples to black-hole binaries and to SpEC, the methods here can also be used for binaries containing neutron stars and in other NR codes.

The improvements discussed here deal with the eccentricity measurement stage of Fig. 2.1. Measurement of eccentricity from a binary evolution is an active research problem. Current approaches include fitting an analytic model to either the waveform or kinematic output [7], or constructing a definition for eccentricity based on waveform properties or the inspiral energetics [46, 4]. Note that eccentricity measurements that use kinematic output such as trajectories require less evolution time than those that need to run long enough to extract waveform information at the outer boundary. This computational cost can be significant depending on the number of iterations that the algorithm requires.

Eccentricity measurement in SpEC involves extracting coordinate trajectories of BHs from an NR simulation, computing the orbital angular velocity  $\Omega(t)$  from the trajectories, fitting its time derivative  $\dot{\Omega}(t)$  to a PN-inspired formula (Eq. (2.10) below) that involves the eccentricity, and reading off the eccentricity from the fit. Before our improvements, the implementation of this procedure was not very robust. For example, small changes in the time interval over which  $\dot{\Omega}(t)$  is fit or small changes in the initial guesses for the fit parameters often led to large changes in the measured eccentricity. Occasionally, the fitting procedure completely failed to converge. We show below that our changes greatly improve the robustness of the algorithm.

This chapter is organized as follows. In Sec. 2.2, we first describe how eccentricity reduction is currently performed in the SpEC code, and then present several new techniques to address the shortcomings of the current method. In Sec. 2.3, we apply these techniques to the SXS public waveform catalog [6] and compare the consistency of measured eccentricities with that of the current eccentricity reduction method. Finally, we summarize our findings in Sec. 2.4. We adopt the unit convention  $G = c = 1$ .

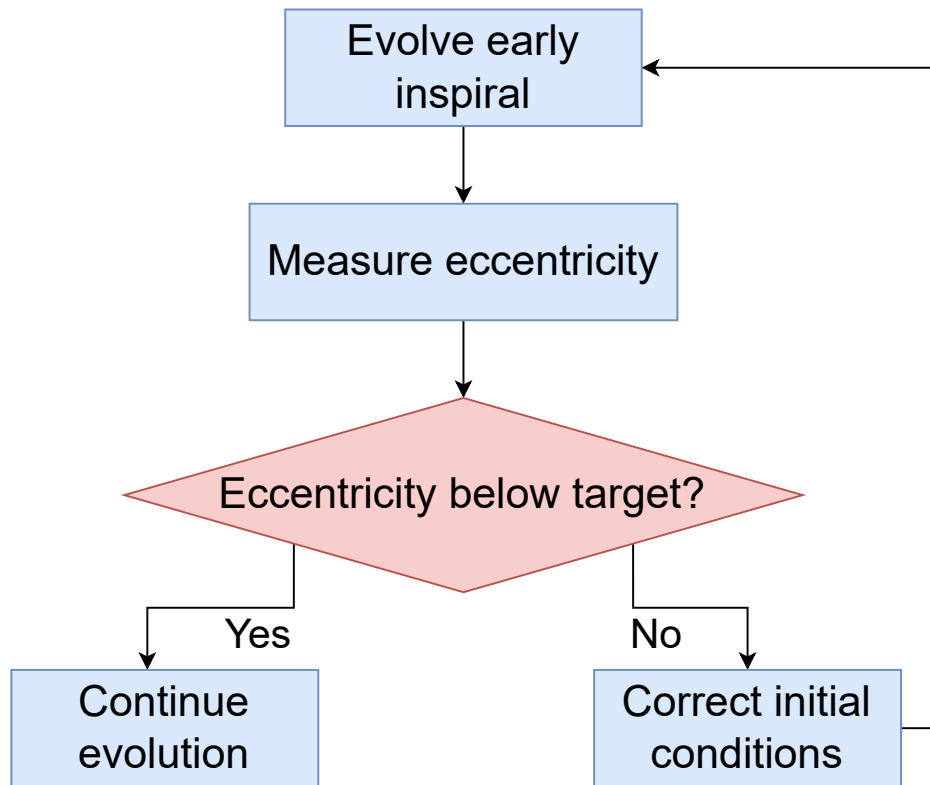


Figure 2.1: A simplified schematic of how quasicircular binary evolutions are achieved in NR codes. After the inspiral has run for 1–2 orbital periods after gravitational wave junk radiation, the trajectory is fit to the model in Eq. (2.10) and an estimate of the eccentricity is calculated as a derived quantity from the fit parameters. If the eccentricity is below a set target value, the evolution is continued. Otherwise, the initial conditions are updated using the formulation in Eq. (2.13) and a new evolution is started. This cycle of restarting evolution with updated initial conditions typically needs to be repeated multiple times in order to achieve an eccentricity of order  $10^{-4}$ .

## 2.2 Methods

### 2.2.1 Current eccentricity reduction method

Here we outline the method that is currently used for eccentricity reduction in SpEC. This method is described in more detail in Ref. [7].

To start a binary evolution at some initial time, one must specify the positions and the velocities of the objects at that time. Without loss of generality, we assume the two objects are initially on the positive and negative  $x$  axis with initial positions  $\vec{x}_1(0)$  and  $\vec{x}_2(0)$ , and their initial velocities  $\dot{\vec{x}}_1(0)$  and  $\dot{\vec{x}}_2(0)$  are in the  $xy$  plane. Given  $\vec{r}(t) = \vec{x}_1(t) - \vec{x}_2(t)$  and  $\dot{\vec{r}}(t) = \dot{\vec{x}}_1(t) - \dot{\vec{x}}_2(t)$ , we then specify the initial coordinate distance  $r_0 = |\vec{r}(0)|$  between the objects, the radial velocity  $\dot{r}_0 = (\vec{r}(0) \cdot \dot{\vec{r}}(0))/r_0$ , and the initial orbital frequency  $\Omega_0 = \Omega(0)$  of the binary. Orbital frequency can be defined as

$$\Omega(t) = \frac{|\vec{r} \times \dot{\vec{r}}|}{r^2}. \quad (2.1)$$

For a Newtonian binary, a circular orbit would be achieved by setting  $\dot{r}_0 = 0$  and setting  $r_0$  and  $\Omega_0$  according to Kepler's law. For a relativistic binary, there are no true circular orbits because of radiation reaction. One can write PN expressions for a choice of  $\dot{r}_0$ ,  $r_0$ , and  $\Omega_0$  that achieves a quasicircular orbit [2, 19, 8], but these expressions do not account for possible gauge differences between PN and NR.

Therefore, as described above, we use the iterative procedure summarized in Figure 2.1: we guess values of  $\dot{r}_0$ ,  $r_0$ , and  $\Omega_0$  (typically using low-order PN), evolve for a few binary orbits, and measure the eccentricity. We then use this measurement to update the values of  $\dot{r}_0$ ,  $r_0$ , and  $\Omega_0$  for the next iteration. The procedure stops when the eccentricity is below some tolerance, at which point we evolve to the desired final time.

For each step in the iterative procedure, initial data is generated from the given  $r_0$ ,  $\dot{r}_0$ , and  $\Omega_0$  values using an initial data solver such as Spells [37]. The initial data is numerically evolved through early inspiral, and the eccentricity is then measured using the extracted time series of orbital frequency  $\Omega(t)$  and its first time derivative  $\dot{\Omega}(t)$ . These quantities are computed from the coordinate trajectories of the centers of the apparent horizons. An alternative would be to compute the eccentricity from the gravitational waveform. However, using the coordinate trajectories has the advantage of requiring fewer orbits (and less simulation run time) than a method

based on waveform data. Using waveform data would require running the simulation long enough for the signal to propagate to a region far from the source where the waveform can be measured. We expect that the difference between eccentricity measured from the trajectory and measured from the waveform to be unimportant for the purposes of eccentricity reduction.

For eccentricity estimation and corrections to the initial data parameters, we use the formulation described in Ref. [7]; for clarity, we will outline it here.

Updates to the initial data parameters require three quantities that are not directly output by the simulation: initial eccentricity  $e$ , frequency of eccentricity-induced oscillations  $\omega$ , and initial mean anomaly  $\phi_0$ . These three quantities are estimated by fitting a phenomenological model to the time derivative of the orbital frequency.

In the derivation of updating formulae, we follow the  $\dot{\Omega}(t)$  model of Ref. [7], which holds for low eccentricity. For small  $e$ , Newtonian mechanics gives as the relation between  $\dot{\Omega}$  and  $e$

$$\Omega(t) = \bar{\Omega} + 2e\bar{\Omega} \sin(\omega t + \phi_0), \quad (2.2)$$

$$\dot{\Omega}(t) = 2e\bar{\Omega}\omega \cos(\omega t + \phi_0), \quad (2.3)$$

where  $\Omega(t)$  is the time-dependent orbital frequency and  $\bar{\Omega}$  is the mean value of orbital frequency (i.e., without eccentricity or spin-induced oscillations). Including additional terms for radiation reaction and spin-spin interaction, the eccentricity estimator model becomes

$$\dot{\Omega}(t) = S_{\Omega}(t) + 2e\bar{\Omega}\omega \cos(\omega t + \phi_0) - \frac{\bar{\Omega}}{M^2\bar{r}} F \sin(2\bar{\Omega}t + \gamma), \quad (2.4)$$

where  $S_{\Omega}(t)$  characterizes the non-oscillatory increase in mean value of  $\dot{\Omega}(t)$  resulting from radiative energy loss during inspiral,  $M = m_1 + m_2$  is the total mass of the binary, and  $\bar{r}$  is the mean value of separation. The last term in Eq. (2.4) accounts for eccentricity-independent oscillations in  $\dot{\Omega}(t)$  caused by spin-spin interactions. The quantity  $F$  is defined by

$$F = (\vec{S}_0 \cdot \hat{n}_0)^2 + (\vec{S}_0 \cdot \hat{\lambda}_0)^2, \quad (2.5)$$

where  $\vec{S}_0 = \left(1 + \frac{m_2}{m_1}\right) \vec{S}_1 + \left(1 + \frac{m_1}{m_2}\right) \vec{S}_2$  is the initial total spin vector, and

$$\hat{n}(t) = \frac{\vec{r}}{r}, \quad \hat{L}_N(t) = \frac{\vec{r} \times \dot{\vec{r}}}{|\vec{r} \times \dot{\vec{r}}|}, \quad \hat{\lambda}(t) = \hat{L}_N \times \hat{n}, \quad (2.6)$$

$$\hat{n}_0 = \hat{n}(0), \quad \hat{L}_{N0} = \hat{L}_N(0), \quad \hat{\lambda}_0 = \hat{\lambda}(0), \quad (2.7)$$

so  $\hat{L}_N$  is orthogonal to the instantaneous orbital plane. The quantity  $\gamma$  is defined such that

$$\sin \gamma = \cos \alpha \sin \alpha, \quad (2.8)$$

$$\cos \alpha \equiv \frac{\vec{S}_0 - (\vec{S}_0 \cdot \hat{L}_{N0}) \hat{L}_{N0}}{\left| \vec{S}_0 - (\vec{S}_0 \cdot \hat{L}_{N0}) \hat{L}_{N0} \right|} \cdot \hat{n}_0, \quad (2.9)$$

where Eq. (2.9) defines  $\alpha$ . Given that the final term in Eq. (2.4) is included only to capture spin-induced effects, the second term captures the full contribution to  $\dot{\Omega}(t)$  from eccentricity. The goal of eccentricity reduction is then to modify the initial data parameters  $\dot{r}_0$ ,  $r_0$ , and  $\Omega_0$  so that the second term in Eq. (2.4) vanishes, and therefore  $e = 0$  in the Newtonian limit.

For curve fitting, we use a form of Eq. (2.4) with simplified prefactors for the sinusoidal terms,

$$\begin{aligned} \dot{\Omega}(t) = & A (T_c - t)^{-11/8} + B (T_c - t)^{-13/8} \\ & + C \cos(\omega t + at^2 + \phi_0) - D \sin(\bar{\alpha}(t) + \phi_s), \end{aligned} \quad (2.10)$$

$$\cos \bar{\alpha}(t) \equiv \frac{\vec{S}_0 - (\vec{S}_0 \cdot \hat{L}_N) \hat{L}_N}{\left| \vec{S}_0 - (\vec{S}_0 \cdot \hat{L}_N) \hat{L}_N \right|} \cdot \hat{n}. \quad (2.11)$$

Here the first two terms describe radiation reaction [7], and are equivalent to  $S_\Omega(t)$  in Eq. (2.4). The final term in Eq. (2.10) is equivalent to the final term in Eq. (2.4), and captures oscillations from spin-spin interactions<sup>1</sup>. For nonspinning binaries, this term goes to zero and should be omitted from fitting. Our goal is to fit the derivative of the orbital frequency, as obtained from an NR simulation, to Eq. (2.10). This fit has nine unknown parameters to be determined:  $A$ ,  $B$ ,  $C$ ,  $D$ ,  $T_c$ ,  $\omega$ ,  $a$ ,  $\phi_0$ , and  $\phi_s$ .

From Eq. (2.4) and the parameters found by fitting to Eq. (2.10), eccentricity is estimated as

$$e = \frac{C}{2\bar{\Omega}\omega}, \quad (2.12)$$

following from the Newtonian definition of eccentricity and Eq. (2.4).  $\Omega_0$  is used as an approximation in place of  $\bar{\Omega}$  for the following results.

<sup>1</sup>It can be shown that  $\sin 2\bar{\alpha} = 2 \sin(2\bar{\Omega}t + \gamma)$ .

The resulting updating formulae, as detailed in Ref. [7], are

$$\Delta \dot{r}_0 = \frac{C}{2\Omega_0} \cos \phi_0, \quad (2.13a)$$

$$\Delta \Omega_0 = -\frac{C\omega}{4\Omega_0^2} \sin \phi_0. \quad (2.13b)$$

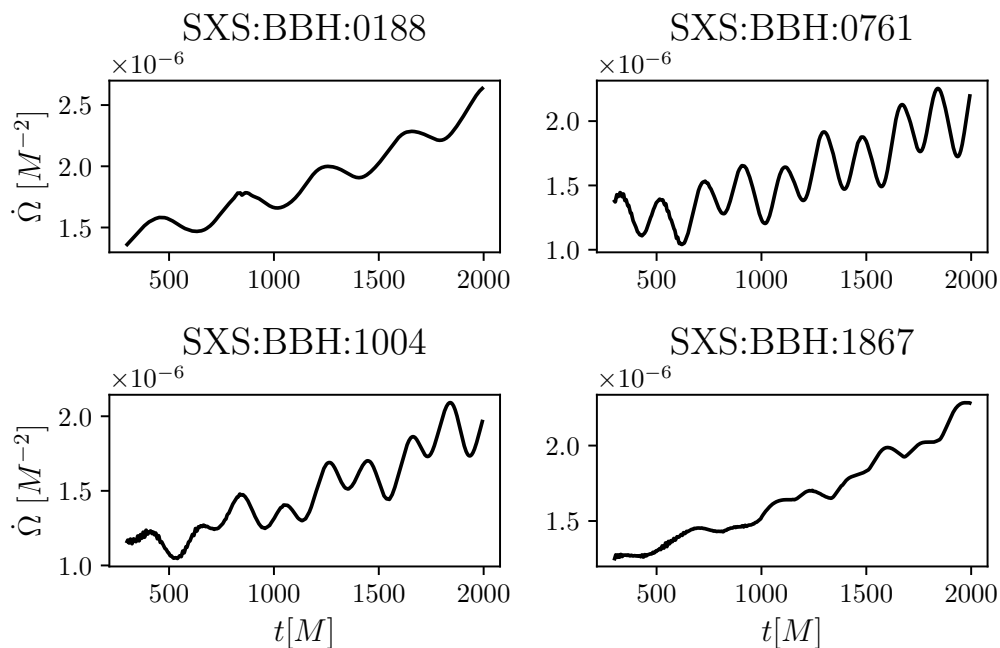
In the above discussion, we choose to fix  $r_0$  and update  $\dot{r}_0$  and  $\Omega_0$ . Alternatively, one can choose to fix  $\Omega_0$  and update  $r_0$  and  $\dot{r}_0$  instead, using a similarly derived update formula for  $r_0$ . One variable is fixed in order to set the scale of the orbit, and the other two are corrected to determine other features of the orbit.

Here we collect certain symbol definitions for clarity. The variable  $\Omega_0$  is the initial orbital frequency, an initial condition specified in the elliptic solver for initial data, and updated through Eq. (2.13b). The variable  $\Omega(t)$  refers to the orbital frequency time series obtained by numerical evolution, that is then fit to the form of Eq. (2.10). The variable  $\omega$  is the frequency of oscillations in  $\Omega(t)$  that are induced by eccentricity, and is a fit parameter in Eq. (2.10). The variable  $\bar{\Omega}$  is the mean value of  $\Omega$ .

## 2.2.2 Improved algorithm for eccentricity fitting

Overall, the method described in Sec. 2.2.1 works reasonably well, and has been used to reduce eccentricity for all of the non-eccentric NR simulations in the SXS simulation catalog [6]. However, we have found that a key step in the method, fitting NR trajectories to Eq. (2.10), is not very robust and is often the limiting factor that determines how small an eccentricity can be obtained. In particular, standard nonlinear fitting methods sometimes fail to converge when fitting to Eq. (2.10), and even worse, the results of the fit are sometimes extremely sensitive to small details such as the time interval chosen for fitting. These problems are related to the large number of nonlinear fit parameters in Eq. (2.10), and to the difficulties in choosing initial guesses for these parameters.

In this section, we propose some new techniques to mitigate these problems and thus improve the robustness of eccentricity measurement. First, we detail a new frequency-domain method for removing spin-spin oscillations from  $\dot{\Omega}(t)$ . This method allows  $\dot{\Omega}(t)$  to be fit to a simpler function that has fewer fit parameters, and it provides a better initial guess for the fit parameter  $\omega$ . We then briefly introduce the variable projection algorithm [16] for solving nonlinear least squares problems



	$q$	$e \times 10^4$	$\vec{\chi}_1$	$\vec{\chi}_2$
SXS:BBH:0188	7.187	1.609	(0, 0, 0)	(0, 0, 0)
SXS:BBH:0761	2.0	1.923	(-0.63, -0.49, 0)	(0, 0, 0)
SXS:BBH:1004	1.602	2.939	(-0.17, 0.41, -0.57)	(-0.49, -0.48, 0.21)
SXS:BBH:1867	3.464	0.695	(0, -0.16, 0)	(-0.20, 0.17, -0.23)

Figure 2.2: Some  $\dot{\Omega}(t)$  trajectories from public SXS BBH simulations. The quantity  $\dot{\Omega}(t)$  generally increases during inspiral, but both eccentricity and spin-spin precession can induce oscillations. Models such as that described in Sec. 2.2.1 measure eccentricity by characterizing these oscillations. The spin-spin oscillations occur at about twice the frequency of the eccentricity-induced oscillations, so spin-spin effects could be accounted for either by fitting for them (i.e., the last term in Eq. (2.10)), or by removing them via a low-pass filter. In nonspinning simulations such as SXS:BBH:0188, only eccentricity-induced oscillations are present.

and show how this algorithm can reduce the number of nonlinear parameters in the fit. Next, we discuss the choice of initial guesses for the fit parameters, why the results of the previous method are sensitive to this choice, and how this choice can be improved through the use of variable projection and frequency-domain filtering.

### 2.2.2.1 Frequency domain pre-processing

The last term in Eq. (2.10) describes oscillations caused by spin-spin interactions. However, the parameters in that term do not enter into the measurement of the eccentricity or the updating formulas for  $\Omega_0$  and  $\dot{r}_0$ —that term and its two fit parameters are present solely to model an effect that we subtract out. We can take advantage of this to simplify Eq. (2.10). The last term in Eq. (2.10) describes oscillations in  $\dot{\Omega}(t)$  with roughly twice the frequency of the oscillations caused by eccentricity (recall that  $\omega$ ,  $\Omega_0$ , and  $\bar{\Omega}$  are all equal in the Newtonian limit for small eccentricity). Figure 2.2 shows a small selection of  $\dot{\Omega}(t)$  trajectories extracted from simulations in the SXS public catalog [6, 47]. Notice that simulations SXS:BBH:0761, SXS:BBH:1004, and SXS:BBH:1867, which have significant precessing spins, have a much more complicated  $\dot{\Omega}(t)$  with higher frequencies than does SXS:BBH:0188, which has no spins. The higher frequency of spin-spin interactions suggests that we can remove the spin-spin term in Eq. (2.10) if we first apply an appropriate low-pass filter to the frequency spectrum of  $\dot{\Omega}(t)$ .

To perform a low-pass filter, we first compute the power spectrum of  $\dot{\Omega}(t)$ . To do this, the time series  $\dot{\Omega}(t)$  must be preprocessed before taking a Fourier transform. This is because  $\dot{\Omega}(t)$  is nonperiodic and its mean value increases over the course of inspiral. Here, we detail the preprocessing steps we have used.

First, we must account for the average increase in  $\dot{\Omega}$  over time. This trend is caused by radiation reaction, and we can approximate it as a linear process because of the short timescale of the part of the signal that we will fit to. Thus we fit a linear trend to  $\dot{\Omega}(t)$  and subtract it off. We then apply a window function to the interval of the signal being fit to mitigate the Gibbs phenomenon [54]. Empirically we find that a Hamming window [18] is particularly effective in preserving the underlying signal structure. The resulting time series is then zero-padded on both sides to increase frequency-domain resolution. For a time series with time steps of size  $\sim 10^{-1}M$ , we note that  $\sim 10^4$  zeros on each end gives a frequency resolution  $\sim 10^{-3} M^{-1}$ , which we find is sufficient to resolve important features in the frequency domain. Figure 2.3

shows an  $\dot{\Omega}$  trajectory extracted from an SXS public catalog simulation [6] and transformed into the frequency domain using the process described above.

Now we turn to the low-pass filter, which we use to remove spin-spin oscillations in  $\dot{\Omega}(t)$  and simplify Eq. (2.10) by dropping the final term. In Fig. 2.3, the spin-spin oscillations correspond to the peak at  $2\pi f \approx 3.5 \times 10^{-2} M^{-1}$  in the right panel. To perform the low-pass filter, we choose a cutoff frequency at the first local minimum that occurs after the dominant frequency peak. In Fig. 2.3, this cutoff frequency occurs at  $2\pi f \approx 2.5 \times 10^{-2} M^{-1}$ . We then set  $\tilde{\Omega}$  to zero for all frequencies greater than this cutoff. The new spectrum is then inverse transformed to give a filtered time domain  $\dot{\Omega}(t)$  usable for fitting. This filtered  $\dot{\Omega}(t)$  is shown as the blue curve in the left panel of Fig. 2.3. We find that fitting to the filtered  $\dot{\Omega}(t)$ , ignoring the final term in Eq. (2.10), produces approximately the same value of eccentricity as fitting to the original  $\dot{\Omega}(t)$  and keeping the final term in Eq. (2.10).

In addition to removing the spin-spin oscillations, the low-pass filter also removes higher overtones in  $\dot{\Omega}$  and also high-frequency numerical noise, both of which are unmodeled by Eq. (2.10) and can interfere with the robustness of fitting. Thus the low-pass filter technique improves the eccentricity measurement algorithm on several fronts.

### 2.2.2.2 Initial guesses for fit parameters

The nonlinear least squares methods used for fitting  $\dot{\Omega}(t)$  to Eq. (2.10) are iterative: Initial guesses for the nonlinear fit parameters are provided, and the method refines those initial guesses multiple times until convergence is achieved. Care must be taken to choose accurate initial guesses, because inaccurate initial guesses can lead to convergence in local minima. Figure 2.4 shows slices in the solution space of Eq. (2.10) for the parameter  $\omega$ . The cost function is computed for an analytically generated sample dataset, and each curve shown uses a different length in time of sample data. For parameters  $\omega$  and  $a$  (not shown), both of which enter as cosine arguments, there are many local minima near the global minimum. Moreover, the larger the time interval over which  $\dot{\Omega}(t)$  is fit, the more local minima are present, and the closer they are to the desired global minimum. This trend means that counterintuitively, fitting over a longer inspiral does not necessarily translate to finding a more accurate solution. However, inclusion of at least one full orbital period is crucial for determining an optimal value of  $\omega$ .

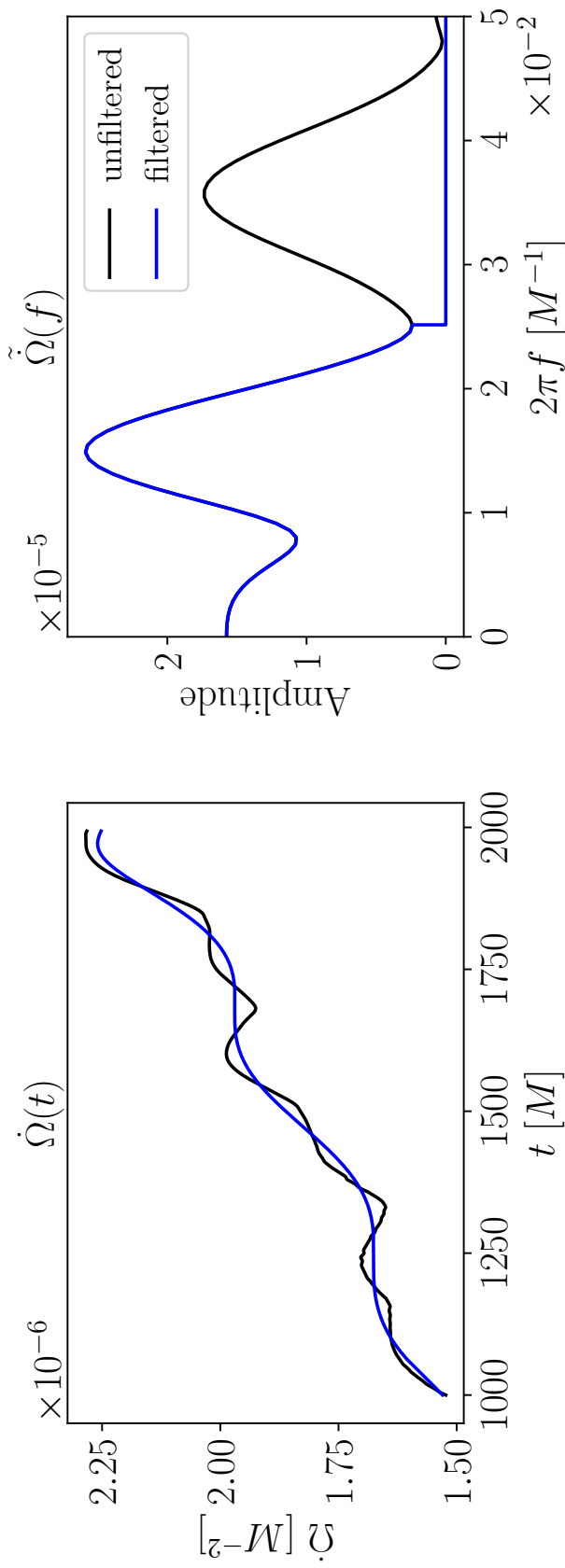


Figure 2.3: The  $\dot{\Omega}$  time series from SpEC BBH run SXS:BBH:1867 and its corresponding frequency spectrum. The black curves correspond to the original data and the blue curves correspond to the data after removing high frequency content as outlined in Sec. 2.2.2.1. The dominant frequency corresponds to eccentricity-induced oscillations, and can be used as an initial guess for the fit parameter  $\omega$ . Since the computed updates in Eq. (2.13) only depend on the dominant frequency, higher frequency content can be removed to simplify fitting (by dropping the last two terms in Eq. (2.14)) without significantly impacting the relevant fit parameters.

Empirically, we observe that the guess for  $\omega$  is the most important factor in guaranteeing that we converge to the global minimum. The typical total time interval used for fitting, roughly one to two orbital periods, is too small to allow for high resolution of  $T_c$  or  $a$ , and neither  $T_c$  nor  $a$  appear in the formula for eccentricity or the updating formulas. As Fig. 2.5 shows, the value of the  $\omega$  guess has a large impact on the quality of the resulting fits, regardless of the fitting technique used. A poor guess for  $\omega$  can result in a fit that entirely fails to capture the primary oscillations in  $\dot{\Omega}(t)$  caused by eccentricity.

For the previous method of eccentricity reduction described in Sec. 2.2.1, the difficulty of choosing accurate initial guesses typically prevents brute-force fitting to Eq. (2.10). Instead, the algorithm proceeds with a series of models and fits, where the first fit in the series uses a model consisting only of a few terms in Eq. (2.10) and therefore fewer parameters. The next fit adds another term and more parameters to the model, and uses the results of the previous fit to provide initial guesses for the parameters. This process continues until the final fit uses all terms in Eq. (2.10). Each intermediate fit effectively functions as a search for an accurate initial guess for one or more new parameters.

We employ three strategies to tackle the problem of initial guesses. The first strategy, discussed above in Sec. 2.2.2.1, is to simplify the fitting function by filtering, so that the last term of Eq. (2.10), and the corresponding parameters that need initial guesses, can be dropped. The second strategy, discussed in Sec. 2.2.2.3 below, is to use a fitting technique called *variable projection*, which solves for a subset of the parameters using *linear* least squares and therefore does not require initial guesses for them. As we will show below, the use of variable projection means that initial guesses are required for only  $T_c$ ,  $\omega$ , and  $a$ . The third strategy is used for the parameter  $\omega$ , which empirically we have found is the one that needs the most accurate initial guess. We obtain the initial guess for  $\omega$  from the frequency spectrum  $\tilde{\Omega}$  that we computed in Sec. 2.2.2.1. In particular, we choose  $\omega$  as the center of the initial peak in  $\tilde{\Omega}$ . Care must be taken to correctly identify this frequency. We use a standard peak-finding routine (e.g. `scipy.signal.find_peaks` [53]) on the amplitude spectrum, with a limit on the minimum amplitude allowed, and restrict the peak search to local maxima in a bandwidth of  $\Omega_0 \pm 40\%$ . For the simulation shown in Fig. 2.3,  $\Omega_0 = 1.69 \times 10^{-2} M^{-1}$ , and the dominant frequency in  $\tilde{\Omega}$  is  $1.49 \times 10^{-2} M^{-1}$  in the right panel of the figure. This frequency is in the search bandwidth and would be chosen as the initial guess. Rarely, there may be no peak in

this range, or else multiple peaks of comparable amplitude, in which case no guess can be extracted from  $\tilde{\Omega}$ . In that case, we default to choosing  $\omega$  to be  $0.8\Omega_0$ , a value that was chosen by trial-and-error. In the few cases we have seen of this failure mode, it indicates that the eccentricity is too small to measure reliably. We find that when an initial guess for  $\omega$  can be obtained from the frequency spectrum, it offers an improvement over the previous trial-and-error method, as shown in Fig. 2.5.

Two other parameters,  $T_c$  and  $a$ , require initial guesses. The guess for  $T_c$  is approximated from the quadrupole formula. Because  $a$  is typically at a much smaller scale than the other fit parameters, we find  $a = 0$  to be an adequate initial guess.

### 2.2.2.3 Variable projection

As discussed in Sec. 2.2.2.4, Eq. (2.10) is an especially challenging nonlinear least squares problem. Much of this difficulty can be removed by noting that Eq. (2.10) leads to a separable least squares problem, that is, some of the parameters in the fit enter the model linearly while others are nonlinear.

The “best” algorithm for separable problems has been known for a long time, since 1973 [16], and is called variable projection. It was implemented originally in a Fortran code called VARPRO [15]. The idea is to start with initial guesses only for the nonlinear parameters. Then standard linear least squares solves for the linear parameters by the usual analytic process. Next, an iterative nonlinear fitting routine updates the nonlinear parameters with the linear parameters held fixed. The whole procedure is then iterated until a suitable tolerance is achieved. The clever part of the algorithm is that the Jacobian of the cost function with respect to the nonlinear parameters that is used in the nonlinear fitting has a dependence on the linear parameters. This is because the nonlinear parameters depend implicitly on the linear ones. Ref. [16] worked out this contribution to the Jacobian—it can be computed explicitly from the analytic solution of the linear least-squares problem using linear algebra techniques. In general, this algorithm is never worse than brute-force nonlinear least squares fitting, and often succeeds when brute force fails. A major reason for this is the reduced dimensionality of the nonlinear part of the fitting.

In the case of Eq. (2.10), the nonlinear parameters in the model are  $\omega$ ,  $T_c$ ,  $a$ ,  $\phi_0$ , and  $\phi_s$ , while  $A$ ,  $B$ ,  $C$ , and  $D$  are the linear parameters. To get the maximum benefit out of variable projection, one should reparameterize the model so that as many parameters

as possible enter linearly. For example, a term of the form  $C \cos(\omega t + \phi_0)$  should be rewritten as  $C \cos \phi_0 \cos(\omega t) - C \sin \phi_0 \sin(\omega t)$ . This avoids having to treat  $\phi_0$  as a nonlinear parameter. We will do this below in recasting Eq. (2.10) to Eq. (2.14).

In this work, we have relied on a modern implementation of VARPRO [29] in Matlab. We have translated this code into Python so that it can use the nonlinear solvers available in Scipy. This Python version is publicly available at Ref. [52].

#### 2.2.2.4 New fitting formula for $\dot{\Omega}(t)$

Eq. (2.10) can be rewritten as

$$\begin{aligned} \dot{\Omega}(t) = & A (T_c - t)^{-11/8} + B (T_c - t)^{-13/8} \\ & + \bar{C}_1 \cos(\omega t + at^2) \\ & - \bar{C}_2 \sin(\omega t + at^2) \\ & - \bar{D}_1 \cos(\bar{\alpha}(t)) - \bar{D}_2 \sin(\bar{\alpha}(t)), \end{aligned} \quad (2.14)$$

where we have absorbed factors of  $\cos \phi_0$ ,  $\cos \phi_s$ , etc., into new parameters  $\bar{C}_1$ ,  $\bar{C}_2$ ,  $\bar{D}_1$ , and  $\bar{D}_2$ . This substitution eliminates two nonlinear parameters ( $\phi_0$  and  $\phi_s$ ) in favor of two extra linear parameters, so that there are now six linear parameters and three nonlinear parameters as opposed to four linear parameters and five nonlinear parameters. Note that we have retained the spin-spin terms, the ones with coefficients  $\bar{D}_1$  and  $\bar{D}_2$ , for completeness, although in practice we can omit these terms as long as we filter out the corresponding effects according to the procedure in Sec. 2.2.2.1.

With variable projection, Eq. (2.14) requires guesses only for  $T_c$ ,  $\omega$ , and  $a$ , so we have reduced the nonlinear fit to three dimensions instead of the original nine. Note that only the magnitude of  $C$  (not  $\bar{C}_1$  or  $\bar{C}_2$ ) appears in the correction formulae Eq. (2.13) and the eccentricity formula Eq. (2.12), and  $C$  is easily computed by  $C^2 = \bar{C}_1^2 + \bar{C}_2^2$ .

For all analyses in the following section, we drop the  $B (T_c - t)^{-13/8}$  term from Eqs. (2.10) and (2.14) for fitting. We find that the degeneracy in the  $A$  and  $B$  parameters contributes some inconsistency to the fit solution, and this term is difficult to resolve in a trajectory only 1-2 orbits long. It is possible that fitting over a longer time span, where radiation reaction has a bigger effect, might require keeping this term.

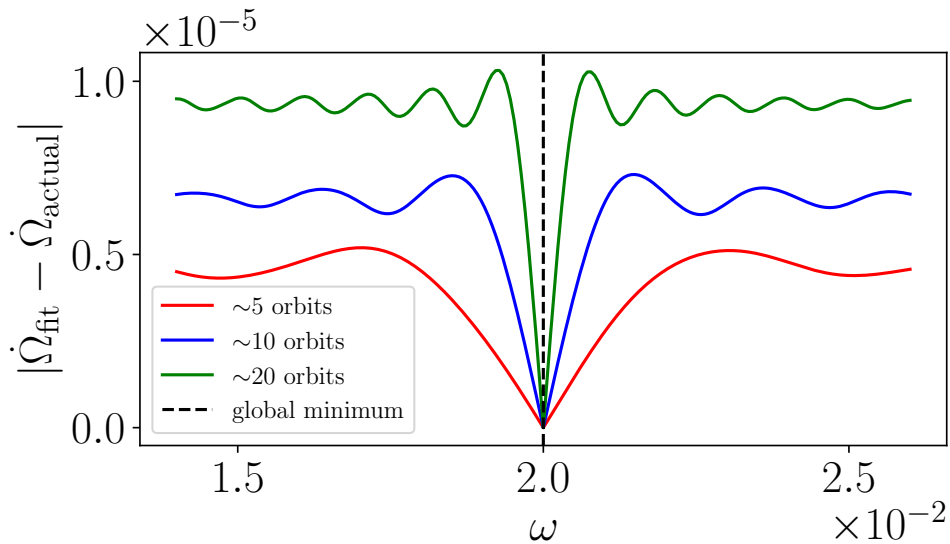


Figure 2.4: The cost function for Eq. (2.10) with a single parameter varied and all others left constant, calculated using trajectories of varying length. The residual curve of  $\omega$ , an argument for the sinusoidal components of Eq. (2.10), contains several local minima near the global minimum. Furthermore, these local minima become closer and more numerous if time window length is increased. Optimizing Eq. (2.10) requires navigating around such local minima.

## 2.3 Robustness test

Here we compare the consistency of eccentricity measurements made both with and without our improved fitting algorithm. We apply our methods first to an analytic trajectory, then to simulations from the SXS public waveform catalog [6, 47].

A key motivation for improving our algorithm is that the original method described in Sec. 2.2.1 is extremely sensitive to the time interval  $[t_{\min}, t_{\max}]$  used for the fit. Consider Fig. 2.6, which shows best fit parameters to an analytic  $\dot{\Omega}(t)$ . The  $\dot{\Omega}(t)$  used in Fig. 2.6 is a function that obeys Eq. (2.10) exactly, and is given as follows:

$$\begin{aligned} \dot{\Omega}(t) = & 0.287 (13000 - t)^{-11/8} + \\ & (1.44 \times 10^{-7}) \cos(0.013t + (1.80 \times 10^{-7})t^2 + 4.68) \\ & + N(t), \end{aligned} \quad (2.15)$$

where  $N(t)$  is noise from a Gaussian distribution with a width of  $10^{-8}$ . The red crosses in Fig. 2.6 show the best fit parameters of Eq. (2.10) for this  $\dot{\Omega}(t)$ , but as a function of  $t_{\min}$  (with  $t_{\max}$  set such that  $t_{\max} - t_{\min}$  is the same for each point).

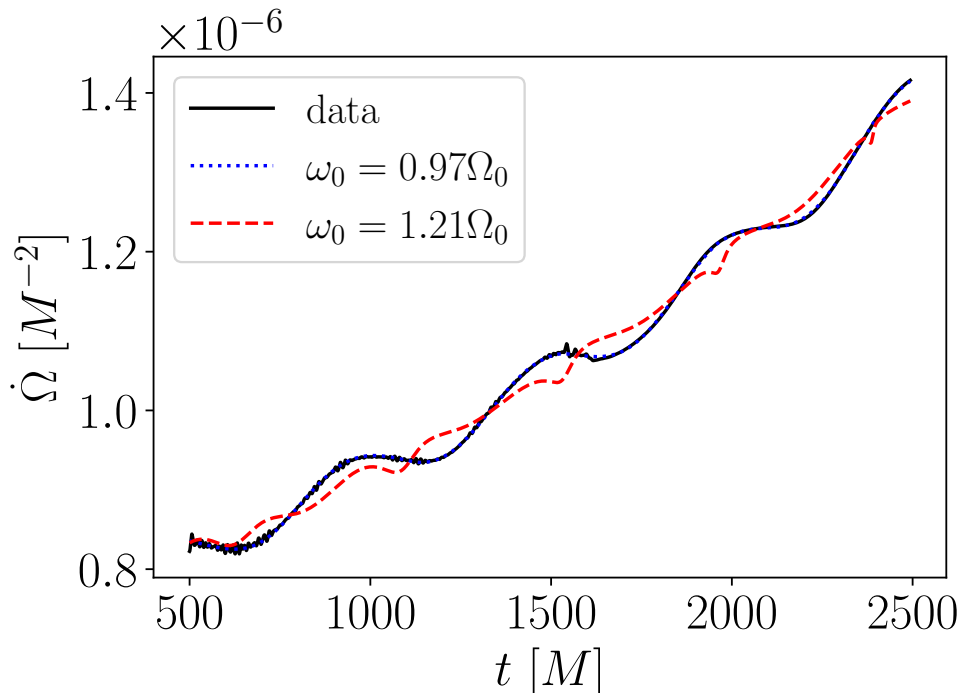


Figure 2.5: An  $\dot{\Omega}$  time series for an equal mass, nonspinning BBH numerically simulated using SpEC (SXS:BBH:2085) and resulting curves of best fit found using variable projection for different initial guesses of  $\omega$ . In particular, the fit in blue (barely visible over the black curve) uses a guess for  $\omega$  found from the dominant peak in the Fourier transform of  $\dot{\Omega}$ , as described in Sec. 2.2.2.1 and 2.2.2.2. A small change in the value of this guess can greatly impact the quality of the resulting fit, to the extent that primary features are not captured, as in the red fit curve.

For the red crosses, we used the original fit method implemented in SpEC, the `scipy.optimize.minimize` [53] routine and a series of fits incrementally adding terms from Eq. (2.10). Small changes in  $t_{\min}$  (compared to the orbital period) can produce eccentricities that vary by large amounts, sometimes even by a factor of 2 or larger. This sensitivity is effectively a source of noise that limits our ability to accurately measure eccentricity, and this noise hampers the ability of the eccentricity reduction procedure to converge to a small value of eccentricity.

The blue circles in Fig. 2.6 are the same as the red crosses, except using the new techniques described in Sec. 2.2. When  $t_{\min}$  is shifted, best fit values from the previous method often jump discontinuously. Figure 2.7 is the same as Fig. 2.6 except that  $\dot{\Omega}(t)$  comes from unequal mass, spinning SpEC BBH simulation SXS:BBH:0235. We see that even with data from an NR simulation, the new method is significantly

less sensitive to  $t_{\min}$  than the previous method. In addition, Fig. 2.6 shows that the new method tends to converge to the correct solution more often. Overall, our proposed method gives considerable improvement in both consistency and accuracy over the previously used algorithm. Since variable projection is more successful than conventional algorithms at converging to global solutions [30], the local minima highlighted in Fig. 2.4 are one likely source of the previously observed inconsistency in measured eccentricity.

One measure of the sensitivity of the eccentricity measurement to the time interval  $[t_{\min}, t_{\max}]$  is to compute  $\sigma_e$ , the standard deviation of  $e$  as a function of  $t_{\min}$  (i.e. in the appropriate subplot of Fig. 2.7). For Fig. 2.7, this value is  $\sigma_e = 3.39 \times 10^{-6}$  for the previous method and  $\sigma_e = 2.47 \times 10^{-7}$  for the method described in this chapter. We now repeat Fig. 2.7 for all BBH simulations in the SXS public waveform catalog. The catalog currently consists of about 2300 precessing and nonprecessing BBH simulations covering a broad parameter space spanning mass ratios  $1 \leq q \leq 10$  and spin magnitudes  $0 \leq \chi_{\text{eff}} \leq 0.998$  [6]. We use simulations with a reference eccentricity  $e_{\text{ref}} < 3 \times 10^{-3}$ , totaling roughly 2200 runs. For each simulation in the catalog we compute  $\sigma_e$ , and we plot these values as a histogram in Fig. 2.8. We see a trend in that the best fit  $e$  with our proposed method is generally more consistent than with the implementation that is currently used in SpEC.

Another issue with the previously used routine is that it occasionally fails to converge to any solution during eccentricity reduction, often because of reaching a maximum number of iterations without satisfying any exit criteria. When this happens, initial data updates for eccentricity reduction cannot be computed at all. Variable projection converges more often and with fewer fitting iterations required. Several SpEC runs that previously failed because the fit during eccentricity reduction failed to converge succeed when variable projection is used in place of standard nonlinear least squares.

## 2.4 Conclusion

We have presented several improvements in an algorithm for reducing the orbital eccentricity of binary simulations in NR. Unlike in Newtonian physics, it is not straightforward in NR to specify initial orbital parameters that yield orbits with zero eccentricity. Instead, we use an iterative procedure, outlined in Fig. 2.1, in which eccentricity is estimated by doing a short evolution. If the estimated eccentricity is large, the initial data is corrected and the evolution is restarted. This process is

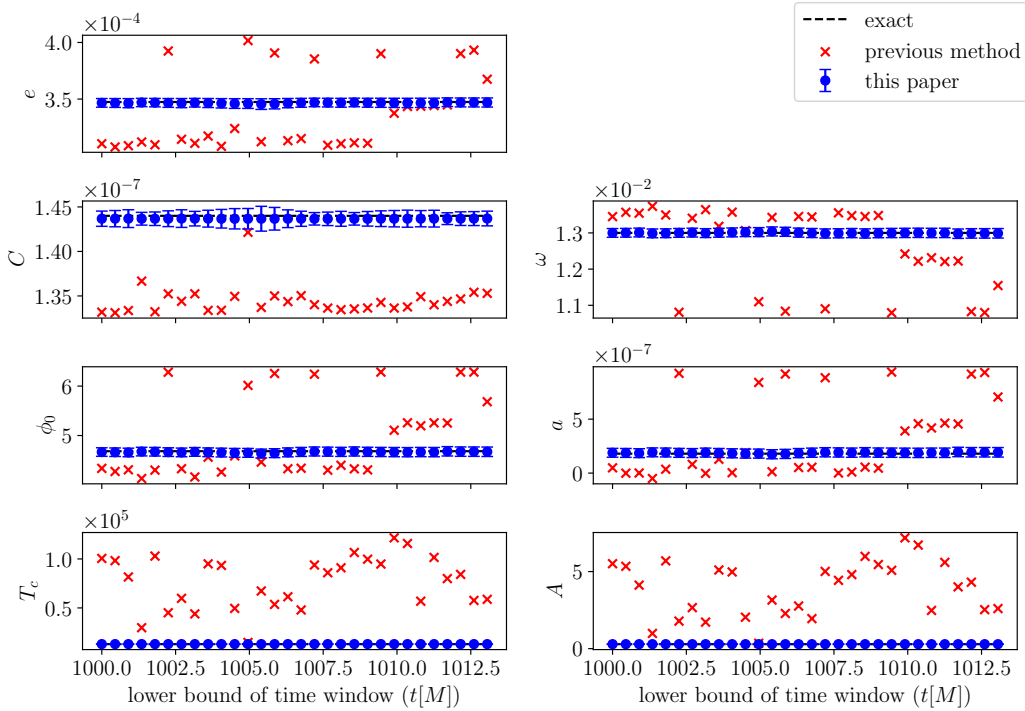


Figure 2.6: Best fit values for Eq. (2.10) (with the  $B$  term dropped) and calculated eccentricity versus fitting window placement. We performed this method comparison using an analytic time series, not an NR simulation. For each set of window bounds, a nonlinear fit was performed on a dataset generated by fixing the parameters of Eq. (2.10) to exact numerical values and adding Gaussian noise to each point in the time series. The same window size,  $900 M$  (roughly two orbital periods), and bounds were used for each method. Fits labelled “this paper” were done with Eq. (2.14) and initial guesses found using the method proposed in Sec. 2.2, and found values of  $\phi_0$  and  $B$  are derived. Error bars for these points are computed as the square root of the corresponding diagonal element in the covariance matrix. Fits labelled “previous method” were done with the previous implementation for eccentricity reduction found in SpEC. These points do not have error bars since error estimates are not implemented with this method. Ideally, the result of the fit should have little to no dependence on the fit cutoff times, so the expected curve for each parameter is a horizontal line at the exact value. However, because the model has so many parameters that require guesses, the previous method is quite sensitive to the time window and often converges to an incorrect value.

repeated until the measured eccentricity is acceptably low.

The eccentricity estimation step of this iterative procedure involves fitting the results of an NR simulation (in our case, the derivative of the orbital frequency  $\dot{\Omega}(t)$ ) to an estimator model, Eq. (2.10). Because the model has many parameters, some of which enter nonlinearly, the fit requires a nonlinear least squares algorithm, which in turn requires accurate initial guesses for the parameters so as to not fall into local minima of the cost function. The model and its solution method are sensitive to small details, and the previous method of eccentricity reduction used in SpEC, described in Sec. 2.2.1, occasionally fails to converge. It is sometimes possible to fix individual failures by hand, by fine-tuning parameters of the algorithm such as initial guesses. However, eccentricity reduction takes place as part of an automated pipeline that allows a single user to run dozens or hundreds of BBH simulations at once [6]. When running hundreds of simulations, even infrequent eccentricity reduction failures require significant human time to fix. A key goal of the new method presented here is to eliminate or at least reduce these failures.

We have found a number of new techniques that improve the reliability of best fit solutions for the eccentricity estimator first derived in Ref. [7]. Our main improvements can be summarized as follows:

1. An initial guess for the  $\omega_0$  fit parameter taken from the  $\dot{\Omega}$  frequency spectrum.
2. Use of variable projection for nonlinear least squares fitting and reparameterization of Eq. (2.10) into Eq. (2.14) for fitting in order to fully take advantage of variable projection. This effectively reduces the nonlinear least squares model from nine to three dimensions.
3. Removal of high frequency content before fitting, enabling the removal of an additional spin-spin precession term from the model.
4. Removal of a higher-order radiation-reaction term from the model when appropriate, to reduce degeneracy in fit parameters.

These methods are currently being integrated into the SpEC code as part of the automated pipeline, and will also see future use in the SpECTRE code [11]. Note that although these techniques have been implemented in SpEC, they are not specific to SpEC and can be used in other NR codes. Further testing is needed to determine how these improvements affect the efficacy of eccentricity reduction, i.e., the number of

iterations required for initial data correction to achieve low eccentricity (e.g. at or below  $O(10^{-4})$ ) and the lowest achievable eccentricity.

In general, we expect to see eccentricity reduction in the gravitational waveform corresponding to eccentricity reduction in the trajectory. Whether eccentricity in the waveform is more effectively reduced as a result of our improvements is an interesting question since the waveform strain is the relevant quantity used for comparisons with experimental observations. Variable projection and frequency preprocessing are techniques that can also be applied to eccentricity estimators using gravitational waveforms instead of trajectory time series. Specifically, variable projection is useful for fit models that include linear parameters, or nonlinear parameters that can be rewritten as a combination of linear parameters. Extension of this method to use gravitational waveforms as input instead of orbital trajectories could in principle be done as follows: first extract the time-dependent angular velocity from the waveform [5] and compute its time derivative  $\dot{\Omega}(t)$ , and then use that  $\dot{\Omega}(t)$  as input to this method. The reason we choose trajectories instead of gravitational waveforms here is computational efficiency: extracting the gravitational waveform during the eccentricity reduction procedure would mean that for each iteration, the ‘Evolve early inspiral’ step in Figure 2.1 would need to continue for additional orbits (and thus additional CPU time) so that the radiation has time to propagate from the near zone to the large radii where the waveform is measured. Also, because we do not generate waveforms during the eccentricity-reduction iterations, we have not explicitly looked at how eccentricities as measured from the waveform decrease during eccentricity reduction. Although one might expect that trajectories would contain gauge effects not present in the waveform, the NR community has consistently observed that NR trajectories behave ‘reasonably’, e.g. they agree with PN trajectories [33]; we expect that eccentricities measured from the waveform should roughly agree with those measured from the trajectories.

A related problem to eccentricity reduction is measurement of larger eccentricities and tuning of NR parameters to achieve a desired eccentric orbit. Just as eccentricity is iteratively reduced as described in Sec. 2.2.1, it can similarly be driven to a nonzero target value using an eccentricity estimator requiring a nonlinear fit. The model presented in Ref. [7] is derived in the limit of small  $e$ , so  $O(e^2)$  terms are dropped from Eq. (2.2). For large eccentricity, a more general functional form is used, and an additional parameter (the mean anomaly) must be specified. Application of the techniques introduced here has not been fully explored in this case. We note that

Ref. [25] introduces a new technique for larger eccentricities.

All testing presented here was done using BBH simulations. However, the eccentricity reduction method used here is not limited to black holes. The method as described in Sec. 2.2.1 is used in SpEC for BNS and BHNS simulations, so the improvements found here apply to those simulations as well.

## 2.5 Acknowledgments

This work was supported in part by the Sherman Fairchild Foundation, by NSF Grants PHY-2207342 and OAC-2209655 at Cornell, and by NSF Grants PHY-2309211, PHY-2309231, and OAC-2209656 at Caltech. Computations were performed at Caltech using the Wheeler cluster and Resnick HPC Center.

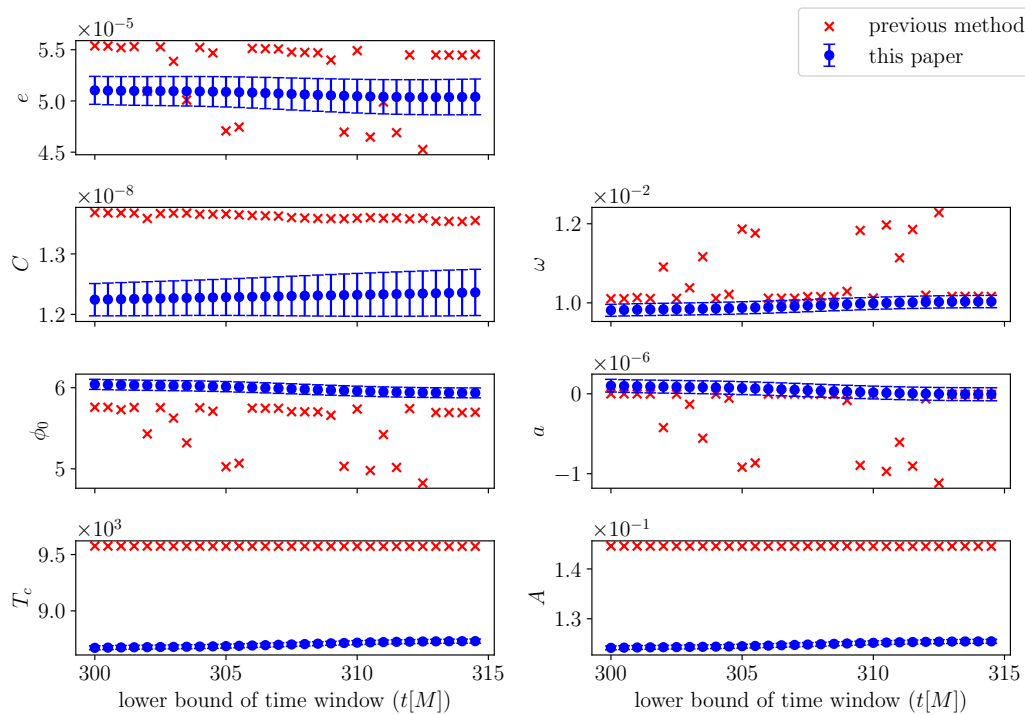


Figure 2.7: The same test as described in Fig. 2.6, using SpEC BBH trajectory SXS:BBH:0235 instead of an analytic dataset. Unlike in Fig. 2.6, an exact solution does not exist. For this test,  $t_{\max} - t_{\min}$  was set to  $1200 M$ , roughly two orbital periods.

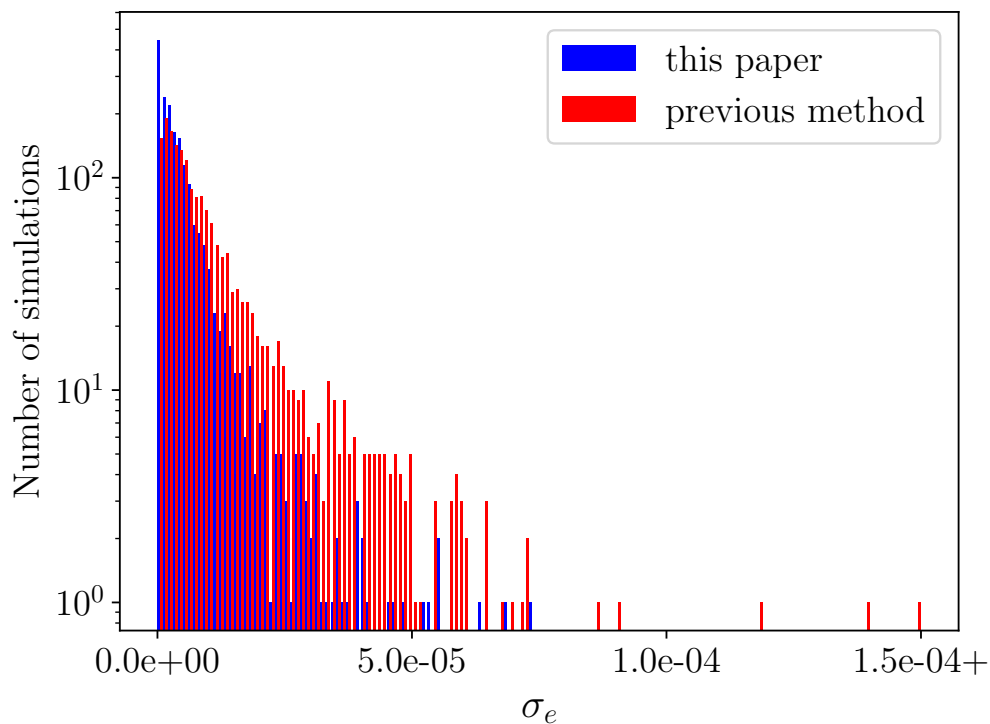


Figure 2.8: A histogram showing the standard deviation in fit  $e$  with respect to fit time windows,  $\sigma_e$ , for simulations from the SXS public catalog with  $e_{\text{ref}} < 3 \times 10^{-3}$ . For each simulation, the experiment in Fig. 2.7 was repeated, from which  $\sigma_e$  was then computed. We take this value as measure of fit consistency, and ideally it should be as close to 0 as possible. Bin width is  $1 \times 10^{-6}$ , and bin count corresponds to the number of simulations found to have  $\sigma_e$  within the bin range. In general, variation in measured  $e$  when fitting with the techniques introduced in this chapter is smaller than when using the current SpEC implementation. Note the logarithmic scale on the vertical axis.

## References

- [1] Kashif Alvi. “An Approximate binary black hole metric”. In: *Phys. Rev. D* 61 (2000), p. 124013. DOI: [10.1103/PhysRevD.61.124013](https://doi.org/10.1103/PhysRevD.61.124013). arXiv: [gr-qc/9912113](https://arxiv.org/abs/gr-qc/9912113).
- [2] Luc Blanchet. “Gravitational radiation from post-Newtonian sources and inspiralling compact binaries”. In: *Living Rev. Rel.* 9 (2006), p. 4.
- [3] Matteo Boschini et al. “Extending black-hole remnant surrogate models to extreme mass ratios”. In: *Phys. Rev. D* 108.8 (2023), p. 084015. DOI: [10.1103/PhysRevD.108.084015](https://doi.org/10.1103/PhysRevD.108.084015). arXiv: [2307.03435](https://arxiv.org/abs/2307.03435) [[gr-qc](#)].
- [4] Matteo Boschini et al. “Orbital eccentricity in general relativity from catastrophe theory”. In: *Phys. Rev. D* 111.2 (2025), p. 024008. DOI: [10.1103/PhysRevD.111.024008](https://doi.org/10.1103/PhysRevD.111.024008). arXiv: [2411.00098](https://arxiv.org/abs/2411.00098) [[gr-qc](#)].
- [5] Michael Boyle. “Angular velocity of gravitational radiation from precessing binaries and the corotating frame”. In: *Phys. Rev. D* 87.10 (2013), p. 104006. DOI: [10.1103/PhysRevD.87.104006](https://doi.org/10.1103/PhysRevD.87.104006). arXiv: [1302.2919](https://arxiv.org/abs/1302.2919) [[gr-qc](#)].
- [6] Michael Boyle et al. “The SXS Collaboration catalog of binary black hole simulations”. In: *Class. Quant. Grav.* 36.19 (2019), p. 195006. DOI: [10.1088/1361-6382/ab34e2](https://doi.org/10.1088/1361-6382/ab34e2). arXiv: [1904.04831](https://arxiv.org/abs/1904.04831) [[gr-qc](#)].
- [7] Alessandra Buonanno et al. “Reducing orbital eccentricity of precessing black-hole binaries”. In: *Phys. Rev. D* 83 (10 2011), p. 104034. DOI: [10.1103/PhysRevD.83.104034](https://doi.org/10.1103/PhysRevD.83.104034). URL: <https://link.aps.org/doi/10.1103/PhysRevD.83.104034>.
- [8] Alessandro Ciarfella et al. *Quasicircular Orbital Parameters for Numerical Relativity Revisited*. June 2024. arXiv: [2406.11564](https://arxiv.org/abs/2406.11564) [[gr-qc](#)].
- [9] Gregory B. Cook. “Initial data for numerical relativity”. In: *Living Rev. Rel.* 3 (2000), p. 5. DOI: [10.12942/lrr-2000-5](https://doi.org/10.12942/lrr-2000-5). arXiv: [gr-qc/0007085](https://arxiv.org/abs/gr-qc/0007085).
- [10] Roberto Cotesta et al. “Enriching the Symphony of Gravitational Waves from Binary Black Holes by Tuning Higher Harmonics”. In: *Phys. Rev. D* 98.8 (2018), p. 084028. DOI: [10.1103/PhysRevD.98.084028](https://doi.org/10.1103/PhysRevD.98.084028). arXiv: [1803.10701](https://arxiv.org/abs/1803.10701) [[gr-qc](#)].
- [11] Nils Deppe et al. *SpECTRE v2024.08.03*. Version 2024.08.03. Aug. 2024. DOI: [10.5281/zenodo.13207712](https://doi.org/10.5281/zenodo.13207712). URL: <https://spectre-code.org>.
- [12] Giacomo Fragione and Bence Kocsis. “Black hole mergers from an evolving population of globular clusters”. In: *Phys. Rev. Lett.* 121.16 (2018), p. 161103. DOI: [10.1103/PhysRevLett.121.161103](https://doi.org/10.1103/PhysRevLett.121.161103). arXiv: [1806.02351](https://arxiv.org/abs/1806.02351) [[astro-ph.GA](#)].

- [13] Rossella Gamba et al. “GW190521 as a dynamical capture of two nonspinning black holes”. In: *Nature Astron.* 7.1 (2023), pp. 11–17. DOI: [10.1038/s41550-022-01813-w](https://doi.org/10.1038/s41550-022-01813-w). arXiv: [2106.05575](https://arxiv.org/abs/2106.05575) [gr-qc].
- [14] V. Gayathri et al. “Eccentricity estimate for black hole mergers with numerical relativity simulations”. In: *Nature Astron.* 6.3 (2022), pp. 344–349. DOI: [10.1038/s41550-021-01568-w](https://doi.org/10.1038/s41550-021-01568-w). arXiv: [2009.05461](https://arxiv.org/abs/2009.05461) [astro-ph.HE].
- [15] G. H. Golub and V. Pereyra. “The Differentiation of Pseudo-Inverses and Nonlinear Least Squares Problems Whose Variables Separate”. In: *Tech. Rep. STAN-CS-72-261*. Computer Science Department, Stanford University, Stanford, CA, 1972.
- [16] G. H. Golub and V. Pereyra. “The Differentiation of Pseudo-Inverses and Nonlinear Least Squares Problems Whose Variables Separate”. In: *SIAM Journal on Numerical Analysis* 10.2 (1973), pp. 413–432. DOI: [10.1137/0710036](https://doi.org/10.1137/0710036). eprint: <https://doi.org/10.1137/0710036>. URL: <https://doi.org/10.1137/0710036>.
- [17] Nihar Gupte et al. *Evidence for eccentricity in the population of binary black holes observed by LIGO-Virgo-KAGRA*. Apr. 2024. arXiv: [2404.14286](https://arxiv.org/abs/2404.14286) [gr-qc].
- [18] Fredric J. Harris. “On the Use of Windows for Harmonic Analysis with the Discrete Fourier Transform”. In: *IEEE Proceedings* 66 (Jan. 1978), pp. 51–83.
- [19] James Healy et al. “Post-Newtonian Quasicircular Initial Orbits for Numerical Relativity”. In: *Class. Quant. Grav.* 34.14 (2017). [Erratum: *Class. Quant. Grav.* 40, 249502 (2023)], p. 145011. DOI: [10.1088/1361-6382/aa7929](https://doi.org/10.1088/1361-6382/aa7929). arXiv: [1702.00872](https://arxiv.org/abs/1702.00872) [gr-qc].
- [20] H. L. Iglesias et al. *Eccentricity estimation for five binary black hole mergers with higher-order gravitational wave modes*. Aug. 2022. arXiv: [2208.01766](https://arxiv.org/abs/2208.01766) [gr-qc].
- [21] Tousif Islam et al. “Eccentric binary black hole surrogate models for the gravitational waveform and remnant properties: comparable mass, nonspinning case”. In: *Phys. Rev. D* 103.6 (2021), p. 064022. DOI: [10.1103/PhysRevD.103.064022](https://doi.org/10.1103/PhysRevD.103.064022). arXiv: [2101.11798](https://arxiv.org/abs/2101.11798) [gr-qc].
- [22] Tousif Islam et al. “Surrogate model for gravitational wave signals from nonspinning, comparable-to large-mass-ratio black hole binaries built on black hole perturbation theory waveforms calibrated to numerical relativity”. In: *Phys. Rev. D* 106.10 (2022), p. 104025. DOI: [10.1103/PhysRevD.106.104025](https://doi.org/10.1103/PhysRevD.106.104025). arXiv: [2204.01972](https://arxiv.org/abs/2204.01972) [gr-qc].
- [23] Nathan K. Johnson-McDaniel et al. “Conformally curved binary black hole initial data including tidal deformations and outgoing radiation”. In: *Phys. Rev. D* 80 (2009), p. 124039. DOI: [10.1103/PhysRevD.80.124039](https://doi.org/10.1103/PhysRevD.80.124039). arXiv: [0907.0891](https://arxiv.org/abs/0907.0891) [gr-qc].

- [24] Bernard J. Kelly et al. “Post-Newtonian Initial Data with Waves: Progress in Evolution”. In: *Class. Quant. Grav.* 27 (2010), p. 114005. DOI: [10.1088/0264-9381/27/11/114005](https://doi.org/10.1088/0264-9381/27/11/114005). arXiv: [0912.5311](https://arxiv.org/abs/0912.5311) [gr-qc].
- [25] Taylor Knapp et al. “Parameter control for eccentric, precessing binary black hole simulations with SpEC”. In: *Phys. Rev. D* 111.2 (2025), p. 024003. DOI: [10.1103/PhysRevD.111.024003](https://doi.org/10.1103/PhysRevD.111.024003). arXiv: [2410.02997](https://arxiv.org/abs/2410.02997) [gr-qc].
- [26] Lionel London et al. “First higher-multipole model of gravitational waves from spinning and coalescing black-hole binaries”. In: *Phys. Rev. Lett.* 120.16 (2018), p. 161102. DOI: [10.1103/PhysRevLett.120.161102](https://doi.org/10.1103/PhysRevLett.120.161102). arXiv: [1708.00404](https://arxiv.org/abs/1708.00404) [gr-qc].
- [27] Geoffrey Lovelace. “Reducing spurious gravitational radiation in binary-black-hole simulations by using conformally curved initial data”. In: *Class. Quant. Grav.* 26 (2009), p. 114002. DOI: [10.1088/0264-9381/26/11/114002](https://doi.org/10.1088/0264-9381/26/11/114002). arXiv: [0812.3132](https://arxiv.org/abs/0812.3132) [gr-qc].
- [28] Ajit Kumar Mehta et al. “Accurate inspiral-merger-ringdown gravitational waveforms for nonspinning black-hole binaries including the effect of subdominant modes”. In: *Phys. Rev. D* 96.12 (2017), p. 124010. DOI: [10.1103/PhysRevD.96.124010](https://doi.org/10.1103/PhysRevD.96.124010). arXiv: [1708.03501](https://arxiv.org/abs/1708.03501) [gr-qc].
- [29] D. P. O’Leary and B. W. Rust. “Variable projection for nonlinear least squares problems”. In: *Comput. Optim. Appl.* 54 (2013), pp. 579–593. DOI: [10.1007/s10589-012-9492-9](https://doi.org/10.1007/s10589-012-9492-9).
- [30] Dianne P. O’Leary and Bert W. Rust. “Variable projection for nonlinear least squares problems”. In: *Comput. Optim. Appl.* 54.3 (2013), pp. 579–593. ISSN: 0926-6003. DOI: [10.1007/s10589-012-9492-9](https://doi.org/10.1007/s10589-012-9492-9). URL: <https://doi.org/10.1007/s10589-012-9492-9>.
- [31] Ryan M. O’Leary et al. “Binary mergers and growth of black holes in dense star clusters”. In: *Astrophys. J.* 637 (2006), pp. 937–951. DOI: [10.1086/498446](https://doi.org/10.1086/498446). arXiv: [astro-ph/0508224](https://arxiv.org/abs/astro-ph/0508224).
- [32] Eamonn O’Shea and Prayush Kumar. “Correlations in gravitational-wave reconstructions from eccentric binaries: A case study with GW151226 and GW170608”. In: *Phys. Rev. D* 108.10 (2023), p. 104018. DOI: [10.1103/PhysRevD.108.104018](https://doi.org/10.1103/PhysRevD.108.104018). arXiv: [2107.07981](https://arxiv.org/abs/2107.07981) [astro-ph.HE].
- [33] Serguei Ossokine et al. “Comparing Post-Newtonian and Numerical-Relativity Precession Dynamics”. In: *Phys. Rev. D* 92.10 (2015), p. 104028. DOI: [10.1103/PhysRevD.92.104028](https://doi.org/10.1103/PhysRevD.92.104028). arXiv: [1502.01747](https://arxiv.org/abs/1502.01747) [gr-qc].
- [34] P. C. Peters. “Gravitational Radiation and the Motion of Two Point Masses”. In: *Phys. Rev.* 136 (4B 1964), B1224–B1232. DOI: [10.1103/PhysRev.136.B1224](https://doi.org/10.1103/PhysRev.136.B1224). URL: <https://link.aps.org/doi/10.1103/PhysRev.136.B1224>.

- [35] P. C. Peters and J. Mathews. “Gravitational Radiation from Point Masses in a Keplerian Orbit”. In: *Phys. Rev.* 131 (1 1963), pp. 435–440. DOI: [10.1103/PhysRev.131.435](https://doi.org/10.1103/PhysRev.131.435). URL: <https://link.aps.org/doi/10.1103/PhysRev.131.435>.
- [36] Harald P. Pfeiffer, Gregory B. Cook, and Saul A. Teukolsky. “Comparing initial data sets for binary black holes”. In: *Phys. Rev. D* 66 (2002), p. 024047. DOI: [10.1103/PhysRevD.66.024047](https://doi.org/10.1103/PhysRevD.66.024047). arXiv: [gr-qc/0203085](https://arxiv.org/abs/gr-qc/0203085).
- [37] Harald P. Pfeiffer et al. “A multidomain spectral method for solving elliptic equations”. In: *Computer Physics Communications* 152.3 (May 2003), pp. 253–273. DOI: [10.1016/S0010-4655\(02\)00847-0](https://doi.org/10.1016/S0010-4655(02)00847-0). arXiv: [gr-qc/0202096](https://arxiv.org/abs/gr-qc/0202096) [gr-qc].
- [38] Harald P. Pfeiffer et al. “Reducing orbital eccentricity in binary black hole simulations”. In: *Class. Quant. Grav.* 24 (2007). Ed. by Manuela Campanelli and Luciano Rezzolla, S59–S82. DOI: [10.1088/0264-9381/24/12/S06](https://doi.org/10.1088/0264-9381/24/12/S06). arXiv: [gr-qc/0702106](https://arxiv.org/abs/gr-qc/0702106).
- [39] Michael Pürrer, Sascha Husa, and Mark Hannam. “An efficient iterative method to reduce eccentricity in numerical-relativity simulations of compact binary inspiral”. In: *Phys. Rev. D* 85 (12 2012), p. 124051. DOI: [10.1103/PhysRevD.85.124051](https://doi.org/10.1103/PhysRevD.85.124051). URL: <https://link.aps.org/doi/10.1103/PhysRevD.85.124051>.
- [40] Antoni Ramos-Buades, Alessandra Buonanno, and Jonathan Gair. “Bayesian inference of binary black holes with inspiral-merger-ringdown waveforms using two eccentric parameters”. In: *Phys. Rev. D* 108.12 (2023), p. 124063. DOI: [10.1103/PhysRevD.108.124063](https://doi.org/10.1103/PhysRevD.108.124063). arXiv: [2309.15528](https://arxiv.org/abs/2309.15528) [gr-qc].
- [41] Antoni Ramos-Buades, Sascha Husa, and Geraint Pratten. “Simple procedures to reduce eccentricity of binary black hole simulations”. In: *Phys. Rev. D* 99.2 (2019), p. 023003. DOI: [10.1103/PhysRevD.99.023003](https://doi.org/10.1103/PhysRevD.99.023003). arXiv: [1810.00036](https://arxiv.org/abs/1810.00036) [gr-qc].
- [42] George Reifenberger and Wolfgang Tichy. “Alternatives to standard puncture initial data for binary black hole evolution”. In: *Phys. Rev. D* 86 (2012), p. 064003. DOI: [10.1103/PhysRevD.86.064003](https://doi.org/10.1103/PhysRevD.86.064003). arXiv: [1205.5502](https://arxiv.org/abs/1205.5502) [gr-qc].
- [43] Isobel M. Romero-Shaw, Paul D. Lasky, and Eric Thrane. “Signs of Eccentricity in Two Gravitational-wave Signals May Indicate a Subpopulation of Dynamically Assembled Binary Black Holes”. In: *Astrophys. J. Lett.* 921.2 (2021), p. L31. DOI: [10.3847/2041-8213/ac3138](https://doi.org/10.3847/2041-8213/ac3138). arXiv: [2108.01284](https://arxiv.org/abs/2108.01284) [astro-ph.HE].
- [44] Isobel M. Romero-Shaw et al. “GW190521: orbital eccentricity and signatures of dynamical formation in a binary black hole merger signal”. In: *Astrophys. J. Lett.* 903.1 (2020), p. L5. DOI: [10.3847/2041-8213/abbe26](https://doi.org/10.3847/2041-8213/abbe26). arXiv: [2009.04771](https://arxiv.org/abs/2009.04771) [astro-ph.HE].

- [45] Johan Samsing. “Eccentric Black Hole Mergers Forming in Globular Clusters”. In: *Phys. Rev. D* 97.10 (2018), p. 103014. doi: [10.1103/PhysRevD.97.103014](https://doi.org/10.1103/PhysRevD.97.103014). arXiv: [1711.07452](https://arxiv.org/abs/1711.07452) [astro-ph.HE].
- [46] Md Arif Shaikh et al. “Defining eccentricity for gravitational wave astronomy”. In: *Phys. Rev. D* 108.10 (2023), p. 104007. doi: [10.1103/PhysRevD.108.104007](https://doi.org/10.1103/PhysRevD.108.104007). arXiv: [2302.11257](https://arxiv.org/abs/2302.11257) [gr-qc].
- [47] SXS Collaboration. *The SXS Collaboration catalog of gravitational waveforms*. <http://data.black-holes.org/waveforms>.
- [48] *The Spectral Einstein Code*. <http://www.black-holes.org/SpEC.html>.
- [49] Wolfgang Tichy. “The initial value problem as it relates to numerical relativity”. In: *Rept. Prog. Phys.* 80.2 (2017), p. 026901. doi: [10.1088/1361-6633/80/2/026901](https://doi.org/10.1088/1361-6633/80/2/026901). arXiv: [1610.03805](https://arxiv.org/abs/1610.03805) [gr-qc].
- [50] Vijay Varma, Mark A. Scheel, and Harald P. Pfeiffer. “Comparison of binary black hole initial data sets”. In: *Phys. Rev. D* 98.10 (2018), p. 104011. doi: [10.1103/PhysRevD.98.104011](https://doi.org/10.1103/PhysRevD.98.104011). arXiv: [1808.08228](https://arxiv.org/abs/1808.08228) [gr-qc].
- [51] Vijay Varma et al. “Surrogate models for precessing binary black hole simulations with unequal masses”. In: *Phys. Rev. Research*. 1 (2019), p. 033015. doi: [10.1103/PhysRevResearch.1.033015](https://doi.org/10.1103/PhysRevResearch.1.033015). arXiv: [1905.09300](https://arxiv.org/abs/1905.09300) [gr-qc].
- [52] *varpro*. <https://github.com/sxs-collaboration/varpro>.
- [53] Pauli Virtanen et al. “SciPy 1.0: Fundamental Algorithms for Scientific Computing in Python”. In: *Nature Methods* 17 (2020), pp. 261–272. doi: [10.1038/s41592-019-0686-2](https://doi.org/10.1038/s41592-019-0686-2).
- [54] Henry Wilbraham. “On a certain Periodic Function”. In: *The Cambridge and Dublin Math. J.* 3 (1848), pp. 198–201.
- [55] Shichao Wu, Zhoujian Cao, and Zong-Hong Zhu. “Measuring the eccentricity of binary black holes in GWTC-1 by using the inspiral-only waveform”. In: *Mon. Not. Roy. Astron. Soc.* 495.1 (2020), pp. 466–478. doi: [10.1093/mnras/staa1176](https://doi.org/10.1093/mnras/staa1176). arXiv: [2002.05528](https://arxiv.org/abs/2002.05528) [astro-ph.IM].
- [56] Jooheon Yoo et al. “Numerical relativity surrogate model with memory effects and post-Newtonian hybridization”. In: *Phys. Rev. D* 108.6 (2023), p. 064027. doi: [10.1103/PhysRevD.108.064027](https://doi.org/10.1103/PhysRevD.108.064027). arXiv: [2306.03148](https://arxiv.org/abs/2306.03148) [gr-qc].
- [57] Jooheon Yoo et al. “Targeted large mass ratio numerical relativity surrogate waveform model for GW190814”. In: *Phys. Rev. D* 106.4 (2022), p. 044001. doi: [10.1103/PhysRevD.106.044001](https://doi.org/10.1103/PhysRevD.106.044001). arXiv: [2203.10109](https://arxiv.org/abs/2203.10109) [gr-qc].

- [58] Nicolas Yunes and Wolfgang Tichy. “Improved initial data for black hole binaries by asymptotic matching of post-Newtonian and perturbed black hole solutions”. In: *Phys. Rev. D* 74 (2006), p. 064013. DOI: [10.1103/PhysRevD.74.064013](https://doi.org/10.1103/PhysRevD.74.064013). arXiv: [gr-qc/0601046](https://arxiv.org/abs/gr-qc/0601046).
- [59] Michael Zevin et al. “Implications of Eccentric Observations on Binary Black Hole Formation Channels”. In: *Astrophys. J. Lett.* 921.2 (2021), p. L43. DOI: [10.3847/2041-8213/ac32dc](https://doi.org/10.3847/2041-8213/ac32dc). arXiv: [2106.09042](https://arxiv.org/abs/2106.09042) [[astro-ph.HE](https://arxiv.org/archive/hep)].

*Chapter 3***ERROR QUANTIFICATION AND COMPARISON OF BINARY  
NEUTRON STAR GRAVITATIONAL WAVEFORMS FROM  
NUMERICAL RELATIVITY CODES**

- [1] Sarah Habib et al. “Error quantification and comparison of binary neutron star gravitational waveforms from numerical relativity codes”. In preparation.

Future gravitational wave detections of merging binary neutron star systems have the possibility to tightly constrain the equation of state of dense nuclear matter. In order to extract such constraints, gravitational waveform models need to be calibrated to accurate numerical relativity simulations of the late inspiral and merger. In this work, we take an essential step toward classifying the error and potential systematics in current generation numerical relativity simulations of merging binary neutron stars. To this end, we perform a direct comparison of three codes (FILL, SpEC, SpECTRE), which differ in almost all aspects, including the numerical methods and discretizations used and equations solved. We find that despite these different approaches, the codes are—within current numerical resolution bounds—fully consistent, and broadly comparable in cost for a given accuracy level. Our results indicate that the error in the waveforms is primarily dominated by the hydrodynamic evolution. We also discuss current limitations and cost estimates for numerical relativity simulations to reach the accuracies required in the era of next-generation gravitational detectors.

### 3.1 Introduction

Binary neutron star (BNS) mergers are exciting gravitational wave sources. With two events detected [2, 3], and many more expected before the end of this decade and beyond [95, 5], there are multiple scientific opportunities to be leveraged. Apart from multi-messenger astronomy of afterglows and gamma-ray bursts associated with BNS (see, e.g. Ref. [33] for a recent review), the gravitational wave (GW) signal itself promises to provide a wealth of information on the dense matter equation of state (EOS) (e.g., Refs. [27, 104]). This is because neutron stars, unlike black holes [78, 31], can be tidally deformed, altering the gravitational waveform in the final orbits approaching merger [57, 107]. Extracting this deformation for the first GW event of a merging BNS, GW170817, has already led to strong constraints on the EOS [10, 1, 90, 103, 36], with future detectors promising to deliver extremely tight constraints, e.g., on the radii of neutron stars [28, 56] (see e.g., Refs. [105, 53] for caveats stemming from phase transitions, chemical equilibration effects [112], and mode resonances [98]). One of the limiting factors in interpreting GW signals to sufficient accuracy to extract this information are well-calibrated waveform models (see, e.g., Ref. [44] for current models). Exacerbating this need, currently available models are not accurate enough for next-generation detectors [63]. Since tidal deformability imprints on the waveform cannot be fully computed from post-

Newtonian theory, which breaks down near merger, they are commonly fitted from numerical relativity (NR) simulations [42, 41, 44]. However, NR simulations of BNS are only available in a limited number of public catalogs [43, 64, 75, 76], which are not systematically sampled, as most of the simulations are targeting primarily the post-merger phase, which has different physics and accuracy requirements [30, 122, 34]. It is therefore important to ask what would be required to build a systematic catalog.

While NR simulations of binary black hole (BBH) mergers have been carried out at extreme precisions already [25], BNS merger simulations so far lag substantially behind, in part because of limited convergence and substantial errors stemming from the hydrodynamical modeling of the stellar material [101, 16, 89, 79]. Different groups have implemented a number of strategies for computing GW waves from merging BNS, especially on the hydrodynamics side, using high-order numerical methods [101, 16, 89], including entropy based limiting [47, 46], and spectral [48] or finite-element methods [38, 6]. Because of their algorithmic or implementation differences, these codes have different intrinsic errors and computational costs. While most codes solve a version of the BSSN [116, 15] or Z4 set of equations [20, 17, 71, 9], others use a generalized harmonic set of variables [99, 81]. Initial conditions for the simulations need to be computed numerically, e.g., by solving the extended conformally thin sandwich (XCTS) equations [96]. This is commonly done using spectral [66, 120, 119, 94] or finite-difference [50, 121] discretizations. Given all these various parts it seems important to ask whether using any such combination of different methods and codes lead to comparable errors or systematic differences when used under production settings. However, only a limited number of direct code comparisons have been carried out [52, 68, 93]. In light of the above question of building a waveform catalog it seems, however, imperative to have a well-defined error budget, as has been established in the case of BBH simulations [7].

In this work, we present a direct code comparison between three different NR codes (FIL [89, 54], SpEC [115, 114, 117, 118], and SpECTRE [38]) for BNS merger simulations. These use different numerical algorithms, formulations of the Einstein equations, and independent initial-data codes, such as the FUKA [94, 67] and SpELLS [119] libraries. As such, the comparison of codes is as different as currently possible with codes in the community, and allows for a faithful assessment of intrinsic consistency and error budgets of current generation numerical waveforms. We outline the currently (limited) accuracy of typical production-level simulations

and discuss potential requirements for future simulation work.s

This chapter is structured as follows. In Sec. 3.2 we present the setup for the comparison. The main results are shown in Sec. 3.3, before concluding in Sec. 3.4. This work uses a unit convention of  $G = c = 1$ .

## 3.2 Methods

For this comparison we adopt an equal mass BNS system with negligible neutron star spin and a total mass of  $M = 1.350M_{\odot}$  at infinite separation, and a baryon mass of  $M_b = 1.4958M_{\odot}$  per NS. We adopt an initial separation of 47.67 km. The initial data are prescribed using the extended conformal thin-sandwich (XCTS) formulation [96]. For more details see, e.g., Refs. [120, 119]. We further adopt eccentricity-reducing initial parameters following the parametrization of Ref. [26]. Specifically, we use

$$\begin{aligned}\dot{a} &= -8.09518351 \times 10^{-5}, \\ M_{\odot}^2 \Omega &= 0.008017218957,\end{aligned}$$

where  $\dot{a}d/2$  is the initial radial velocity of the stars,  $d$  the binary separation, and  $\Omega$  their initial angular velocity.

The choice of equation of state (EOS) dictates tidal effects and contributes to observable features in the GW signal, particularly during and after late inspiral. We use the SLy [45] spectral EOS implemented in Ref. [61]. At the time of writing, the SLyΓ2 model is within current EOS constraints from BNS observations [1, 4]. A spectral EOS is represented as a set of basis functions with coefficients [80]. In the EOS representation we use [61], the pressure  $P$  is related to the rest-mass density  $\rho$ , via

$$P(x, T) = P_0 \exp\left(\Gamma_0 x + \Theta(x) \left[\gamma_2 \frac{x^3}{3} + \gamma_3 \frac{x^4}{4}\right]\right) + \rho T, \quad (3.1)$$

where  $T$  is the temperature,  $x = \log(\rho/\rho_0)$ ,  $P_0 = 3.3625e - 7$ ,  $\gamma_2 = 0.4029$ ,  $\gamma_3 = -0.1008$ ,  $\rho_0 = 1.0118e - 4$ ,  $\Gamma_0 = 2$ , and  $\Theta(x)$  is the Heaviside function. This representation is chosen to minimize loss of convergence due to non-smoothness in the equation of state [61, 106].

### 3.2.1 Evolution codes

We use the standard 3 + 1 decomposition in numerical relativity, in which the spacetime metric  $g_{\mu\nu}$  takes the form

$$ds^2 = -\alpha^2 dt^2 + \gamma_{ij} (dx^i + \beta^i dt) (dx^j + \beta^j dt), \quad (3.2)$$

where  $\alpha$  is the lapse,  $\beta^i$  is the shift, and  $\gamma_{ij}$  is the spatial metric.

All tested codes solve the general relativistic (magneto-)hydrodynamics (GR(M)HD) system of equations in flux-balanced conservation form [49]

$$\partial_t \mathbf{U} + \partial_i \mathbf{F}^i(\mathbf{U}) = \mathbf{S}(\mathbf{U}). \quad (3.3)$$

Here  $\mathbf{U}$  is the state vector of conserved variables to be evolved,  $\mathbf{F}^i(\mathbf{U})$  are the fluxes, and  $\mathbf{S}(\mathbf{U})$  are source terms. More details on the discretizations and the codes are provided in the following sections below. All runs were performed on comparable hardware, i.e. AMD EPYC CPUs with  $\sim 2.5$  GHz clock speed.

#### 3.2.1.1 FIL

The Frankfurt/IllinoisGRMHD (FIL) code is based on the Einstein Toolkit infrastructure [82]. It implements the GRMHD equations in 3+1 form [49], which are solved using a fourth-order accurate version of the conservative finite-difference ECHO scheme [37]. Reconstruction to cell interfaces uses WENO-Z [21], with fluxes  $\mathcal{F}$  being computed using a HLLC Riemann solver [51]. We additionally limit the fluxes using an approximate second-order a priori positivity-preserving limiter based on the density [102]. The resulting limited fluxes are then corrected using a DER4 corrector [37] to achieve overall higher order. In detail, we compute fluxes at cell interfaces,  $i + 1/2$ ,

$$F_{i+1/2} = \frac{13}{12} \mathcal{F}_{i+1/2} - \frac{1}{24} (\mathcal{F}_{i+3/2} - \mathcal{F}_{i-1/2}). \quad (3.4)$$

Primitive inversion is carried out using the scheme of Ref. [73], with a fall-back for purely hydrodynamical flows [62]. We also use an entropy-based backup solver. Equation of state handling is provided using FIL's microphysics infrastructure, which offers two ways of handling the spectral EOS used here. First, the EOS routine has been implemented using direct numerical integration outlined in Ref. [61]. However, we have found it more convenient to simply tabulate the spectral EOS

using a uniformly sampled table with 1,000 grid points, which is then interpolated linearly in logarithmic quantities.

The Einstein equations are solved using the Z4c formalism [17, 71] in moving puncture gauge [8]. Specifically, we adopt

$$\partial_t \alpha - \beta^i \partial_i \alpha = -2\alpha K, \quad (3.5)$$

$$\partial_t \beta^k - \beta^i \partial_i \beta^k = \frac{3}{4} B^k, \quad (3.6)$$

$$\partial_t B^k - \beta^i \partial_i B^k = (\partial_t - \beta^i \partial_i) \tilde{\Gamma}^k - \eta B^k, \quad (3.7)$$

where  $K$  is the trace of extrinsic curvature,  $\tilde{\Gamma}^k$  and  $B^k$  are the variables for the Gamma-driver, and  $\eta M_\odot = 0.2$ . We adopt Z4c damping parameters of  $\kappa = 0.04$ . All damping parameters have a roll-off with inverse distance that sets in at a radius of  $R/M_\odot = 64$ .

The resulting set of equations is then solved using a strong-stability preserving third-order Runge-Kutta scheme [65]. FIL uses a domain of 7 uniform-resolution AMR grids centered on each NS, with a total domain extent of  $2,048 M_\odot$ . The initial data configuration is computed using the FUKA code [94]. FUKA uses the KADATH spectral solver library [67]. The equation of state is handled using the same log-linear table used for the evolution.

### 3.2.1.2 SpEC

SpEC evolves the gravitational and hydrodynamic systems on two separate spatial grids [48]. The Einstein equations are evolved on a pseudospectral grid; the hydrodynamics equations are evolved on a finite-difference grid. Evolution is done with a third-order Runge-Kutta time stepper. The time step on the pseudospectral grid is chosen adaptively to reach a target tolerance varying with the chosen grid resolution. The time step on the finite-difference grid is allowed to be larger: up to  $\Delta t = \Delta x/4$ , with  $\Delta x$  the minimum grid spacing. At the end of a time step on the finite-difference grid, the metric and its derivatives are interpolated onto the finite-difference grid by first refining the spectral data using spectral interpolation, then using third-order interpolation onto the finite-difference grid. The primitive fluid variables are interpolated onto the pseudospectral grid using monotonicity-preserving polynomial interpolation. Data at intermediate times is obtained using linear interpolation (higher-order interpolation is possible but has no practical impact on the accuracy of the simulations [77]). More details on the time stepping

methods can be found in Ref. [77], while grid-to-grid interpolation is described in Ref. [48].

The pseudospectral grid during inspiral is composed of a set of spherical shells centered on each NS, balls around the NS interior regions, distorted cubes connecting the spherical regions to the wave zone, and spherical shells centered on the center of mass of the binary in the wave zone. SpEC employs adaptive mesh refinement (AMR) for the pseudospectral grid, adjusting resolution based on the errors estimated from the coefficients of the spectral expansion for each evolved variable. The target truncation error is scaled as  $\Delta x_{FD}^5$ , with details in Ref. [60]. The finite-difference grid uses a constant resolution grid during inspiral, and fixed mesh refinement after merger. In both cases, the finest level of the computational domain is divided into blocks of  $\sim 6 \text{ km}^3$  that are only evolved if matter is present in the region of space that they cover. More specifically, if all grid cells in a block have densities below  $6 \times 10^9 \text{ g/cm}^3$ , it is removed from the computational domain. If matter with density above  $10^{10} \text{ g/cm}^3$  approaches within 3 grid cells of a removed block, that block is added and evolved once more. The threshold densities are decreased far away from the center of the binary, as described in Ref. [60]. As the SpEC grid is constructed so that the centers of the compact objects are fixed on the grid during inspiral, the effective grid resolution increases as the neutron stars spiral in. Whenever the grid spacing is reduced by 20%, we interpolate onto a new finite-difference grid with the original grid resolution. Once the BNS approaches merger and the NSs deform, spherical pseudospectral domains around each NS no longer characterize symmetry in the binary, so both grids are restructured. When the maximum density on the pseudospectral grid grows to 3% higher than its initial value, the grid switches to a ball centered at the coordinate center of mass of the binary system, surrounded by spherical shells covering the wave zone. After contact, the finite-difference grid is made of four nested cubes. The finest resolution grid covers a  $40 \text{ km}^3$  region around the center of mass of the system. Each coarser level of refinement is twice as large in each dimension.

To keep the center of mass of the neutron stars fixed on the grid during inspiral, SpEC uses a time-dependent map between grid coordinates and “inertial” coordinates. That map includes both a global rescaling of the coordinates and a rotation around the polar axis. The control system used to evolve the scaling factor and rotation angle is described in more detail in Ref. [70].

The spacetime metric is evolved using the first-order GH formulation [81], in which

the coordinates  $\mathbf{x}$  obey the wave equation

$$g_{\mu\nu}\nabla^\sigma\nabla_\sigma x^\nu = H_\mu(\mathbf{x}, g_{\mu\nu}), \quad (3.8)$$

where  $H_\mu(\mathbf{x}, g_{\mu\nu})$  is an arbitrary gauge source function, which in SpEC is set to the harmonic gauge  $H_\mu = 0$ . This gives a system of equations and several constraint equations for  $g_{\mu\nu}$ ,  $\Phi_{i\mu\nu} \equiv \partial_i g_{\mu\nu}$ , and  $\Pi_{\mu\nu} \equiv n^\gamma \partial_\gamma g_{\mu\nu}$ , where  $n^\gamma$  is the unit normal vector to the spatial slice. Constraints are not enforced during numerical evolution and need to be monitored. SpEC damps the constraints  $C_\mu = \Gamma_\mu + H_\mu$  and  $C_{i\mu\nu} = \Phi_{i\mu\nu} - \partial_i g_{\mu\nu}$ , where  $\Gamma_\mu = \Gamma_{\nu\mu}^\nu$  is the contracted Christoffel symbol and  $\Phi_{i\mu\nu}$  the first-order reduction variable in the GH system. The constraint damping parameters are chosen the same as in Ref. [60]. In addition to constraint damping, violations are controlled by constraint-preserving boundary conditions enforced at the outer boundary of the computational domain as extra terms in the evolved variables [81, 110].

The hydrodynamics evolution uses numerical fluxes at cell faces that are computed from the characteristic fluxes and characteristic variables reconstructed on cell faces using the fifth-order accurate MP5 reconstructor, using the methods introduced in Ref. [102]. A density floor of  $\rho_{\text{floor}} = 6 \times 10^4 \text{ g/cm}^3$  is imposed, below which densities are reset to  $\rho_{\text{floor}}$ . Below  $\rho_{\text{atm}} \approx 1 \times 10^6 \text{ g/cm}^3$ , we also apply atmosphere corrections limiting the velocity of the fluid in the corotating frame to  $< 0.0001c$  and the pressure to  $P(\rho, T) < 1.01P(\rho, 0)$ . We also require  $T \geq 0$ . Finally, corrections to the conservative variables are performed whenever the evolution reaches values of the conserved variables that are close to becoming unphysical (i.e. to no longer correspond to physical values of the primitive variables), as described in Ref. [60].

### 3.2.1.3 SpECTRE

SpECTRE uses a hybrid discontinuous Galerkin-finite difference method [39, 38] on a single grid to evolve both the Einstein equations and the hydrodynamic equations. SpECTRE also uses the first-order GH formulation (as described in Sec. 3.2.1.2) and a third-order Adams-Moulton predictor-corrector time stepper. The computational domain is divided into nonoverlapping elements, and each element is evolved using either a discontinuous Galerkin (DG) or finite-difference (FD) scheme. Points in DG elements use Legendre-Gauss-Lobatto quadrature, while FD elements use a cell-centered equidistantly-spaced Cartesian grid in the “reference” or “logical” coordinates.

Whether an element uses DG or FD is determined dynamically. After each time step or substep, the validity of the DG solution in each element is checked with a troubled-cell indicator (TCI) as described below. In DG elements where the DG solution is deemed inadmissible, the step is undone and recomputed using FD. In FD elements, if the TCI determines that the DG solution would be acceptable, the *next* time/sub step will use DG. The TCI algorithm is essentially the same as that used in Ref. [38]. The TCI algorithm checks that evolved conserved variables  $\tilde{D}$  and  $\tilde{\tau}$  are positive (in practice above a small but positive number), that the primitive variables can be recovered, and that the DG basis function expansion converges for  $\tilde{D}$  and  $\tilde{\tau}$ . Finally, if we are in atmosphere we always use DG (atmosphere is determined similarly as in the SpEC code). DG and FD representations of the same element use different sets of grid points. For a DG element with  $N$  grid points in a particular dimension, the corresponding FD element uses  $(2N - 1)$  grid points in that dimension. When an element switches from DG to FD, the conserved variables are interpolated to the FD grid. When switching from FD to DG, a constrained linear least squares system is used to construct the restriction<sup>1</sup> operator [38]. DG has superior accuracy and efficiency for smooth solutions, but exhibits undesirable oscillatory behavior (Gibbs phenomenon) at discontinuities. The DG-FD hybrid method combines the advantages of DG with the robustness of FD. In practice, elements near the NS surfaces are primarily FD.

The computational domain consists of a rectangular inner domain of Cartesian elements containing the two NSs, and several wedge-shaped subdomains in the surrounding wave zone. The outer boundary of the computational domain is at  $R_{\text{boundary}} = 605M_{\odot}$ . SpECTRE uses three different coordinate systems. The “logical” or “reference” coordinates are locally Cartesian coordinates defined in each element on the cube  $[-1, 1]^3$  and are the coordinates in which the basis functions (i.e. Legendre polynomials) are defined. These are then mapped using time-independent coordinate maps to the “grid” frame. The grid coordinates are still Cartesian, but the individual elements are deformed to better suit the geometry of the underlying physical system. The grid coordinates corotate with the binary. Finally, the grid coordinates are mapped to the “inertial” frame<sup>2</sup> using a time-dependent map that currently is only a rotation (a translation is necessary for unequal mass systems to track the center-of-mass). The rotation is controlled by a feedback control system

<sup>1</sup>In our previous papers we called this operation “reconstruction” but find the terminology confusing with the reconstruction performed in the FD algorithm.

<sup>2</sup>The coordinates are not actually the coordinates of an inertial observer.

similar to that used in Ref. [38] and in BBH simulations [84]. We smoothly disable the rotation over a time scale of  $10M_\odot$  when the center of mass separation between the two stars falls below  $5M_\odot$ .

SpECTRE uses the same constraint damping approach as SpEC for the GH system, with parameters that are exactly those described in Ref. [38] except that the Gaussians now comove with the stars. The same constraint-preserving boundary conditions are also applied. We use harmonic gauge  $H_a = 0$  for the entire evolution. The hydrodynamics evolution also uses the divergence-cleaning Valencia formulation of the GRMHD equations but with zero magnetic field [11, 59, 14]. Primitive recovery for non-magnetized flows is done using the scheme from [62]. The GRMHD equations are solved using a flux-difference-splitting scheme with second-order spatial derivatives. The HLLE Riemann solver is used alongside fifth-order positivity-preserving adaptive-order reconstruction [40], the same scheme used in Ref. [38]. Thus, even though the GH equations on the FD grid are solved at sixth order, the FD solver is currently formally second-order accurate because of the GRMHD solver.

### 3.2.2 Waveform extraction

For a given mode of the GW strain  $h_{lm}$ , the waveform amplitude  $A$  and phase  $\phi$  are defined from the strain as

$$r h_{lm} = A_{lm} e^{-i\phi_{lm}}. \quad (3.9)$$

Sign conventions are not consistent among all codes (see Ref. [22], Appendix C for a discussion). For the following results, we use the sign convention

$$h = h_+ - i h_\times. \quad (3.10)$$

For our analysis, we primarily focus on the  $l = 2, m = 2$  mode.

We consider two  $l = 2, m = 2$  waveforms to be equivalent if they differ by only by an overall phase shift (equivalent to a rotation in the  $x$ - $y$  plane) and/or an overall time offset. So when comparing two different waveforms, we first align them by explicitly time-shifting and phase-shifting one of them. This must be done carefully because differences between waveforms are very sensitive to alignment. A typical alignment method is to time-shift and phase-shift so that the two waveforms reach their maximum amplitude at the same time and phase. However, we find that this results in phase differences being dominated by errors during the merger and

Run name	Code	Grid spacing [ $M_{\odot}$ ]	Grid spacing [m]	Computational cost to merger [core-hours]
SpEC Lev1	SpEC	0.17667	261.5	16,855 (25,491)
SpEC Lev2	SpEC	0.14134	209.2	44,476 (93,118)
SpEC Lev3	SpEC	0.11307	167.3	109,759 (187,331)
FIL Lev0	FIL	0.22857	338.3	46,080
FIL Lev1	FIL	0.178	263.4	71,349
FIL Lev2	FIL	0.1379	204.1	245,760
SpECTRE Lev0	SpECTRE	0.1944	287.7	33,312
SpECTRE Lev1	SpECTRE	0.1591	235.5	41,952
SpECTRE Lev2	SpECTRE	0.1346	199.2	120,061
SpECTRE Lev3	SpECTRE	0.1167	172.7	200,725

Table 3.1: The computational cost and grid spacing of the different codes. For SpEC we give the computational cost to merger as the time. For FIL we give the computational cost to merger as the time the maximum amplitude in the gravitational waveform is computed at a distance of  $600 M_{\odot}$ . For SpECTRE we give the computational cost to merger as the time when the peak of the waveform reaches the  $r = 200 M_{\odot}$  CCE worldtube radius, approximately  $t = 4700 M_{\odot}$ . Since we are interested in the GW signal during the inspiral, we exclude the post-merger cost. In SpEC the post-merger is significantly more expensive than the inspiral because of the much larger finite-difference grid.

post-merger, and we are most interested in errors during inspiral. So instead, we align waveforms by choosing the optimal time and phase shift to minimize the difference in amplitude and phase of the  $l = 2, m = 2$  strain mode over a chosen time window during the inspiral; this is a two-dimensional root-finding problem. The time window chosen for alignment, typically around  $[700 M_\odot, 2000 M_\odot]$ , must start sufficiently late such that junk radiation or CCE junk is not included in the minimization.

Asymptotic GW quantities can be extracted upon completion of a numerical simulation. The three primary methods for achieving this are using Nakano extrapolation (NE), finite-radius extrapolation (FRE), and Cauchy-Characteristic evolution (CCE). In the following results we apply these different methods and assess their contribution to overall simulation error.

### 3.2.2.1 Nakano extrapolation

FIL extracts the Weyl scalar  $\Psi_4$  at coordinate spheres of finite radii  $r$ . We use the perturbative formula proposed as Eq. 3 in Ref. [83],

$$\lim_{r \rightarrow \infty} r \Psi_4^{lm} = \left(1 - \frac{2M}{\bar{r}}\right) \times \quad (3.11)$$

$$\left[ \bar{r} \Psi_4^{lm} - \frac{(l-1)(l+2)}{2\bar{r}} \int \bar{r} \Psi_4^{lm} dt \right] \quad (3.12)$$

for a given extraction radius  $\bar{r}$ . We use this formula to obtain  $\Psi_4$  at future null infinity for FIL.

The  $\Psi_4$  spherical harmonic waveform can then be integrated to obtain the modes of the gravitational wave (GW) strain  $h$ , which are given as

$$h_{lm} = - \int_{-\infty}^t \int_{-\infty}^{t'} \Psi_4^{lm} dt'' dt', \quad (3.13)$$

where the sign is appropriately chosen for each code. However, simply integrating  $\Psi_4$  in time tends to cause a spurious nonlinear drift in the strain [109]. The standard solution is to compute the strain using fixed frequency integration (FFI) [109], i.e., integration of  $\Psi_4$  in the frequency domain while fixing the contribution from frequencies below a chosen cutoff. The cutoff frequency is a free parameter that must be fine tuned and chosen with care to avoid damping physical frequencies or amplifying unphysical features. Where necessary we use a cutoff near the orbital

frequency, the lowest physical frequency present in the system, as suggested in Ref. [109]. All FIL waveforms presented are computed using the NE GW extraction method.

### 3.2.2.2 Finite radius extrapolation

SpEC uses FRE to extract GW data. Specifically, in SpEC,  $\Psi_4$  and  $h$  are computed on a series of concentric spherical shells approximately evenly spaced in  $1/r$  and centered on the binary. The waveforms are then extrapolated to future null infinity by fitting a series in powers of  $1/r$  to the data on the concentric shells [23]. Less care is taken in using the “best” tetrad when computing  $\Psi_4$  and  $h$  on the shells since the errors from tetrad differences will extrapolate away. We emphasize that in addition to extracting  $\Psi_4$  directly, SpEC *directly and independently* extracts the GW strain  $h$  using the Sarbach and Tiglio formulation [113] of the Regge-Wheeler and Zerilli equations [108, 123] with implementation details described in Refs. [111, 25, 24]. Unless otherwise stated, we use the extrapolated waveforms for SpEC in our analysis.

### 3.2.2.3 Cauchy-Characteristic Evolution

Cauchy-characteristic evolution (CCE) [19, 18, 69, 12, 91, 92] is a waveform extraction method where Einstein’s equations are solved out to future null infinity,  $\mathcal{I}^+$ . Metric data on a worldtube at some finite radius is written to disk during the Cauchy evolution, i.e., during the GH simulation in SpEC and SpECTRE. This data is then used as a boundary condition to the characteristic evolution that evolves the outgoing gravitational radiation to  $\mathcal{I}^+$ . CCE is able to capture physical effects like gravitational wave memory that are not present in extrapolated waveforms [88, 85]. Figure 3.1 shows a schematic representation of the simulation domains involved. By solving the Einstein equations to  $\mathcal{I}^+$ , CCE circumvents extrapolation errors inherent in FRE waveforms. Thus, CCE will generally produce more realistic waveforms than any extrapolation procedure. Despite these advantages, CCE is not completely parameter-free since initial data on the initial null slice needs to be chosen and different radii for the worldtube can be used. An additional complication that CCE presents is that the waveforms are output in an arbitrary Bondi-Metzner-Sachs (BMS) frame. This frame is not generally going to match the one that the

extrapolated waveforms are in. We choose to always map the waveforms to their own superrest frame [85].

We use several worldtube radii for CCE, and find that the resulting waveforms differ slightly. SpEC uses radii of  $\{129, 496, 863, 1230\} M_\odot$  while SpECTRE uses  $\{200, 250, 300, 350, 400, 450, 500\} M_\odot$ . All CCE waveforms are extracted using the SpECTRE CCE module [92]. For each code, we choose the extraction radius with the smallest  $\Psi_2$  constraint.

We use SpEC to study the difference between extrapolated and CCE waveforms for BNS simulations. Since SpECTRE does not output any finite radius or extrapolated waveforms, it is crucial to understand if systematic difference between the extrapolated and CCE waveforms are a dominant source of discrepancy between different codes. For SpECTRE waveforms, we use a CCE worldtube radius of  $200 M_\odot$ , which minimizes effects from the outer computational boundary at  $605 M_\odot$ . This worldtube radius is in the range typically used for BBH simulations as well.

### 3.3 Results

In this section, we perform several side-by-side comparisons of BNS simulations with the same initial parameters run by different codes. Table 3.1 describes the runs examined in this section. We analyze SpEC and FIL at three different finite-difference resolutions each, allowing for convergence tests. Each level increases the resolution by about 25%. We restrict our analysis to inspiral and merger in the following.

Note that at the time of writing, SpECTRE BNS simulation is not in a production state and some SpECTRE runs are in progress, so analysis and comparison of SpECTRE BNS waveforms in the following sections is limited.

#### 3.3.1 Waveform properties

Here we compare waveform features during the inspiral. Figure 3.2 shows the real part of the GW strain  $rh_{22}$  and the strain amplitude  $|rh_{22}|$  for the highest-resolution runs available from each code. Waveforms in Fig. 3.2 have been individually aligned to SpEC Lev3 by time and phase shifts as described in Sec. 3.2.2.

In general, all three codes show remarkable agreement by eye in frequency and phase evolution until merger. The fact that we start out with very good agreement

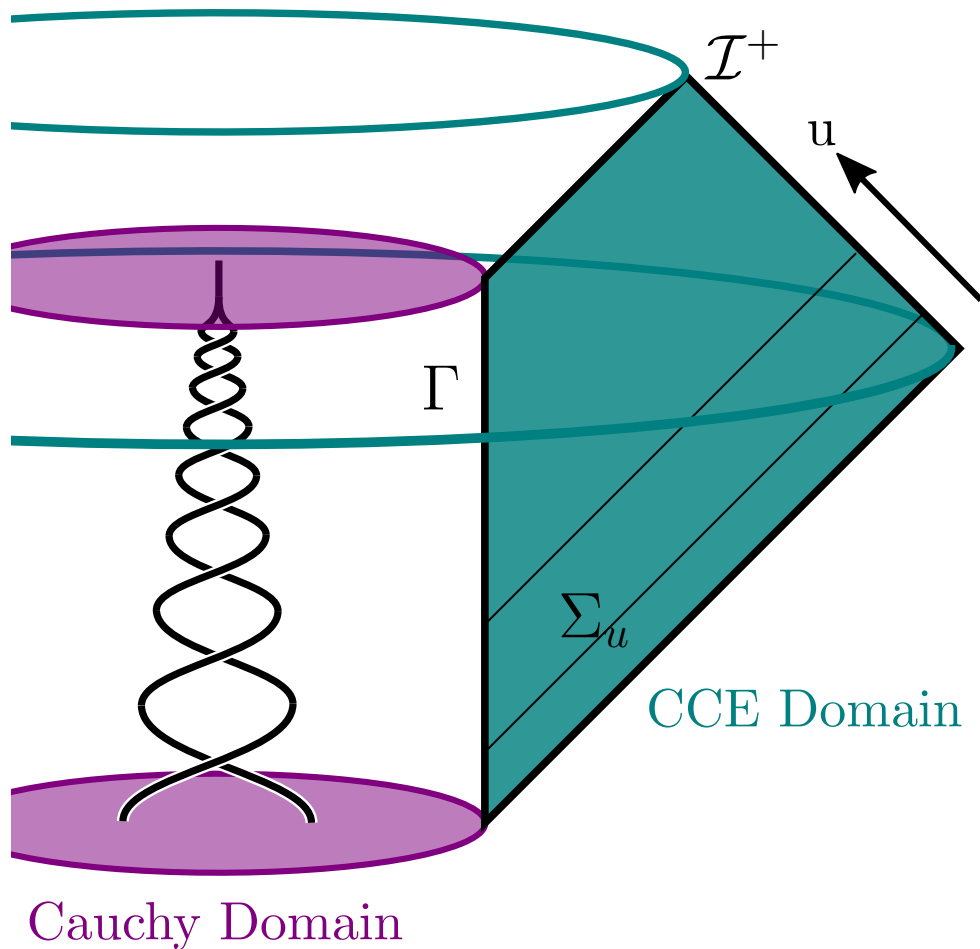


Figure 3.1: A schematic spacetime diagram showing the domains of CCE. The initial evolution of the Einstein equations through inspiral, merger, and ringdown is done in the Cauchy domain. The Cauchy evolution then supplies initial data on the worldtube  $\Gamma$  for the proceeding evolution in the characteristic domain. The characteristic evolution takes place on null hypersurfaces  $\Sigma_u$  that extend to null infinity  $\mathcal{I}^+$ , and from the characteristic system the outgoing gravitational radiation at  $\mathcal{I}^+$  can be recovered. Figure reproduced from Ref. [92] (Figure 1).

already implies that we should be able to meaningfully compare the different codes quantitatively. Since the initial configuration is constructed without gravitational wave content from previous orbits being present in the initial domain, *junk radiation*, spurious waveform content sourced from the relaxation of initial data in the beginning of evolution, and CCE junk (present in SpECTRE only) are present (see initial oscillations in the amplitude), but do not significantly impact the observed code agreement.

Figure 3.3 provides a zoom-in on the time of merger for all resolutions. Runs in this figure are unaligned and are instead matched in time to the retarded time at infinity,  $u$ , as best estimated for each code. Since numerical resolution strongly affects (spurious) dissipation of orbital energy, we expect a monotonic increase in the time of merger with increasing resolution. In all codes, higher resolution runs do reach merger at later times, by as much as  $\sim 60 M_{\odot}$ . Note that the coalescence time in both SpEC and FIL appears to converge asymptotically with increasing grid resolution. As such, the waveforms we use should have a sufficiently high fidelity for a code comparison, which we provide in quantitative terms in the following.

### 3.3.2 Error analysis

There are several possible sources of error in numerical-relativity waveforms. One source is roundoff error, originating from the finite precision of values represented by computer hardware. More important and usually dominant is truncation error, which comes from approximating continuous values as discrete. In numerical waveforms, truncation error includes contributions from discretization in space and time. Additional error sources come from extrapolation of waveform quantities to future null infinity. While CCE does not have extrapolation errors, it is still subject to truncation errors in the discretization of the Einstein equations on the characteristic domain, and systematic errors from choosing the worldtube radius and initial data on the initial null slice. Improving the accuracy of numerical waveforms requires understanding which of these error sources dominate.

In the following sections, we show several measures of error using the phase of the  $l = 2, m = 2$  mode of the strain. In Sec. 3.3.2.1 we perform self-convergence tests with SpEC and FIL to check the self-consistency of measured errors with expected convergence rates. In Sec. 3.3.2.2 we measure the impact of waveform extraction in overall phase error, and in Sec. 3.3.2.3 we extrapolate continuum solutions from SpEC and FIL waveforms to assess systematic agreement between the two

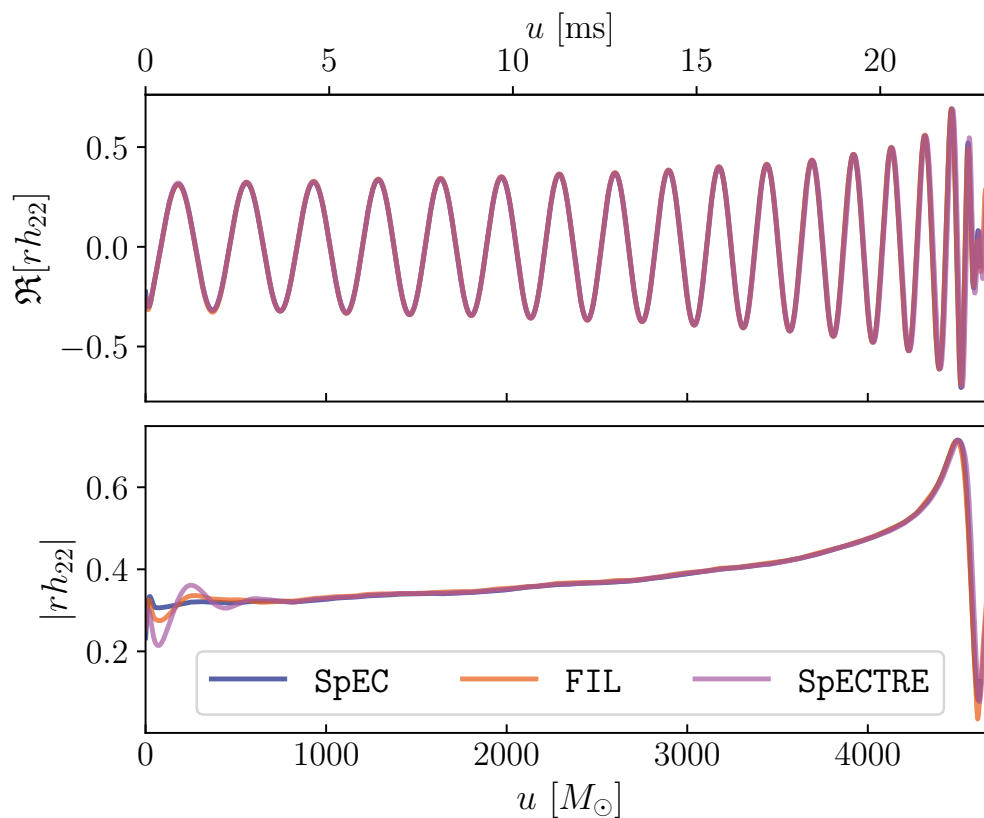


Figure 3.2: Real part of the  $l = 2, m = 2$  strain mode  $\Re(rh_{22})$  and amplitude of the  $l = 2, m = 2$  strain mode  $|rh_{22}|$  for the highest resolution runs available from each code (SpEC Lev3, FIL Lev2, and SpECTRE Lev2). Runs are aligned to SpEC Lev3 with a time and phase shift. All waveforms generally show close agreement during inspiral and reach merger at similar times, having similar cycle evolutions, peak amplitudes, and inspiral lengths.

codes. Lastly, in Sec. 3.3.3 we discuss what our findings imply for target accuracy requirements with respect to next-generation gravitational wave observatories.

### 3.3.2.1 Phase error convergence

Convergent behavior in phase is a particularly important benchmark for numerical waveforms since the phase encodes various information about the system, including tidal deformability [57]. In this section, we perform self-convergence tests using SpEC and FIL waveforms to determine whether phase error scales predictably with grid resolution within each code.

Suppose we have a numerical waveform evolved at three uniform spatial resolutions

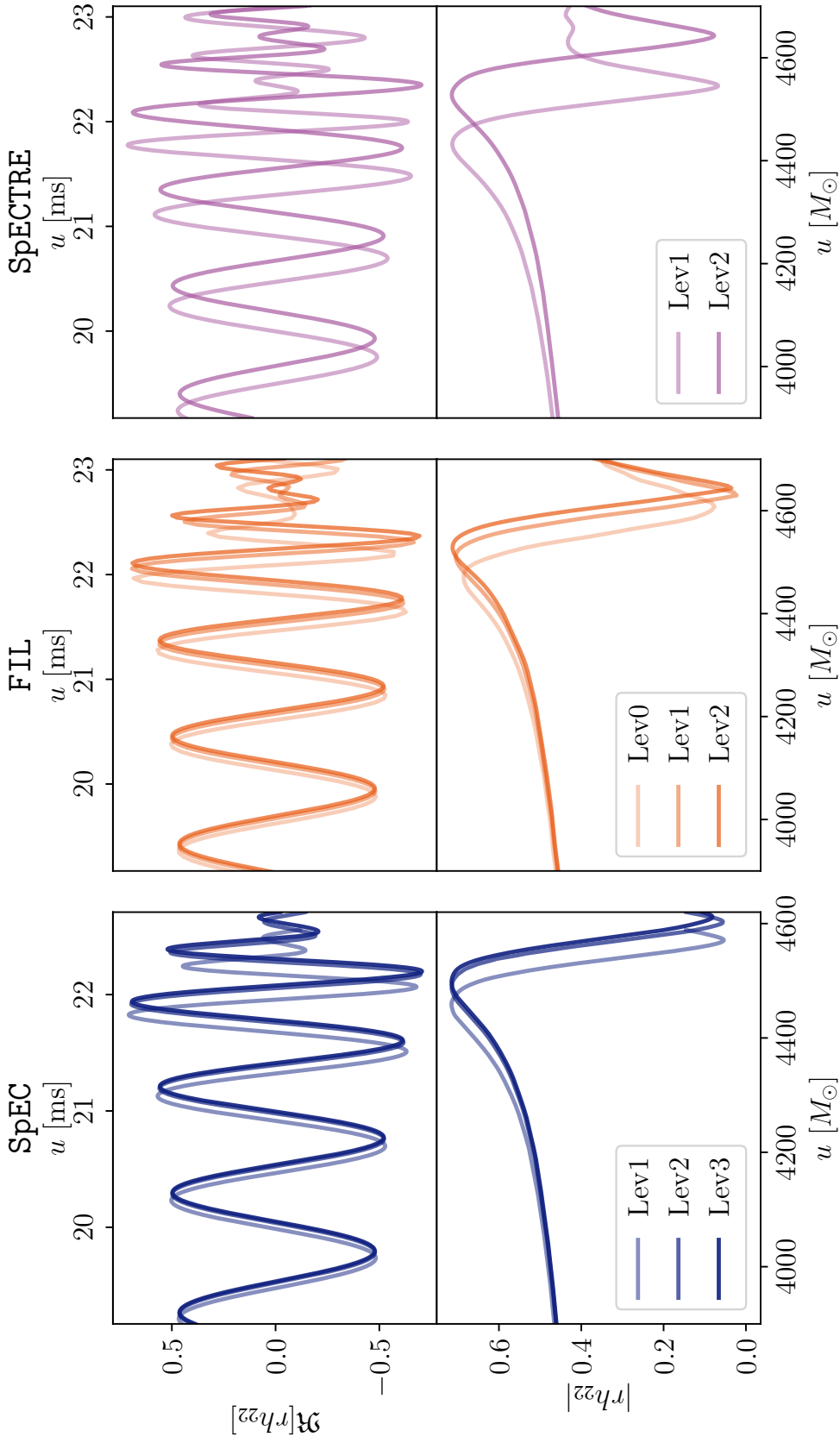


Figure 3.3: Real part of the  $l = 2, m = 2$  strain mode  $\Re(rh_{22})$  and amplitude of the  $l = 2, m = 2$  strain mode  $|rh_{22}|$  for all resolutions available from each code. Runs are not aligned, but are time-offset to match at estimated retarded time at infinity  $u$ ,  $r_e$  the extraction radius, and  $t$  the simulation time. Darker curves correspond to higher resolution runs. Inspiral is consistent between different resolutions, especially in SpEC and FIL. Runs with higher resolutions coalesce at later times because of decreased numerical dissipation.

$\Delta x_H < \Delta x_M < \Delta x_L$ . If truncation error from a FD scheme is the dominant error source, then for some exact solution  $f(x)$  we can write the expected solution obtained,  $\tilde{f}(\Delta x)$ , as

$$\tilde{f}(x) = f(\Delta x) + C\Delta x^p, \quad (3.14)$$

where  $C\Delta x^p$  is the contribution from truncation error. The variable  $p$  is the convergence order, which depends on and can be computed for a given choice of numerical FD scheme. Thus we expect that

$$\frac{\tilde{f}(\Delta x_M) - \tilde{f}(\Delta x_H)}{\tilde{f}(\Delta x_L) - \tilde{f}(\Delta x_M)} = \frac{\Delta x_M^p - \Delta x_H^p}{\Delta x_L^p - \Delta x_M^p}. \quad (3.15)$$

We calculate phase errors as the difference in time series at different resolutions, e.g.  $\tilde{f}(\Delta x_M) - \tilde{f}(\Delta x_H)$ .

A numerical result is said to be convergent if the equality in Eq. (3.15) holds for the expected  $p$ , meaning the error scales predictably with a limiting factor of the numerical accuracy, e.g. grid resolution. Convergence indicates that truncation error is the dominant error source and that implementations of the contributing numerical schemes are correct. Quantifying this error can be straightforward in numerical codes that have a fixed discretization, as in FIL, whereas in hybrid schemes, as in SpEC, in which the spectral and FD schemes have different orders, error cannot easily be analyzed in this way unless, e.g., the FD error dominates.

In Fig. 3.4, we show the phase difference  $\Delta\phi$  in radians over time between consecutive resolutions given three runs for SpEC and FIL. Each difference is calculated with the higher resolution time series interpolated onto the time grid of the lower resolution time series. Waveforms are matched by estimated retarded time without alignment, similar to those shown in Fig. 3.3. Colored lines show the phase differences between two waveforms of differing resolution, and dashed lines show the phase differences rescaled by the expected factor from Eq. (3.15) assuming some convergence order.

Errors in dashed lines are scaled from the higher resolution error and ideally should match the lower resolution error, and vice versa for dotted lines. SpEC errors are rescaled assuming third-order convergence ( $p = 3$ ). General convergence in SpEC is difficult to assess because of its coupled evolution grids and the competing effects of several numerical schemes. However, the rescaled errors do not conform to the measured errors, indicating that the error is not entirely dominated by the hydrodynamic sector, at least for the lowest resolution simulation available. It

is likely that the multiple schemes in SpEC interact differently at different grid resolutions (e.g. such that errors between SpEC Lev2 and SpEC Lev3 cancel). For different setups, SpEC has previously shown convergence during inspiral for BHNS waveforms [48].

FIL errors are rescaled assuming the expected third order ( $p = 3$ ). The rescaled errors show that FIL is consistent with third-order convergence during inspiral as demonstrated previously [89]. Although the FD scheme in FIL is formally fourth-order convergent, accuracy is limited either by the third-order time stepper or the third-order fallback reconstruction in the WENO-Z algorithm.

Overall, we confirm that phase errors systematically decrease with resolution for SpEC and FIL, and find that overall phase errors are small, on the order of  $O(10^{-2})$ .

### 3.3.2.2 Waveform extraction error

In this section, we assess the error contribution from waveform extraction. It has previously been established that extraction errors can dominate in the early inspiral of BNS simulations (e.g. Ref. [16]). In BBH simulations, errors in waveform extraction have been well investigated (e.g., Refs. [32, 25]). BBH waveform extraction has undergone many recent advances with the development of CCE [92, 91]. Unlike FRE, CCE evolves the spacetime from a chosen timelike worldtube out to future null infinity and is capable of resolving gravitational wave memory [97]. Since CCE is generally considered to be the best mathematically well-motivated extraction method, we evaluate extraction error by comparing between CCE and FRE waveforms in SpEC, effectively treating CCE as a reference point. We prefer this method over comparing different FRE waveforms as it gives a measure of total FRE error. It has been shown that for BBH, CCE is more accurate than FRE in that it obeys the Bondi constraints better and matches better to PN at early times [85, 86, 87], and it has been shown that the numerical truncation error associated with CCE is much smaller than the numerical truncation error of the spectral BBH Cauchy evolution [92, 91]. Given that even for spectral BBH simulations the FRE error is smaller than truncation error [25], we expect truncation error (in particular due to hydrodynamics) and not wave extraction error to be dominant for current BNS waveforms. Note, however, that some aspects of CCE are under active investigation, and beyond the scope of this work.

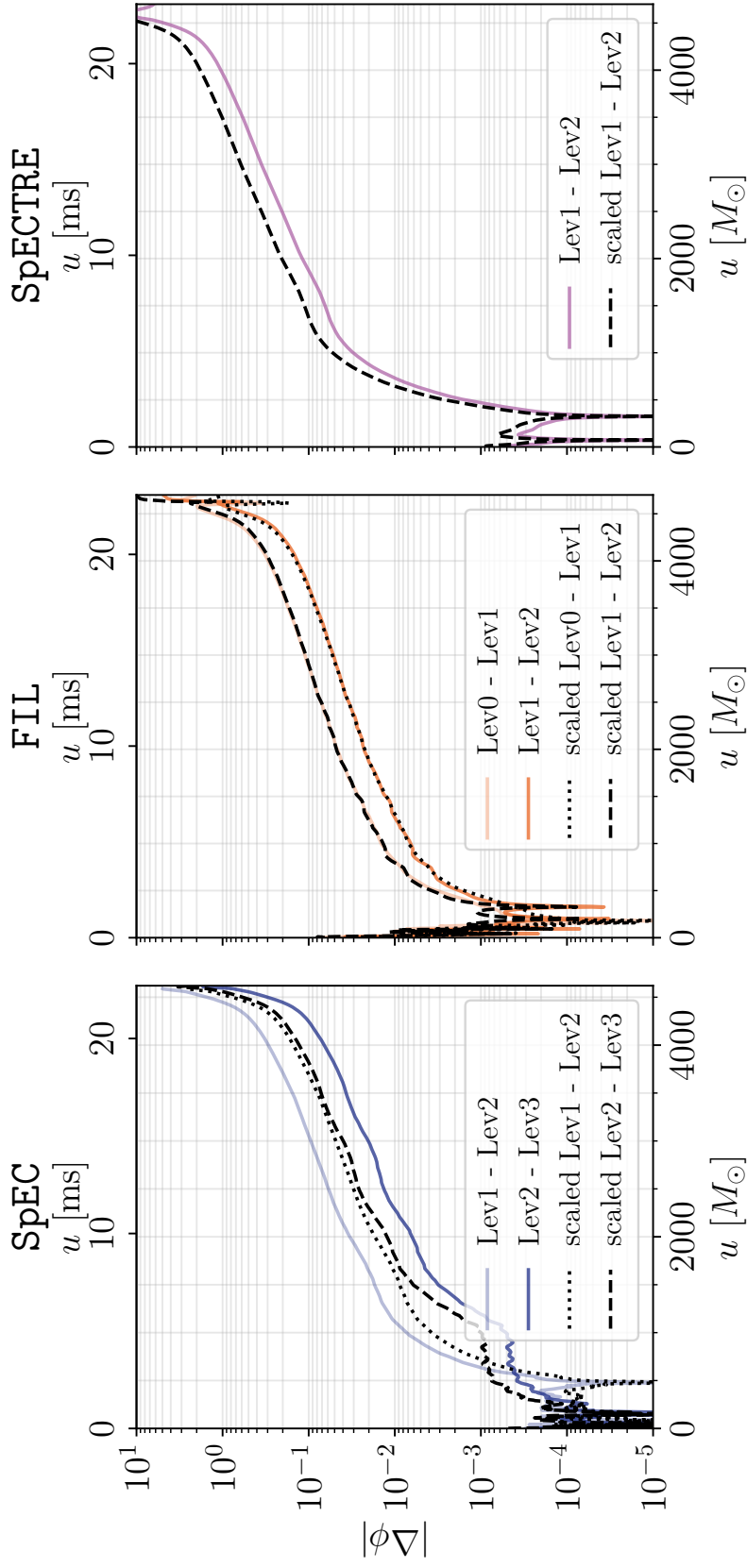


Figure 3.4: Phase difference over time between runs at varying resolutions of the same code, with SpEC in the left panel and FIL in the right panel. Waveforms are unaligned and instead have matched estimated retarded times as in Fig. 3.3. Dashed lines show error curves rescaled by an assumed convergence factor—both SpEC errors and FIL errors are scaled by third order. The rescaled errors match the measured errors if the code conforms to the assumed convergence order; otherwise the error is not well-described by a single convergence order. SpEC is generally expected to be limited to fifth-order convergence but instead scales with seventh order, indicating that in reality SpEC has no clear convergence order in this regime. FIL is consistent with the expected and previously shown third-order convergence during most of inspiral.

Figure 3.5 shows the phase difference between CCE and FRE waveforms at the same FD grid resolution. The shown CCE waveform is extracted using a worldtube radius of  $R = 496 M_{\odot}$ . The CCE waveform has been aligned with a time and phase shift to SpEC Lev3 as extrapolated with FRE. The black dashed line shows the phase difference (i.e. the truncation error, similar to those shown in Fig. 3.4) between SpEC Lev2 and SpEC Lev3, both extrapolated with FRE, for comparison of truncation error with extraction error. In general, truncation error is either larger than or comparable to the phase difference between CCE and FRE waveforms through inspiral and is clearly larger than extraction error at merger, indicating that truncation error tends to dominate over extraction error, as expected.

It turns out that the choice of CCE worldtube radius makes a small difference in the CCE waveforms, for reasons that are not fully understood and beyond the scope of this work. In theory, the best choice of worldtube radius minimizes Bondi constraint values. For Fig. 3.5, we choose the worldtube radius that minimizes the Bondi constraint value  $\Psi_2$ , as  $\Psi_2$  is a criterion in BMS frame fixing. However, extraction error is subdominant relative to truncation error at all examined worldtube radii, so our findings are not significantly impacted by the choice of radius.

### 3.3.2.3 Phase error comparison

In this section, our goal is to directly compare the phase errors of the three different codes presented in this chapter. This is important because it allows us to draw conclusions about potential systematic differences between the codes (e.g., small differences even on the initial data level will lead to slightly different physical parameters of the system). It also allows us to estimate the computational cost per level of accuracy, which we do in the next section.

One way of facilitating a comparison is to designate a reference solution and compare to it. This is easiest if a clear convergence order of a code can be established, as it allows us to extrapolate the numerical solutions to their continuum limit (at zero grid spacing), so-called Richardson extrapolation. Given a numerical solution  $\tilde{f}(\Delta x)$  computed at two different grid resolutions  $\Delta x_1$ ,  $\Delta x_2$  and known convergence order  $p$ , the solution in the limit of zero grid spacing can be estimated from Eq. (3.14) as

$$f(x) \approx \tilde{f}(\Delta x_1) + \frac{\tilde{f}(\Delta x_1) - \tilde{f}(\Delta x_2)}{r^p - 1} \quad (3.16)$$

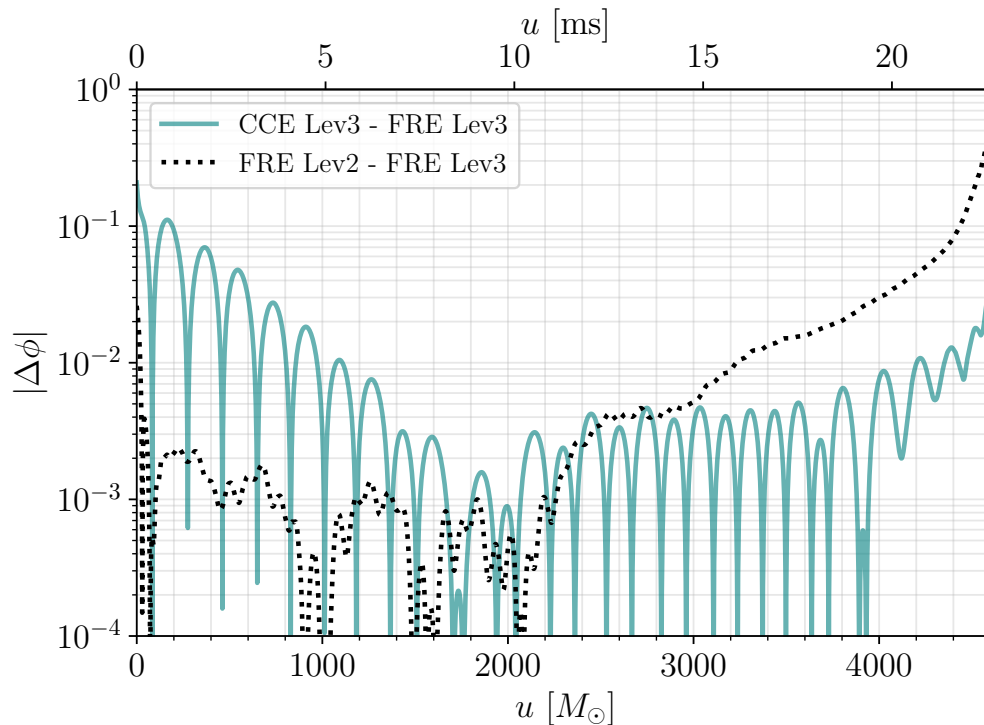


Figure 3.5: Phase difference between FRE and CCE waveforms at the same grid resolution, with the CCE waveform extracted using a worldtube radius of  $R = 496 M_{\odot}$ . The black dashed line shows relative truncation error between SpEC Lev2 and SpEC Lev3 extracted with FRE. Extraction error is comparable to or lower than truncation error throughout inspiral. This trend holds for all examined CCE worldtube radii, although there is no clear trend in error with respect to worldtube radius.

assuming  $C$  is independent of grid resolution (which it should be), and with  $r = \Delta x_2 / \Delta x_1$ .

FIL results in a systematic third-order convergent solution, as shown in Sec. 3.3.2.1 (see also Ref. [89]). We therefore adopt the extrapolated FIL solution as our reference for the purpose of this comparison and compute phase differences for all waveforms. The Richardson extrapolation assumes third-order convergence in FIL (as verified in Sec. 3.3.2.1) and uses the highest two resolution runs available, FIL Lev1 and FIL Lev2. In particular, the  $l = 2$ ,  $m = 2$  strain mode is extrapolated, and the reference phase is computed from the Richardson extrapolated strain as a derived quantity.

Figure 3.6 shows the phase error relative to the reference phase for all runs. Each

run has independently been aligned to the Richardson extrapolated waveform using the process outlined in Sec. 3.2.2. The phase differences oscillate around zero at early times because of the choice of alignment window.

The behavior of the errors in each code as grid resolution changes indicates whether there is a systematic phase discrepancy between the two codes. If SpEC converged to a significantly different phase evolution from FIL, the difference in the SpEC phase from the Richardson extrapolated FIL phase would asymptotically approach some large value as grid resolution increases. In Fig. 3.6 we find that SpEC and FIL approach similar magnitudes of phase error with increasing grid resolution, and SpEC appears to approach 0 with increasing resolution instead of leveling off at a finite value. The errors in SpEC Lev3 and FIL Lev2 (the highest resolution runs from each code) differ from each other on the scale of  $O(10^{-2})$  through inspiral. Given that, as shown in Sec. 3.3.2.1, truncation error is also generally of order  $O(10^{-2})$ , we conclude that no systematic difference in phase between SpEC and FIL is resolvable from truncation error at these resolutions. Figure 3.6 indicates a rough upper bound on truncation error in phase for FIL, which is on the order of  $O(10^{-1})$  for the resolutions we adopt.

### 3.3.3 Implications

In order to keep up with the accuracy demands of next-generation gravitational wave detectors, numerical waveforms need to reach mismatch errors much smaller than what is currently achieved [100, 63]. In this section we discuss the numerical resolution and computational cost required for such an improvement.

A way of estimating accuracy and cost requirements is through waveform mismatches. Mismatch is a standard tool in gravitational waveform analysis for not only error measurement but also matching waveform templates to signal data. Our definition of mismatch, which we summarize here, is the same as in Ref. [22].

Given two complex waveform strains  $h_1$  and  $h_2$ , we define their inner product  $\langle h_1 | h_2 \rangle$  as

$$\langle h_1 | h_2 \rangle = \int_{-\infty}^{+\infty} \frac{\tilde{h}_1(f) \tilde{h}_2^*(f)}{S_n(f)} df, \quad (3.17)$$

where  $\tilde{h}_1(f)$  and  $\tilde{h}_2(f)$  are the strains in the frequency domain,  $\tilde{h}_2^*(f)$  is the complex conjugate of  $h_2(f)$ , and  $S_n(f)$  is noise power spectral density.  $S_n(f)$  is set by detector precision, and we use the Advanced LIGO noise curve [13] for the

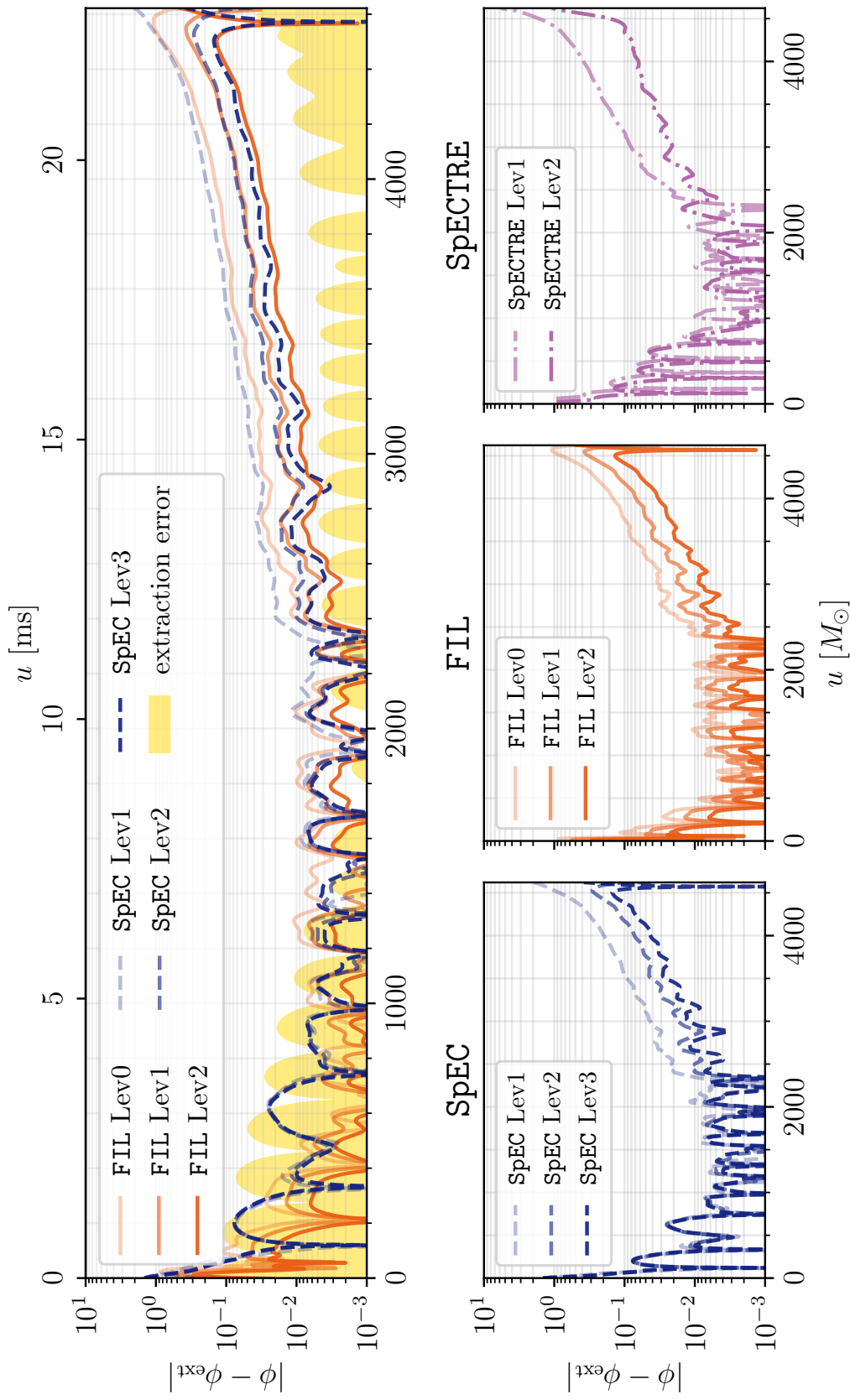


Figure 3.6: Phase difference over time in radians relative to the waveform Richardson-extrapolated from FIL Lev1 and FIL Lev2 for all runs. The top panel shows phase errors from different codes together (with SpEC error in dashed lines and FIL error in solid lines), and the bottom panels show the errors measured for each code separately. The shaded region shows extraction error as measured from SpEC in Sec. 3.3.2.2, using the CCE radius  $R = 496 M_{\odot}$ . SpEC and FIL show similar magnitudes in error, indicating that there is no resolvable systematic difference between the two codes at the chosen grid resolutions. Both SpEC and FIL appear to approach 0 error with increasing resolution. Additionally, phase differences are consistently larger than extraction error, indicating that evolution error dominates throughout inspiral. Low phase error in the range of roughly  $[700 M_{\odot}, 2000 M_{\odot}]$  is a consequence of waveform alignment, which minimizes amplitude and phase differences within the chosen time window.

following calculations. Then, we define mismatch  $\mathcal{M}(h_1, h_2)$  as

$$\mathcal{M}(h_1, h_2) = 1 - \max_{\delta\phi, \delta t} \Re \left[ \frac{\langle h_1 | h_2 \rangle}{\sqrt{\langle h_1 | h_1 \rangle \langle h_2 | h_2 \rangle}} \right], \quad (3.18)$$

in which  $h_1$  and  $h_2$  are aligned with phase and time shifts  $\delta\phi$ ,  $\delta t$  that minimize mismatch. We use the alignment procedure described in Sec. 3.2.2 to align waveforms for the purposes of mismatch analysis. We compute mismatches using only the  $l = 2, m = 2$  strain modes, and we use the extent of each numerical waveform from the end of junk radiation to the peak amplitude.

We compare mismatches to the faithfulness criterion defined in [58, 35] and perform an analysis similar to that done in [47]. For faithful GW parameter estimation, a numerical waveform  $h$  should satisfy

$$\mathcal{M}(h, h_{\text{ref}}) < \frac{N}{2\tilde{\rho}^2}, \quad (3.19)$$

where  $\tilde{\rho}$  is the desired signal-to-noise ratio (SNR). Formally,  $N \leq 1$ , but in practice it is sometimes set to the number of intrinsic parameters in order to obtain a less strict threshold value [29], so we use both  $N = 1$  and  $N = 6$ . We use the Richardson extrapolated strain computed in Sec. 3.3.2.3 as  $h_{\text{ref}}$ . To determine what grid spacing would be necessary to reach a given mismatch threshold, we can extrapolate mismatch to arbitrary resolution by fitting computed mismatches to a power law ( $\mathcal{M} \propto \Delta x^{-p}$ , where  $p$  is convergence order). For the following analysis, we assume a convergence order of  $p = 3$  for both codes, which is likely an underestimate for SpEC and consistent with the previously shown results in Sec. 3.3.2.1 for FIL.

Figure 3.7 shows the relationship between mismatches and grid separation. Scatter plot points in both subplots show the reference mismatches for the various numerical BNS runs from SpEC and FIL. Solid curves show mismatch extrapolated for each code to arbitrary resolutions using the known reference mismatches. The distinguishability thresholds with  $\tilde{\rho} = 30$  and  $N = \{1, 6\}$  are marked as dashed horizontal lines. The mismatch extrapolations and the threshold lines intersect at the grid separation required for the reference mismatch in either code to meet the threshold criteria. Figure 3.8 then shows total compute time in core hours until merger as a function of grid separation. Compute cost curves are extrapolated from the known costs of numerical runs (given in Table 3.1) using the cost scaling  $\propto \mathcal{O}(\Delta x^4)$ . Scatter plot points show these compute costs for the numerical runs from SpEC and FIL. The diamond and cross points show the extrapolated costs at the resolutions required to reach the target thresholds as shown in Fig. 3.7.

Code	Threshold $N$	Threshold grid spacing [ $M_{\odot}$ ]	Threshold grid spacing [m]	Projected computational cost to merger [core-hours]
SpEC	1	0.0360	53.2	10,647,965
SpEC	6	0.0654	96.6	976,546
FIL	1	0.0408	60.2	31,213,955
FIL	6	0.0742	109.6	2,864,719

Table 3.2: A summary of the results computed in Sec. 3.3.3. For the given code and reference mismatch threshold, the grid resolution and computational cost required to achieve the threshold mismatch are shown according to the extrapolations specified in Sec. 3.3.3.

The mismatches  $\mathcal{M}(h, h_{\text{ref}})$  of SpEC Lev2 and SpEC Lev3 are 0.0336 and 0.0114 respectively. Extrapolating from these mismatches, we find that, assuming third order convergence, a SpEC run must have a grid spacing of  $\sim 0.036 M_{\odot}$  in order to reach the  $N = 1$  threshold, i.e. roughly triple the resolution of SpEC Lev3 and a  $\sim 97\times$  cost increase; SpEC reaches the  $N = 6$  threshold at a grid resolution of  $\sim 0.065 M_{\odot}$ , i.e. roughly double the resolution of SpEC Lev3 and a  $\sim 8\times$  cost increase. For a more conservative cost estimate, we can treat the convergence order as a fitting parameter instead of fixing it. This gives a resulting convergence order of  $p = 5.2$ , which is plausible for SpEC, and the target resolution becomes  $\sim 0.063 M_{\odot}$ , leading to a  $\sim 9\times$  cost increase. For FIL Lev2 and FIL Lev1, we find mismatches  $\mathcal{M}(h, h_{\text{ref}})$  of 0.0104 and 0.0512. The  $N = 1$  threshold resolution assuming third order convergence is then  $\sim 0.041 M_{\odot}$ , resulting in a  $\sim 134\times$  cost increase from FIL Lev3; the  $N = 6$  target resolution is  $\sim 0.074 M_{\odot}$ , giving a  $\sim 5\times$  cost increase. These results are summarized in Table 3.2.

## 3.4 Conclusion

Next-generation gravitational wave detectors offer exciting prospects for probing dense matter with BNS [28, 56]. In order to extract this information from the GW signal, highly accurate models for inspiral gravitational wave emission will be needed [63]. Crucially, these rely on calibration to NR simulations [44], which in turn will have similar accuracy requirements.

In this work, we investigated potential systematics in gravitational waveforms computed with current numerical relativity simulations. We have done so by performing

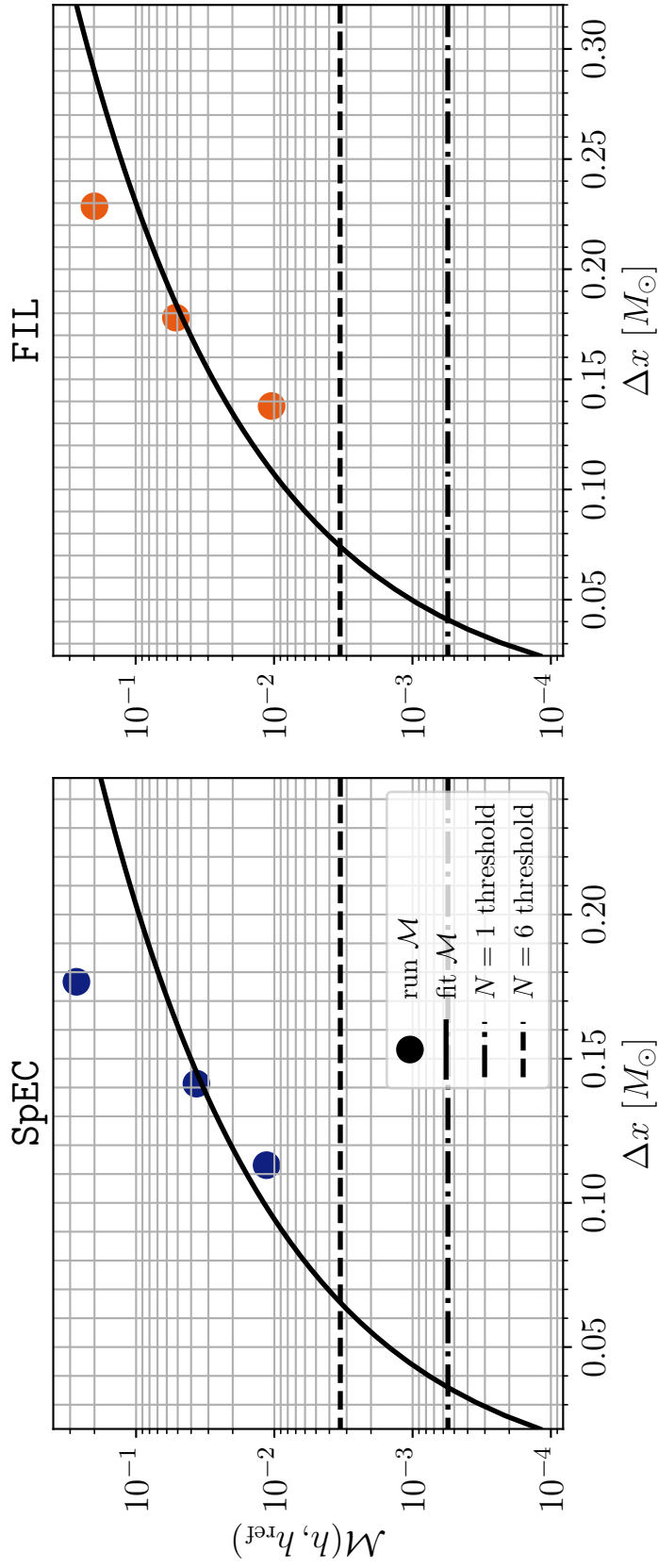


Figure 3.7: Computed mismatches between the Richardson extrapolated FIL waveform and presented numerical BNS waveforms from SpEC and FIL of varying grid separation (grid separation increases from left to right in each subplot). Solid lines denote the extrapolated mismatch as a function of grid resolution, as determined by the power law  $\mathcal{M} \propto \Delta x^{-p}$ . For both codes, we assume  $p = 3$ . Mismatch extrapolations use the two data points of lower grid separation in each subplot. Dashed lines mark the threshold mismatch values, defined by Eq. (3.19).

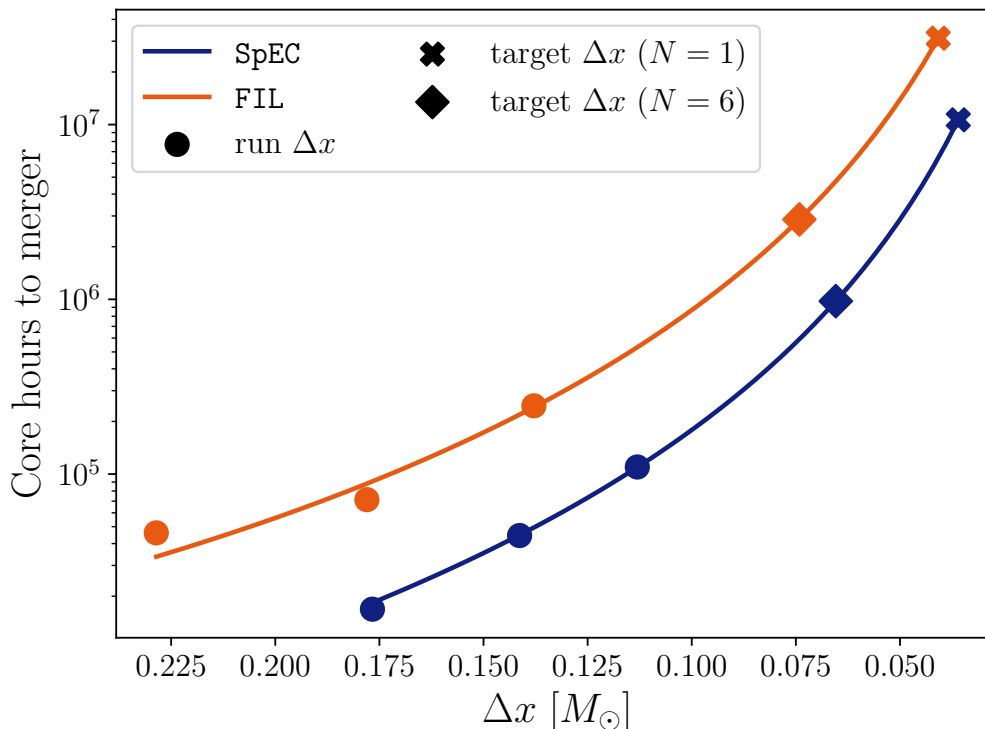


Figure 3.8: The computational cost in core hours for a BNS waveform through merger in relation to the finite difference grid separation  $\Delta x$ . Dots mark compute times of runs presented in this paper, crosses mark the projected costs given the grid separations required to reach the  $N = 1$  mismatch threshold shown in Fig. 3.7, and diamonds mark the respective costs for the  $N = 6$  threshold. Curves are extrapolated from known run costs assuming cost scales as  $O(\Delta x^4)$ . For either SpEC or FIL, a BNS run with high enough grid resolution to reach the target mismatch would require on the order of 1 million to 10 million core hours.

a direct code comparison of three NR codes (FIL, SpEC, SpECTRE) that are maximally different in both the equations they solve and the numerical schemes they use. We have presented a detailed BNS error analysis that covers GW phase error, convergence behavior, and extraction error across multiple resolutions of BNS runs with the same initial data parameters. By quantifying error in a BNS waveform observable and considering the relative impacts of evolution error and extraction error, this analysis contributes to an area of limited study in the current literature.

Reassuringly, we find that within currently used numerical resolutions the codes systematically agree, and are, in part, convergent. We further show that waveform extraction errors are at present negligible when compared to a more accurate and well-defined CCE approach. Also, SpEC and SpECTRE use pseudo-spectral and

finite-element methods for the wavezone. In this region, BNS simulations are the same as BBH simulations for these codes, and BBH simulations with SpEC and SpECTRE have substantially smaller errors than BNS (e.g., Refs. [25, 84]). These considerations likely imply that the waveform error is currently limited by the hydrodynamic evolution.

Using the current computational cost, which for a given accuracy we find to be roughly comparable among all codes within a factor of a few (see Table 3.1), we predict that resolutions three to four times higher than what are used now may be needed to build a catalog to meet the requirements of next-generation facilities (see also Ref. [47] for similar conclusions). Additional improvements on the hydrodynamics side [47, 74] (see also Refs. [101, 16, 89]), as well as the use of new hardware acceleration [55] may be necessary to overcome present limitations.

As a starting point, this work only considers one binary configuration with equal mass components (see, e.g., Ref. [72] for potential challenges in BBH waveforms). Additionally, our analysis is confined to the  $l = 2$ ,  $m = 2$  waveform mode. Higher-order modes have even greater accuracy requirements in order to be numerically resolved, but may be important for unequal mass systems. Future work will be needed to address these issues.

### 3.5 Acknowledgments

We would like to thank Keefe Mitman, Kyle Nelli, Yoonsoo Kim, and Nicholas Rui for helpful discussions. This material is based upon work supported by the National Science Foundation under Grants No. PHY-2309211, No. PHY-2309231, and No. OAC-2209656 at Caltech and No. PHY-2407742, No. PHY-2207342, and No. OAC-2209655 at Cornell. ERM acknowledge support by the National Science Foundation under grants No. PHY-2309210 and OAC-2103680. ERM acknowledges the use of Delta at the National Center for Supercomputing Applications (NCSA) through allocation PHY210074 from the Advanced Cyberinfrastructure Coordination Ecosystem: Services & Support (ACCESS) program, which is supported by National Science Foundation grants #2138259, #2138286, #2138307, #2137603, and #2138296. Additional simulations were performed on the NSF Frontera supercomputer under grant AST21006. ERM also acknowledges support through DOE NERSC supercomputer Perlmutter under grant m4575, which uses resources of the National Energy Research Scientific Computing Center, a DOE

Office of Science User Facility supported by the Office of Science of the U.S. Department of Energy under Contract No. DE-AC02-05CH11231 using NERSC award NP-ERCAP0028480. Any opinions, findings, and conclusions or recommendations expressed in this material are those of the author(s) and do not necessarily reflect the views of the National Science Foundation. This work was supported by the Sherman Fairchild Foundation at Caltech and Cornell.

